2017

Thermal transport in thin films and across interfaces

BOSTON UNIVERSITY

COLLEGE OF ENGINEERING

Dissertation

THERMAL TRANSPORT IN THIN FILMS AND ACROSS INTERFACES

by

ELBARA OUSSAMA ZIADÉ

B.S., Boston University, 2012
M.S., Boston University, 2015

Submitted in partial fulfillment of the

requirements for the degree of

Doctor of Philosophy

2017

Approved by

First Reader

Aaron J. Schmidt, PhD
Assistant Professor of Mechanical Engineering
Assistant Professor of Materials Science and Engineering

Second Reader

Enrico Bellotti, PhD
Professor of Electrical and Computer Engineering
Professor of Materials Science and Engineering

Third Reader

Chuanhua Duan, PhD
Assistant Professor of Mechanical Engineering
Assistant Professor of Materials Science and Engineering

Fourth Reader

Dan Cole, PhD
Associate Professor of Mechanical Engineering

There is no rest in residence for a person of culture and intellect;
so travel and leave where you're residing!
Travel! You will find a replacement for what you have left.
And Strive! The sweetness of life is in Striving!

I've seen that water stagnates if still
becomes pure if it runs, but not if it doesnt flow.
If the lion doesn't leave his den he cannot hunt,
and the arrow will not strike without leaving its bow.

If the sun stood still in its heavenly course
then people it would bore.
Gold dust is as the earth where commonly found,
and in its land, agarwood (oud) is but another wood in store.

If one travels, he becomes sought out.
If one travels, he is honored like gold.

A Call To Travel - A Poem By Imam As-Shafi'ee

Acknowledgments

This thesis and the work herein would not have been possible without the support and guidance of many people. First, I would like to thank my advisor, **Professor Aaron J. Schmidt**, for his patience and guidance. I would not have been able to complete this research without his mentorship. Aaron helped me become a better researcher, writer, and experimentalist.

I would like to thank my committee members, **Professor Chuanhua Duan**, **Professor Enrico Bellotti**, and **Professor Dan Cole**. Professor Duan connected me with Aaron almost five years ago when I first started this project and it would not have been possible without the introduction. Professor Bellotti pushed me to improve my mathematics and modeling abilities and has always found a way to share a joke in the hallways of Photonics. Professor Dan Cole first introduced me to modeling and finite element analysis.

There are many professors that I would like to thank for their guidance and mentorship during my years at BU. I would like to graciously thank **Professor Ted D. Moustakas** for his guidance and sage advice. His discussions always helped advance my knowledge and basic understanding of gallium nitride and diamond material systems. Special thanks to **Professor Matthias Schneider** for lending his laboratory and resources. I would also like to thank Professor Schneider for welcoming me into his lab as an undergraduate. Thank you to **Professor Bill Hauser** for great discussions, mentorship, and support.

I would like to **thank my family** for their unconditional love and support. Special thanks to my labmates, **Jia Yang and Miguel Goni**. I would like to thank my friends, **Lauren, Corey, David and Steve**. Also, thanks to my first friend in graduate school and an inspiring friend **Calvin Patmont**.

Finally, I would like to thank my external funding agencies NAMICS and eM-

TECH. Thank you **Dr. Pawel Czubarow** and **Mr. Toshiyuki Sato**. I would also like to thank my collaborators from Element Six. Thank you **Dr. Firooz Faili** and **Dr. Daniel Francis**.

Elbara Oussama Ziadé

Student

ME Department

THERMAL TRANSPORT IN THIN FILMS AND ACROSS INTERFACES

ELBARA OUSSAMA ZIADÉ

Boston University, College of Engineering, 2017

Major Professor: Aaron J. Schmidt, PhD
Assistant Professor of Mechanical Engineering
Assistant Professor of Materials Science and Engineering

ABSTRACT

Heat dissipation is a critical bottleneck for microelectronic device performance and longevity. At micrometer and nanometer length scales heat carriers scatter at the boundaries of the material reducing its thermal conductivity. Additionally, thermal boundary conductance across dissimilar material interfaces becomes a dominant factor due to the increase in surface area relative to the volume of device layers. Therefore, techniques for monitoring spatially varying temperature profiles, and methods to improve thermal performance are critical to future device design and optimization.

The first half of this thesis focused on frequency domain thermoreflectance (FDTR) to measure thermal transport in nanometer-thick polymer films and across an organic-inorganic interface. Hybrid structures of organic and inorganic materials are widely used in devices such as batteries, solar cells, transistors, and flexible electronics. The Langmuir-Blodgett (LB) technique was used to fabricate nanometer-thick polymer films ranging from 2 - 30 nm. FDTR was then used to experimentally determine the thermal boundary conductance between the polymer and solid substrates.

The second half of the thesis focused on developing a fundamental understanding of thermal transport in wide-bandgap (WBG) materials, such as GaN, and ultrawide-bandgap (UWBG) materials, such as diamond, to improve thermal dissipation in power electronic devices. Improvements in WBG materials and device technologies have slowed as thermal properties limit their performance. UWBG materials can provide a dramatic leap in power electronics technologies while temporarily sidestepping the problems associated with their WBG cousins. However, for power electronic devices based on WBG- and UWBG-materials to reach their full potential the thermal dissipation issues in these hard-driven devices must be understood and solved. FDTR provides a comprehensive pathway towards fully understanding the physics governing phonon transport in WBG- and UWBG-based devices. By leveraging FDTR imaging and measuring samples as a function of temperature, defect concentration, and thickness, in conjunction with transport models, a well-founded understanding of the dominant thermal-carrier scattering mechanisms in these devices was achieved. With this knowledge we developed pathways for their mitigation.

Contents

List of Tables

List of Figures

List of Abbreviations

AFM	.....	Atomic Force Microscopy
AlN	.....	Aluminum Nitride
AMM	.....	Acoustic Mismatch Model
BTE	.....	Boltzmann Transport Equation
DMM	.....	Diffuse Mismatch Model
E-beam	.....	Electron-Beam
FDTR	.....	Frequency Domain Thermoreflectance
GaN	.....	Gallium Nitride
LB	.....	Langmuir Blodgett
MBE	.....	Molecular Beam Epitaxy
PVAc	.....	Polyvinyl Acetate
RMS	.....	Root-Mean-Square
SEM	.....	Scanning Electron Microscopy
TBC	.....	Thermal Boundary Conductance
UWBG	.....	Ultra Wide-Band Gap
WBG	.....	Wide-Band Gap

List of Symbols

c_p	.....	Specific Heat
E	.....	Energy
G	.....	Thermal Boundary Conductance
$\hbar$	.....	Reduced Planck Constant
I	.....	Gaussian Laser Intensity
k	.....	Wave Number (Hankel transform coefficient in Chapter 3)
p	.....	Momentum
v	.....	Velocity
w_0	.....	$1/e^2$ Radius
Z	.....	Correction Coefficient for DMM
κ	.....	Thermal Conductivity
λ	.....	Wavelength
Λ	.....	Phonon Mean Free Path
Π	.....	Lateral Surface Pressure
ρ	.....	Density
ω	.....	Phonon Frequency
ζ	.....	Transmission Coefficient

Chapter 1

Introduction

1.1 Motivation

Thermal management plays a critical role in the functionality and reliability of modern microelectronics. As microelectronics continue to miniaturize and hybridize components, heat dissipation becomes a critical bottleneck for their performance and longevity. This is because at micrometer and nanometer length scales, the material properties, particularly the thermal conductivity, may deviate significantly from the bulk leading to a temperature rise in devices, which causes device failure (Chen et al., 2005). Moreover, the heat conduction in micrometer or nanometer-scale features is often limited by heat flow across the interfaces (Cahill et al., 2014), which prevents the reliable operation of electronic devices such as the heat assisted magnetic recording, phase change memories, and high electron mobility transistors based on wide-bandgap nitride material systems (Shi et al., 2015; Meneghesso et al., 2008). The purpose of this thesis is to contribute to the fundamental understanding of how heat energy moves at the micrometer and nanometer length scales and across interfaces. The motivation of measuring and understanding these phenomenas is to identify and mitigate the major bottlenecks to heat dissipation.

1.1.1 Composites

We first investigated thermal properties that limit heat flow in composite materials. A composite material consists of a host material with embedded particles that are used

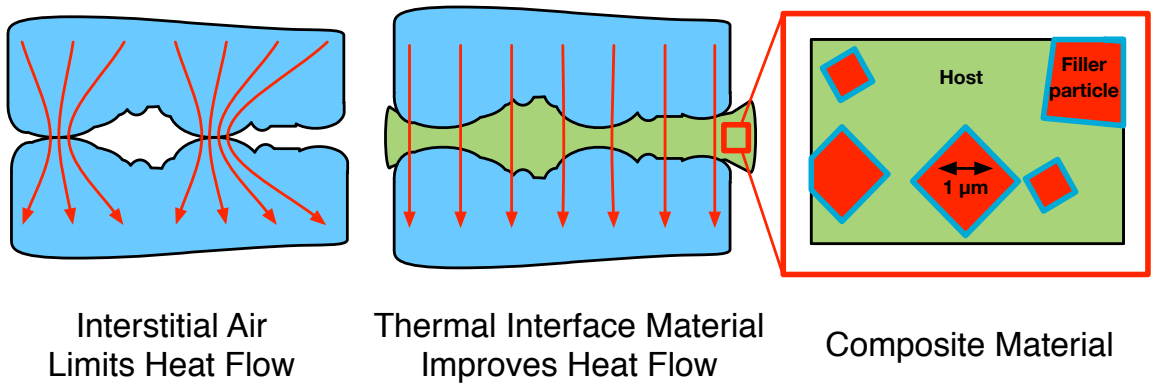

Figure 1·1: Thermal interface material and composites.

to modify the macroscopic properties of the host. We investigated composite materials used as flexible thermal interface materials as shown in Fig. 1·1. The flexibility of the composite material insures minimal interstitial air between electronic devices and heat sinks, which increases heat dissipation. Polymers are flexible and compliant making them candidate host materials. However, polymers are poor conductors of heat due to their amorphous nature (Wong and Bollampally, 1999), although, ordering the polymer chains can improve the thermal conductivity (Singh et al., 2014). More commonly, ceramic microparticles with high thermal conductivity are added (Gong et al., 2014; Shen et al., 2011) to increase the thermal transport in polymers used as flexible heat sinks. These particles can also be metalized prior to matrix embedment to improve thermal transport into and out of the particle (Zhang et al., 2011; Krupa et al., 2007).

There are two key questions to answer when designing composites as flexible thermal interface materials. First, what is the thermal conductivity of the micro and nanoparticles used as fillers? The particles are size-constrained and this will freeze out thermal carriers with mean free paths larger than the dimension of the particle, reducing thermal conductivity. Additionally, the quality of the particles will also impact the thermal conductivity. For example, a particle that is not be fully

dense will exhibit lower thermal conductivity. Second, how well does heat move into and out of the ceramic particles from the host matrix? If the thermal boundary conductance between the polymer host and the ceramic particle is too low, then little heat will enter the ceramic particles and we will fail to take advantage of the particles relatively high thermal conductivity.

In this thesis we developed techniques to answer these two critical questions for composite design. We improved an optical pump-probe measurement technique known as frequency domain thermoreflectance (FDTR) for high-throughput thermal conductivity measurements of individual microparticles. This allows for rapid screening of candidate particles without the needed to create a complete composite. Additionally, we used the Langmuir-Blodgett (LB) technique to create an array of nanometer-thick polymer films with a varying degree of crystallinity such that our thermal measurement was sensitive to extract the thermal boundary conductance between the polymer film and a ceramic, a polymer film and a metal, as well as the thermal conductivity of the polymer films.

1.1.2 Wide-bandgap semiconductors

Wide-bandgap (WBG) semiconductors, such as gallium nitride (GaN), and ultrawide-bandgap (UWBG) semiconductors, such as diamond, have attracted a significant amount of interest for next generation amplifiers, power electronics devices, cell-phone networks, solid-state lighting applications, and power distribution networks due to their relatively high breakdown voltages and high current density capabilities (Albrecht et al., 2010; Rosker, 2007; Su et al., 2013b; Wang et al., 2014; Mishra et al., 2008; Moskalyk, 2003; Babic et al., 2010; Iacopi et al., 2015). As the size of WBG- and UWBG-based transistors decreases to achieve higher operating frequencies, heat dissipation from the active device layer is expected to worsen due to thermal interface resistance and phonon boundary scattering, as well as dislocation

and impurity scattering of phonons (Chou et al., 2004; Bloschock and Bar-Cohen, 2012; Won et al., 2013; Cahill et al., 2014). Phonons are quantized lattice vibrations and are the primary carriers of heat in both semiconductors and insulators (Chen, 2005). Calculating the dominant phonon scattering mechanisms in WBG and UWBG systems is critical for developing higher quality materials and designing devices that can quickly dissipate heat, because a temperature rise in these devices will reduce the transistor's electron mobility and maximum drain current, potentially increase gate leakage, and ultimately diminish device lifetime (Xu et al., 2007; Meneghesso et al., 2008; Cho and Goodson, 2015). For example, a 5°C increase in temperature above the optimum operating range can reduce the lifetime of a device by half (Meneghesso et al., 2008; Wyrwas et al., 2011). Despite the importance of characterizing thermal transport in WBG and UWBG semiconductor films, the literature remains unclear as to the dominant phonon scattering mechanisms in these material systems (Beechem et al., 2016; Mion et al., 2006).

This thesis adds to the fundamental understanding of phonon transport in WBG and UWBG semiconductor systems to improve heat dissipation in thin-film power electronic devices, with a specific focus on GaN and diamond material systems. By measuring samples as a function of temperature and thickness, in conjunction with phonon-transport models, we developed a better understanding of the dominant phonon-scattering mechanisms in these systems. Figure 1·2 summarizes the targeted regions of thermal analysis for improving the thermal conductivity of WBG and UWBG semiconductors and the thermal boundary conductance (TBC) to metallic pads and crystalline substrates.

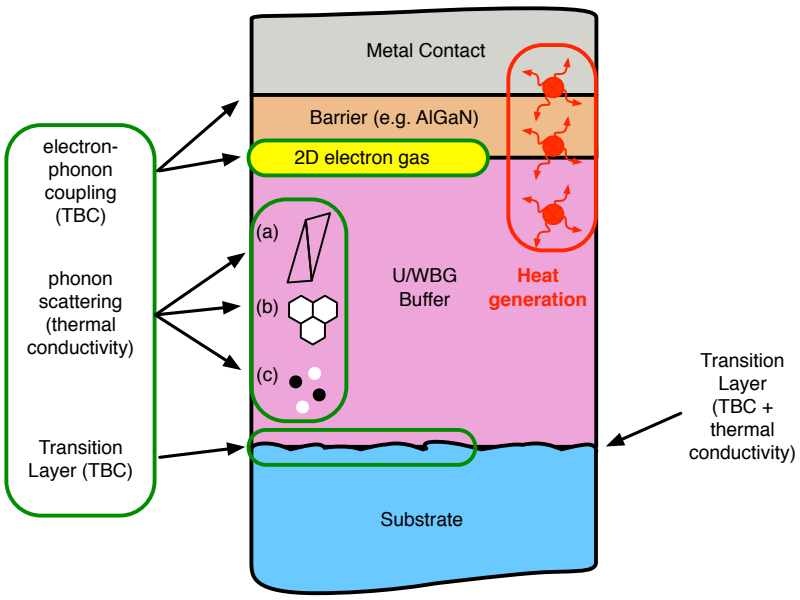

Figure 1·2: Phonon scattering in WBG and UWBG materials. These scattering mechanisms represent opportunities to optimize thermal transport. (a) grain boundary and dislocation scattering (b) atomic composition (c) Rayleigh scattering at impurity or vacancy sites.

1.2 Outline of the Thesis

Chapter two is a review of thermophysical properties. Details about heat carriers and the phonon models used in this thesis are described.

Chapter three is an overview of our optical pump-probe thermal microscope, frequency domain thermoreflectance (FDTR). Details about the setup, thermal model and imaging techniques are discussed. We demonstrated FDTR imaging for measurements of AlN microparticles embedded in an epoxy host.

Chapter four focuses on thermal transport in polymer-based composites. Polymer-based composites are used in flexible electronics, batteries, and as an interface material for heatsinks. The interface between a polymer matrix and inorganic material in a composite material is the limiting component for heat transfer. As can be seen in Fig. 1·1 the surface area to volume ratio of filler particles increases as their size

decreases. To better understand thermal transport across organic-inorganic interface we created a model system with PolyVinyl Acetate (PVAc) on silicon and gold. We measured the thermal conductivity of the nanometer thick PVAc film, the thermal boundary conductance between PVAc and silicon, and thermal boundary conductance PVAc and gold.

Chapter five focuses on thermal transport in the wide-bandgap semiconductor material, gallium nitride (GaN). Gallium nitride is a wide-bandgap semiconductor that is promising for next-generation RF switches and power electronics. We measured the thermal properties of GaN grown on 4H-SiC from 300-600 K. We improved the diffuse mismatch model to predict interface conductance between GaN and SiC from 300-600 K. Additionally, we investigated the thickness dependent thermal conductivity of a GaN film from 15-1000 nm. A phonon-gas model was used to capture the trend of thermal conductivity in this size-constrained system.

Chapter six focuses on the anisotropic thermal conductivity of diamond films. Diamond has an extremely high thermal conductivity, about five times higher than SiC, and is the ideal material for near-junction thermal management in GaN-based devices. We measured the thermal conductivity of polycrystalline diamond on silicon with film thickness in the range of 1-10 μm. In addition, we measured the thermal boundary conductance between a Au/Ti metallization layer and the diamond film.

Chapter seven is the summary and outlook.

Chapter 2

Theories for Heat Transport

2.1 Introduction

The purpose of this thesis is to measure how heat energy moves at the micrometer and nanometer length scales and across interfaces. The motivation of measuring these properties is to identify and mitigate the major bottlenecks to heat dissipation. In this chapter, we will briefly review the fundamentals of thermal transport physics.

2.2 Heat Carriers

Heat energy can be transmitted in solids through electrical carriers, lattice waves, electromagnetic waves, spin waves, or other excitations (Tritt, 2004). In metals, electrical carriers such as electrons or holes conduct a majority of the heat. In semiconductors and dielectrics, lattice vibrations are the primary carriers of heat. In this thesis, we primarily focus on thermal transport due to lattice vibrations.

A lattice wave that spans the entire length of a crystal can be summed up as a combination of plane waves in the form of:

$$A(x,t) = \exp\left[i\left(\frac{2\pi}{\lambda}x - \omega t\right)\right] \tag{2.1}$$

Where x is the direction coordinate, t is time, ω is the frequency, and λ is the wavelength. A plot of Eq. 2.1, where t is held constant is shown in Fig. 2·1(a). A schematic representation of a longitudinal acoustic wave traveling through a 1D

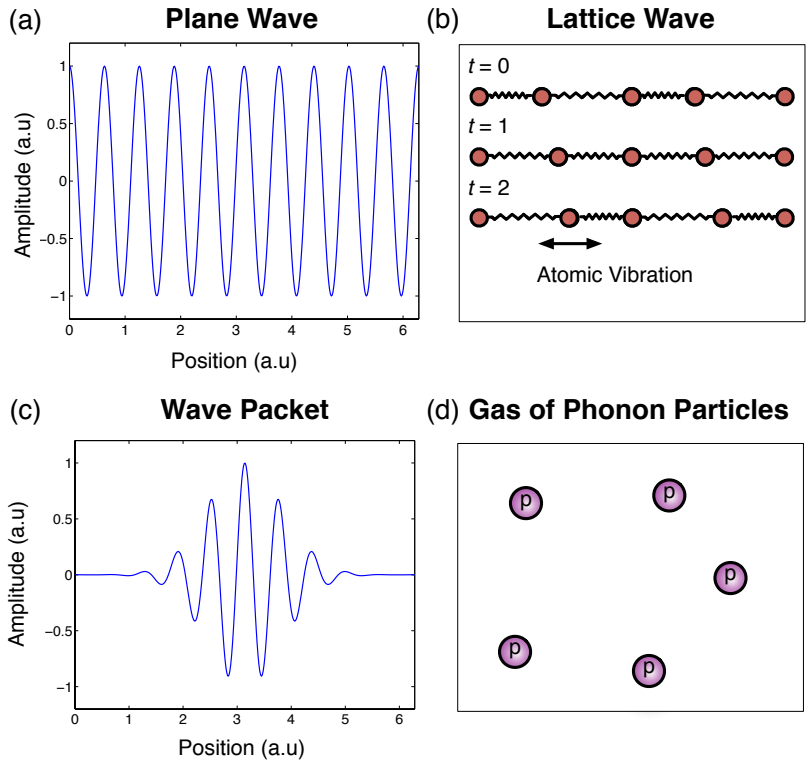

Figure 2·1: (a) A plane wave of the form $A(x,t) = \exp\left[i\left(\frac{2\pi}{\lambda}x - \omega t\right)\right]$ that propagates indefinitely. (b) Ball-spring representation of atoms vibrating and propagating a lattice wave. (c) A wave packet. (d) Gas of phonon particles.

monotonic lattice is shown in Fig. 2·1(b). A superposition of lattice waves with multiple frequencies creates a wave packet of finite size (Fig. 2·1(c)), which creates the origin of phonons.

A phonon is a quantum mechanical description of lattice vibration and can be used to describe thermal energy transport. Typically, a phonon is treated as a particle and thermal transport is a result of phonon diffusion. A gas of phonon particles that can be used to describe lattice vibrations is shown in Fig. 2·1(d). Phonons can be treated as particle so long as they are much smaller than the crystal size. The typical size of a phonon is 1-10 Å (Chen, 2005). When the size of a crystal approaches the size of a phonon particle, phonons exhibit wave-like behavior (Ravichandran et al., 2013) and the particle model of phonons is no longer valid.

A phonon is discrete and has momentum levels, p, and energy levels, E, in multiples of:

$$p = \hbar k \tag{2.2}$$

$$E = \hbar \omega \tag{2.3}$$

where $\hbar = \frac{h}{2\pi}$ and is the reduced Planck constant; $k = \frac{2\pi}{\lambda}$ and is the wave number; and $\omega = 2\pi v$, where v is the velocity of the phonon. In addition, phonons are polarized into different branches. The number of phonon branches depends on the number of atoms in a unit cell for that material. For bulk materials, this includes three acoustic phonon branches, one longitudinal acoustic (LA) and two transverse acoustic (TA) branches, and $(3w - 3)$ optical branches, where w is the number of atoms in a unit cell. As an example, we look at the phonon dispersion curves for wurtzite gallium nitride (GaN). There are four atoms in the unit cell of the GaN crystal. Therefore, there are three acoustic branches and nine optical branches. The phonon dispersion curves for GaN in the directions of high symmetry are shown in Fig. 2·2(a) (Ruf et al., 2001). A schematic of the Brillouin zone of GaN is shown in Fig. 2·2(b).

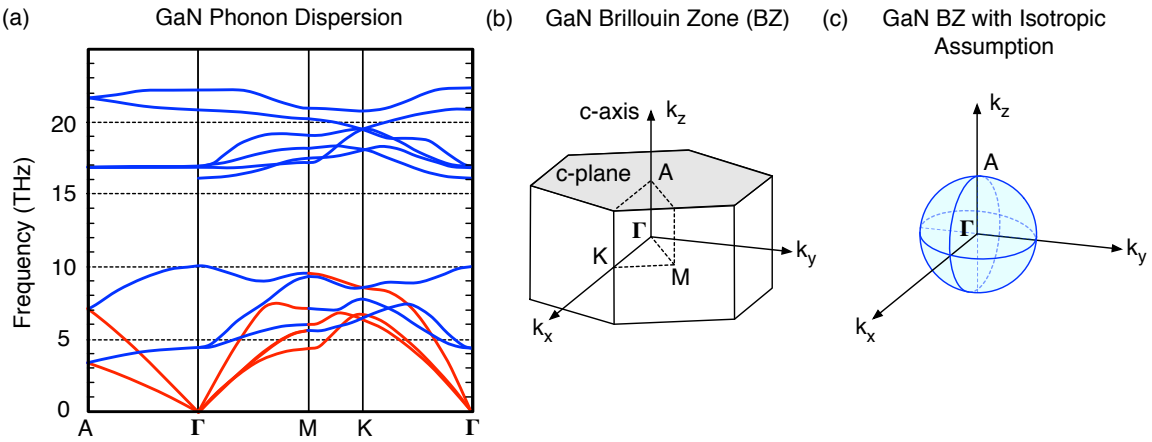

Figure 2·2: (a) Phonon Dispersion curves for GaN (Ruf et al., 2001). The red lines are the acoustic branches while the blue lines are the optical branches. (b) Brillouin zone of GaN lattice (c) The assumption of an isotropic material results in an integration over a sphere in k-space.

2.3 Thermal Conductivity

Thermal conductivity is a property of a material and defines how well heat energy is transported through the material. Classically, heat is conducted from hot to cold regions through the diffusion of thermal carriers. This implies that the random motion and collision of the carriers transfers energy from the hot to cold regions. It is important to recognize that thermal conductivity is a property that depends on the statistical properties of the heat carriers. Therefore, the population of heat carriers must be large such that they can be treated as an ensemble. In this sense, the thermal conductivity of a material under steady state heat flow can be defined by Fourier's Law of conduction. Fourier's law can be derived from the basics of statistical mechanics considering an ensemble of particles where each particle has a distribution of energy and they interact. Fourier's law is written as:

$$\vec{q} = -\kappa \nabla T \tag{2.4}$$

where κ is thermal conductivity with units $[W/mK]$, $\vec{q}$ is the heat flux density with units $[W/m^2]$, and ∇T is the temperature gradient such that $\nabla T = \frac{\partial T}{\partial x}\hat{x} + \frac{\partial T}{\partial y}\hat{y} + \frac{\partial T}{\partial z}\hat{z}$, where $\hat{x},\ \hat{y},$ and $\hat{z}$ are the unit vectors along coordinate directions.

Fourier's law is valid when heat transfer is considered to be diffusive. At very small length scales or very fast time scales, energy carriers can move non-diffusively and Fourier's law is no longer valid (Joshi and Majumdar, 1993). Practically, the failure of Fourier's law is seen in ultrafast optical pump-probe thermal measurements (Wilson and Cahill, 2014) and when the heater geometry in thermal measurements or the size of the material approaches the mean free path of a heat carriers (Wilson and Cahill, 2015).

2.3.1 Phonons and Thermal Conductivity

The Boltzmann transport equation (BTE) can be used to calculate the thermal conductivity of a material. This is because the BTE describes the statistical behavior of a thermodynamic system not in a state of equilibrium, such as a phonon-gas system with a thermal gradient. However, the BTE is an extremely difficult equation to solve explicitly with its full form given as:

$$\frac{\partial f}{\partial t} + \frac{d\vec{r}}{dt} \cdot \nabla_{\vec{r}} f + \frac{d\vec{p}}{dt} \cdot \nabla_{\vec{p}} f = \left(\frac{\partial f}{\partial t} \right)_c \tag{2.5}$$

where $\vec{r}$ and $\vec{p}$ are coordinates and momentum of the particle in 3D space, respectively, and f represents the one-particle distribution function, such that the solution of the BTE is done over an ensemble of N-particle space rather than over a system space (Chen, 2005). Recently an open-source software to fully solve the BTE has become available (Li et al., 2014). However, what is more commonly done, and what is done in this thesis, the BTE is solved using simplifying assumptions.

The solution of the BTE can be significantly simplified using the relaxation time approximation and with the assumption that the crystal is isotropic. In this solution of the BTE, the geometry of the first Brillouin zone is reduced to a sphere, such as the one shown in Fig. 2·2(c) for GaN. To simplify the BTE solution even further we could use a simplified dispersion as oppose to the real dispersion curves. Such dispersions include a Debye dispersion $\omega(k) = vk$; Born von Karman Slack dispersion $\omega(k) = \omega_{\max} \sin \frac{k\pi}{k_{\max}}$; or a polynomial fit to the real dispersion curve for a particular direction, i.e. $\Gamma - \mathrm{A}$ direction shown in Fig. 2·2(a) and (c). Using these simplifications the BTE collapses into the well-known kinetic theory:

$$\kappa = \sum_s \int_0^{\omega_{\max,s}} \frac{1}{3} C_s(\omega) v_s(\omega) \Lambda_s(\omega) d\omega \tag{2.6}$$

where $C(\omega) = \hbar\omega D(\omega)\frac{\partial n_q}{\partial T}$ is the specific heat per unit frequency interval at frequency ω and temperature T; D(ω) is the phonon density of states per unit volume and per unit frequency and can be calculated from $D(k) = \frac{4\pi k^2}{(2\pi)^3}$ depending the assumed dispersion relation; $n_q = (\exp(\hbar\omega/k_BT) - 1)^{-1}$ is the Bose-Einstein distribution; $v = \frac{d\omega}{dk}$ is the phonon group velocity; s indexes the phonon branch; and Λ_s is the distance a phonon travels before scattering. Equation 2.6 can also be written as a function of wave number k:

$$\kappa = \frac{1}{6\pi^2}\sum_s \int_0^{k_{\max,s}} C_s(k)k^2 v_s(k)\Lambda_s(k)dk \tag{2.7}$$

where

$$C_s(k) = \frac{\hbar^2\omega_s^2(k)}{k_BT^2}\frac{e^{\frac{\hbar\omega_s(k)}{k_BT}}}{(e^{\frac{\hbar\omega_s(k)}{k_BT}} - 1)^2}. \tag{2.8}$$

Typically, Λ_s is referred to as the phonon mean free path (MFP) and is defined by $\Lambda_s = \tau_s v_s$, where τ_s is the relaxation time per unit frequency. To solve Eq. 2.7 or 2.6 it is easier to solve for τ_s.

There are various scattering mechanisms which limit the phonon MFP and affect τ_s. According to Matthiessen's rule these scattering mechanisms can be added as: $\tau_s^{-1} = \sum_i \tau_{s,i}^{-1}$, where i denotes the scattering mechanism. In typical crystals, phonons are scattered by other phonons, Fig. 2·3(a); atomic vacancies and impurities, Fig. 2·3(b); lattice defects such as dislocations and grain boundaries, Fig. 2·3(c); and surface boundaries, Fig. 2·3(d) (Asen-Palmer et al., 1997; Abeles, 1963; Callaway, 1959; Holland, 1963).

In an ideal, bulk crystal, the phonon mean free path at room temperature is limited by phonon-phonon scattering. The thermal conductivity, in this case, is referred to as intrinsic and is a direct result of the lattice anharmonicity as determined by crystal structure and atomic composition. These phonon anharmonic interactions, which

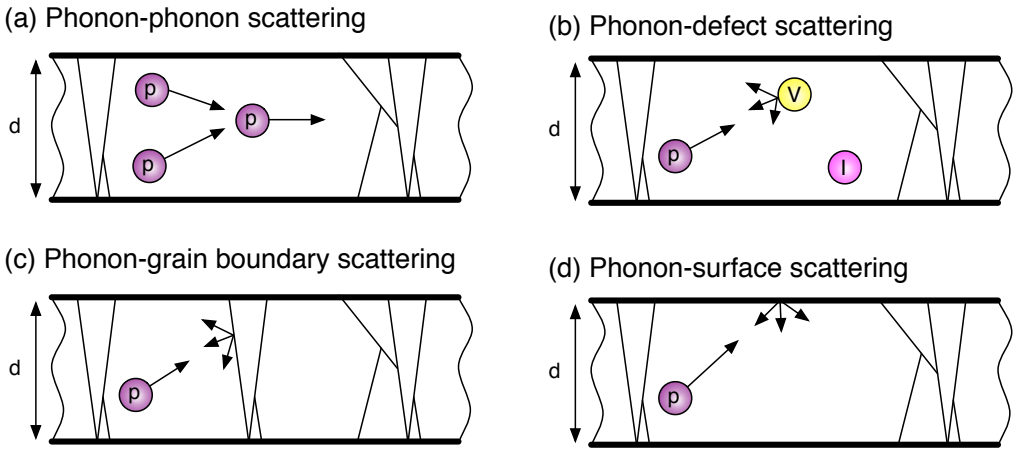

Figure 2·3: Phonon scattering mechanisms in semiconductor thin films of thickness d.

are non-momentum conserving scattering process, lead to a finite thermal conductivity and are referred to as Umklapp processes (Abeles, 1963). Momentum conserving phonon scattering interactions are referred to as normal phonon scattering processes. Normal phonon scattering does not directly contribute to thermal conductivity, but instead, this scattering process redistributes phonons from one mode to another, thus enabling alternative phonon branches to participate in Umklapp scattering (Callaway, 1959). Figure 2·3(a) depicts a 3-phonon scattering process. Phonon-phonon scattering is intrinsic to the material itself and should not change from crystal to crystal.

Phonon scattering on atomic vacancies or isotopes and phonon scattering lattice defects such as dislocations and grain boundaries are scattering mechanisms that depend on the quality of the material. Figure 2·3(b) depicts a phonon scattering on an atomic vacancy while Fig. 2·3(c) a phonon scattering on a grain boundary. These aforementioned phonon scattering mechanisms are common scattering mechanisms for a bulk crystal at room temperature. At lower temperatures or as the size of the crystal begins to decrease, phonon scattering on the surface becomes a major resistance to heat flow (Abeles, 1963; Callaway, 1959; Holland, 1963; Asen-Palmer

et al., 1997). Figure. 2·3(d) shows a phonon scattering on the edge of a crystal.

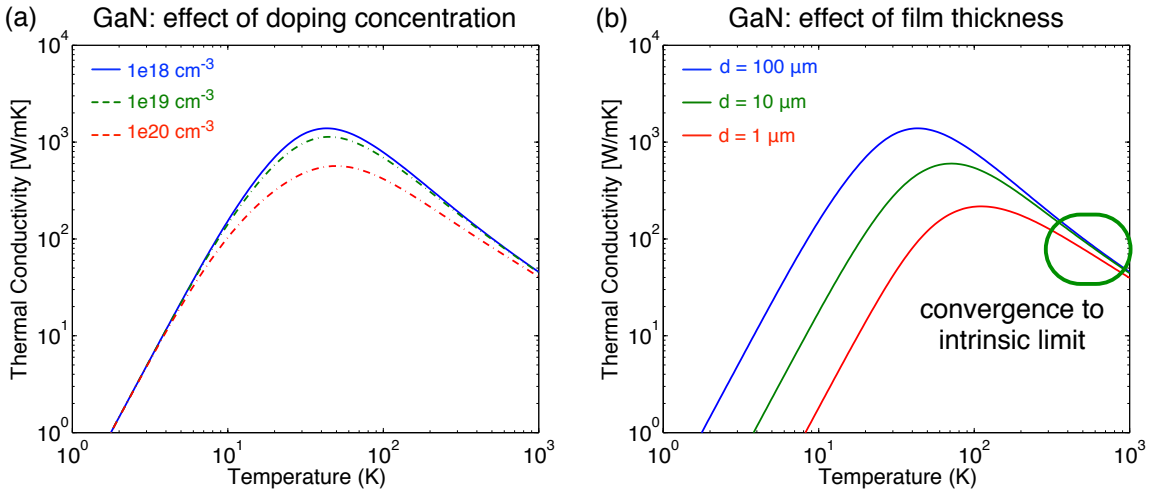

Figure 2·4: Phonon scattering mechanisms as a function of temperature. (a) With an increase in impurity concentration, the thermal conductivity peak shifts predominantly downward. (b) With a reduction in film thickness, d, the thermal conductivity peak strongly shifts to the right along with the low-temperature limit. In both scenarios, the thermal conductivity converges to the intrinsic (bulk) limit due to the dominance of phonon-phonon scattering.

Scattering due to dislocations, defects, and surfaces can be probed by performing thermal conductivity measurements as a function of temperature, with each mechanism identified separately (Abeles, 1963; Callaway, 1959; Holland, 1963; Asen-Palmer et al., 1997). This determination is made possible because various phonon scattering mechanisms dominate in different temperature regimes. For example, the theoretical thermal conductivity of GaN is plotted in Fig. 2·4, using Eq. 2.6 considering phonon-phonon scattering (normal and Umklapp), phonon-isotope scattering, and phonon-boundary scattering as described by Ref. (Asen-Palmer et al., 1997). Figure 2·4(a) shows the effect of increasing the doping (i.e., impurity) concentration for a constant film thickness. When impurity scattering dominates, the thermal conductivity peak reduces and remains at nearly the same temperature. However, in Fig. 2·4(b), when the film thickness is reduced and the impurity concentration held constant, surface

(i.e., boundary) scattering dominates phonon transport and the thermal conductivity peak reduces, with both the peak and the low-temperature limit of thermal conductivity shifting to a higher-temperature value.

2.4 Thermal Boundary Conductance

Thermal boundary conductance is a property of an interface and describes how well heat transfers across an interface. When two dissimilar or similar materials are in contact with one another there a finite temperature drop across the interface. Even at a perfect interface between two materials this occurs due to the mismatch of the acoustic properties of the materials (Swartz and Pohl, 1989). In steady-state heat flow, when the heat carriers at either side of the interface are in equilibrium, we can defined thermal boundary conductance as:

$$q = G\Delta T \tag{2.9}$$

Where q is the total heat flow rate across the interface with units $[W/m^2]$, ΔT is the temperature drop across the interface, and G is the thermal boundary conductance. Typically, thermal boundary conductance is high and can be neglected on the macroscale. However, as we move to the micron and nanoscale, the thermal boundary conductance becomes dominant due to the increasing number of interfaces and as the ratio of surface area to volume increases.

2.4.1 Phonons and Thermal Boundary Conductance

Phonon transport across the interface between two materials has long been one of the most fundamental problems in thermal transport. Even across an ideal interface between two disparate materials, a fundamental limit exists on the thermal boundary conductance (TBC) imposed by a mechanical impedance mismatch (Swartz and Pohl,

1989). This limit, also known as Kapitza resistance, is typically more severe when the two materials have drastically different atomic structures. This mismatch in phonon properties at an interface frequently occurs, such as the deposition of a semiconductor (i.e. GaN) on a high thermal conductivity substrate (i.e. diamond, SiC) in a high power device (Meneghesso et al., 2008; Won et al., 2013; Chou et al., 2004; Bloschock and Bar-Cohen, 2012) and when depositing metal contacts on active semiconductor regions (Majumdar and Reddy, 2004; Dobos et al., 2006; Zhou et al., 2014; Hopkins et al., 2009; Hopkins, 2013; Donovan et al., 2014; Ziade et al., 2015b).

The diffuse mismatch model is often used to model phonon transport across interfaces. The general form for TBC across a solid-solid interface consisting of material 1, to the adjacent solid, material 2, is given by (Swartz and Pohl, 1989):

$$\mathrm{TBC}^{1\to 2} = \frac{1}{4}\sum_{s}\int_{0}^{\omega_{\max,s}} \zeta^{1\to 2}\hbar\omega v_{1,s} D(\omega, v_{1,s})\frac{\partial f_0}{\partial T}d\omega \tag{2.10}$$

where $\zeta^{1\to 2}$ is the transmission coefficient from material 1 to 2, $\omega_{\max,s}$ is the cutt-off frequency for phonon branch s, $\hbar$ is the reduced Planck's constant, D is the density of states, and f_0 is the equilibrium carrier distribution. The most difficult parameter to determine in this formalism is the transmission coefficient (Duda et al., 2010) due to complex scattering that occurs at an interface such as electron-phonon scattering (Majumdar and Reddy, 2004) and the ratio of inelastic and elastic phonon scattering (Hohensee et al., 2015). In general, the transmission coefficient is larger when the overlap between the phonon density of states (DOS) of the two mating materials is greater, thus, permitting more thermal energy to be transported across the interface (English et al., 2012). For example, in Fig 2·5(a) the phonon DOS of aluminum and GaN overlap more than that of aluminum and diamond. Based on the relative overlap, the TBC for Al-GaN is predicted to be five times higher than for Al-Diamond, 670 $\mathrm{MW/m^2K}$ compared to 140 $\mathrm{MW/m^2K}$, respectively. Measurements of these two

interfaces tell a similar story with the TBC of Al-GaN measured to be 100 $\mathrm{MW/m^2K}$ (Donovan et al., 2014) while the TBC of Al-Diamond is 23 $\mathrm{W/m^2K}$ (Monachon and Weber, 2013), and although the correct trend for theory and experiment is observed, the absolute values are quite far off.

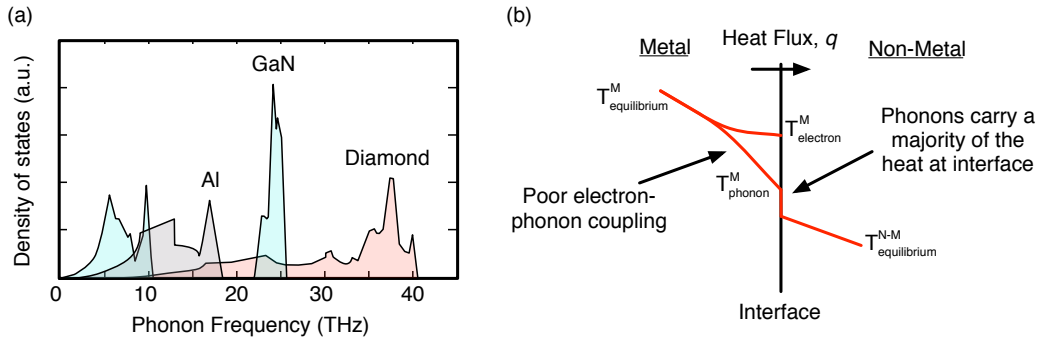

Figure 2·5: (a) DOS for diamond (Hohensee et al., 2015), GaN and Al (Zhou et al., 2013). (b) Temperature profile for electrons and phonons at at metal-nonmetal interface.

In recent years, adjustments to the DMM have been added to correct for phonon transport across interfaces dominated by phonon-phonon scattering, interface mixing and surface roughness (Duda et al., 2013). An excellent review of the DMM and the assumptions used to calculate the transmission coefficient based on phonon-phonon scattering at an interface can be found in Ref. (Duda et al., 2010). However, thermal transport across interfaces remains unclear and thermal transport across interfaces of dissimilar materials remains an active debate in the thermal physics community. For example, weak electron-phonon coupling in metal-nonmetal interfaces.

Electron-phonon coupling in metals is important to understand with regard to metal-nonmetal interfaces (Hohensee et al., 2015), for example, between electrical leads, semiconductor device layers, and heat sinks (Yan et al., 2012). Figure 2·5(b) qualitatively shows the predicted temperatures profiles of electrons (T_e) and phonons (T_p) in the metal and nonmetal (Majumdar and Reddy, 2004). The interface exhibits temperature discontinuities, where the temperature of electrons remains high at the

interface while the lattice temperature of the metal equilibrates to that of the non-metal (Majumdar and Reddy, 2004; Wilson et al., 2013; Yang et al., 2016a). For optical pump-probe thermal measurement techniques samples are typically coated with a metal transducer to absorb laser fluence and heat the sample. Weak electron-phonon coupling in the metal can lead to incorrect modeling of the thermal boundary conductance and lead to incorrect extraction of thermal properties (Wilson et al., 2013). Understanding the physics at the interface between metals and the subsequent layer is critical for proper thermal analysis.

2.5 Summary

In this chapter, we described the basic physical understanding of thermal transport. Phonons were introduced, and gas models based on phonon transmission and scattering were defined. We also introduced the Boltzmann transport equation that uses an ensemble of phonons to calculate macroscopic properties such as thermal conductivity. A method for extracting phonon scattering rates in this ensemble was presented. In the next chapter, we will describe the experimental technique used to measure the important thermophysical properties of thermal conductivity and thermal boundary conductance.

Chapter 3

Frequency Domain Thermoreflectance Microscopy

3.1 Experimental System

Frequency domain thermoreflectance (FDTR) is a state-of-the-art optical measurement technique that enables high-throughput thermal measurements with 400 nm spacial resolution and atomically-thick depth resolution (Yang et al., 2013; Yang et al., 2014; Schmidt et al., 2009; Ziade et al., 2015c; Ziade et al., 2015b; Ziade et al., 2016). The high-throughput nature of FDTR comes from its ability to extract multiple thermophysical parameters from a single sample and measurement (Yang et al., 2016b). This method readily permits the extraction of a thin-film's thermal conductivity and the thermal boundary conductance (TBC) on both sides of the film from a single sample (Ziade et al., 2015b).

In this chapter, we will describe the FDTR system that was constructed in our lab and the heat transfer model used to extract thermal properties. We will then discuss recent advances in FDTR imaging. Recently, FDTR has been extended to imaging, thus allowing 200 by 200 μm^2 thermal property maps. These thermal property maps are quantitative in their information, can help to identify defective regions in specimens, and used to study gradient samples with varying physical properties (Ziade et al., 2015c; Ziade et al., 2016; Ziade et al., 2017). Most of the content about the experimental system and thermal model has been published in Ref. (Yang et al.,

2013; Yang, 2016; Schmidt, 2008).

3.2 Experimental System

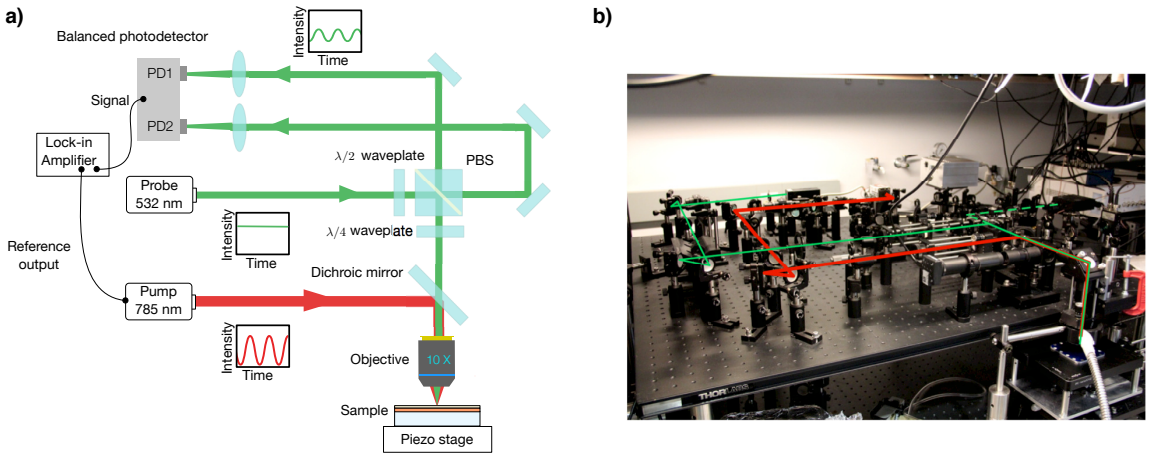

Figure 3·1: FDTR microscope based on two cw diode lasers. (a) Schematic of our setup. The pump laser is directly modulated by the reference output signal from a lock-in amplifier. The lock-in detects the phase lag in the probe signal at the modulation frequency relative to the reference output signal. A balanced photodetection scheme is used to improve the signal to noise ratio. A flip mirror is used to temporarily direct a portion of the pump beam to the signal photodiode PD1 and determine the absolute phase of the pump beam at the sample surface. (b) Picture of the setup built in our lab.

The FDTR system is based on two TEM_{00} free space cw lasers. The schematic and actual system picture are shown in Fig. 3·1(a) and Fig. 3·1(b), respectively. The pump is a 50 mW diode laser (Coherent OBIS 785LX) with a wavelength of 785 nm. We digitally modulate the output power of the pump by modulating the driving current of the laser driver using the signal generated from the output channel of the lock-in amplifier (Zurich Instruments HF2LI). We typically use a sinusoidal signal with a peak-peak voltage of 2V and a frequency range of 10 kHz to 50 MHz as the driving signal. The probe is a 20 mW diode pumped solid state laser with a wavelength of

532 nm. Each beam passes through an optical isolator (Thorlabs IO-5-532-HP for 532nm, Thorlabs IO-3-780-HP for 785 nm) to eliminate back reflection and improve power stability.

The pump beam is reflected by a dichroic mirror (Edmund Optics, hot mirror) and focused onto the sample with a microscope objective, creating a periodic heat flux with a Gaussian spatial distribution on the sample surface. The probe beam is aligned coaxially with the pump beam and focused with the pump spot to monitor the periodic fluctuations in reflectivity at the sample surface caused by the oscillating sample temperature. The coaxial geometry simplifies alignment and enables diffraction-limited beam spot profiles. The sample is coated with a thin metal film, on the order of 80 – 120 nm, which is chosen to maximize the coefficient of thermoreflectance at the probe wavelength (Wilson et al., 2012) and to thermalize a majority of the irradiated electrons (Wilson et al., 2013). For our system, gold gives a large signal at the 532 nm probe wavelength with a coefficient of thermoreflectance of $\sim 2\times10^{-4}$ K^{-1}(Cardenas et al., 2012). The sample is mounted on a closed-loop piezoelectric translation stage (Physik Instrumente) with a 200 μm scanning range in the x, y and z directions and a typical repeatability of $\pm$ 0.01 μm.

We use balanced photodetection to improve the signal-to-noise ratio at low frequencies. This is implemented with a balanced photodetector (Thorlabs PDB410A) comprised of two well-matched photodiodes PD1 and PD2. The probe beam is split with a polarizing beam splitter (PBS). One beam (post-sample) is focused onto the sample and reflected back to PD1, while the other beam (pre-sample) is sent along a matched optical path to PD2. The output currents of PD1 and PD2 are subtracted in the detector and sent through a low-noise transimpedance amplifier, removing common mode noise in the probe beam. Fine balancing is performed by adjusting the half waveplate until the noise is minimized. A translation stage is used to precisely

match the optical path lengths of the pre-sample and post-sample beams for maximum noise rejection. Two bandpass filters (Thorlabs FGB37) are placed before the photodetectors to block scattered pump light, which would otherwise overwhelm the thermal signal.

In our implementation of FDTR, we compare the phase lag of the post-sample probe beam, measured with respect to the reference signal from the lock-in amplifier, against the calculated phase lag of the sample surface temperature to a periodic Gaussian heat source at the sample surface (Schmidt et al., 2009). However, the optical path lengths of the pump and probe beams, driving electronics, and photodetectors all introduce additional frequency-dependent phase shifts into the signal, which collectively we write as ϕ_{ext}. Our approach to account for this external phase shift is to split 1% of the pump beam with a beam sampler and temporarily direct it into the post-sample photodiode with a flip-mirror. We then record ϕ_{ext} over the frequency range of our measurement and subtract this quantity from the measured phase signal before fitting the data to our thermal model. The reference path length should be as close as possible to the total path length from the beam sampler to the sample surface plus the path length from the sample surface to the photodetector. We found that $\sim 5\%$ of the pump light that is reflected from the sample surface leaks through the dichroic mirror. We achieved finding the right reference path length by temporarily removing the 785 nm filters and adjusting the reference path length until the phase signals from the leakage beam and the sampled beam were the same. A translation stage is used to adjust the sampled path until the measured phases agree to within 0.01 degrees at 50 MHz, corresponding to a path length difference of ~ 16 μm.

3.3 Signal Analysis

The extraction of thermal properties is done as an inverse problem, minimizing the difference between the observed and calculated phase lag at different frequencies by adjusting parameters of interest in a thermal model. The model, described in detail in the literature (Schmidt et al., 2009; Schmidt, 2008), gives the frequency response of the sample surface temperature in the diffusion regime in response to a Gaussian heat source on a multilayer stack of materials. A typical measurement configuration is shown in Fig. 3·2. We use five physical parameters for each layer in the sample: the volumetric heat capacity, C_p, the cross-plane and in-plane thermal conductivities, $\kappa_\perp$ and $\kappa_\parallel$, the layer thickness, d, and the thermal boundary conductance to the next layer, G. Thus for an n-layer sample we have $5n-1$ physical properties, of which 1–4 are typically unknown in a given measurement. If the thickness of the bottom layer is greater than the penetration depth of the thermal wave at the lowest frequency, a semi-infinite boundary condition can be used for the final surface and the thickness of the bottom layer d can be made arbitrarily large. Otherwise, the actual thickness of the final layer must be used in the solution, and the boundary condition at the bottom surface can be taken as adiabatic, isothermal or convective, depending on how the sample is mounted. The thermal penetration can be estimated from $\delta_t = \sqrt{2\alpha/\omega_0}$ where ω_0 is the lowest frequency and α is the thermal diffusivity of the bottom layer.

The optical power impinging on the sample from the modulated pump beam at frequency ω is given by $Q_\mathrm{modulation} = (1/2)Q_\mathrm{pump}(1+\cos\omega t)$ where Q_pump is the maximum DC output power of the pump laser. The lock-in amplifier detects the amplitude and phase of the harmonic component of the reflected probe signal at ω. The amplitude of the lock-in voltage is given by

$$|V_\mathrm{LI}| = \frac{1}{2}Q_\mathrm{pump}Q_\mathrm{probe}(1-R_{\lambda_\mathrm{pump}})\left(\frac{dR}{dT}_{\lambda_\mathrm{probe}}\right)G_\mathrm{det}|H(\omega)| \tag{3.1}$$

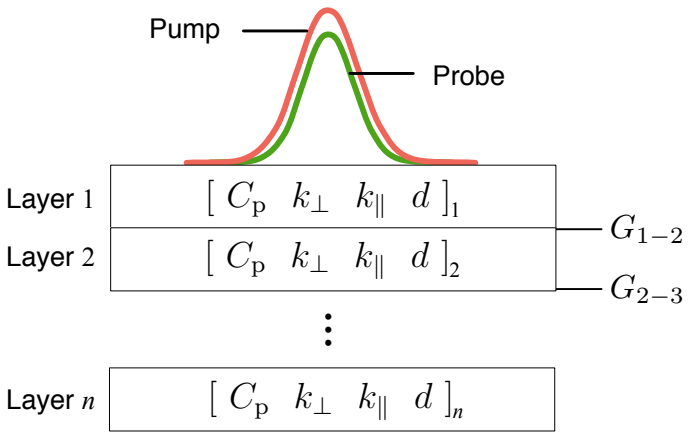

Figure 3·2: Multilayer sample with Gaussian pump and probe spots. For each layer we include the volumetric heat capacity, C_p, the cross-plane and in-plane thermal conductivities, $\kappa_\perp$ and $\kappa_\parallel$, the layer thickness, d, and the thermal boundary conductance to the next layer, G.

where Q_{probe} is the probe power that is impinging on the sample surface, $R_{\lambda_{\text{pump}}}$ is surface reflectivity at the pump wavelength, $\frac{dR}{dT}_{\lambda_{\text{probe}}}$ is the coefficient of thermoreflectance at the probe wavelength, and G_{det} is the product of the transimpedance amplifier gain and the photodiode responsivity at the probe wavelength. $H(\omega)$ is a complex number that represents the frequency response of the sample surface temperature to a periodic heat flux that is absorbed on the surface, weighted by the intensity distribution of the probe beam.

We derived the explicit expression of $H(\omega)$ for a multilayer geometry such as the one shown in Fig. 3·2 from a two-dimensional heat conduction equation. To avoid confusion with the Hankel transfer variable, k, we use Λ to represent the thermal conductivity in the derivation below. κ is used elsewhere in this chapter to denote the thermal conductivity. In a later chapter, k is used to denote wave number. In cylindrical coordinates, the heat conduction equation for each layer of material is given by

$$\frac{\Lambda_r}{r}\frac{\partial}{\partial r}\left(r\frac{\partial\theta}{\partial r}\right)+\Lambda_z\frac{\partial^2\theta}{\partial z^2}=C_p\frac{\partial\theta}{\partial t} \tag{3.2}$$

where θ is the temperature, Λ_r and Λ_z are the in-plane and cross-plane thermal conductivities, respectively, and C_p is the volumetric heat capacity. We find the solution of Eq. 3.2 in the frequency domain following the approach described by Carslaw and Jaegar (Carslaw and Jaeger, 1959). Taking the Fourier transform and Hankel transform of Eq. 3.2, we obtain

$$\Lambda_z \frac{\partial^2 \theta(\omega, k, z)}{\partial z^2} = (\Lambda_r k^2 + C_\mathrm{p} i\omega)\theta(\omega, k, z) \tag{3.3}$$

We let

$$q^2 = \frac{\Lambda_r k^2 + C_\mathrm{p} i\omega}{\Lambda_z}$$

For a layer of material n, the temperature, θ_n, and heat flux, f_n, on the top surface are related to the temperature and heat flux on the bottom surface:

$$\begin{pmatrix} \theta_{n,b} \\ f_{n,b} \end{pmatrix} = \begin{pmatrix} \cosh(qd) & -\frac{\sinh(qd)}{\Lambda_z q} \\ -\Lambda_z q \sinh(qd) & \cosh(qd) \end{pmatrix} \begin{pmatrix} \theta_{n,t} \\ f_{n,t} \end{pmatrix} \tag{3.4}$$

where d is the layer thickness. A thermal boundary conductance G between the bottom surface of layer n and the top surface of the next layer $n+1$ can also be written as a matrix form

$$\begin{pmatrix} \theta_{n+1,t} \\ f_{n+1,t} \end{pmatrix} = \begin{pmatrix} 1 & -G^{-1} \\ 0 & 1 \end{pmatrix} \begin{pmatrix} \theta_{n,b} \\ f_{n,b} \end{pmatrix} \tag{3.5}$$

Combining Eqs. 3.4 and 3.5, we obtain the solution for a multilayer sample through matrix multiplication:

$$\begin{pmatrix} \theta_b \\ f_b \end{pmatrix} = \mathrm{M}_N \mathrm{M}_{N-1} \cdots \mathrm{M}_2 \mathrm{M}_1 \begin{pmatrix} \theta_t \\ f_t \end{pmatrix} \tag{3.6}$$

where M_n, $n = 2, ..., N$ are the matrices from Eqs. 3.4 and 3.5. We let

$$\mathrm{M}_N\mathrm{M}_{N-1}\cdots\mathrm{M}_2\mathrm{M}_1 = \begin{pmatrix} A & B \\ C & D \end{pmatrix}$$

If an adiabatic or semi-infinite boundary condition is applied to the bottom surface of the Nth layer, the surface temperature will be given by

$$\theta_t = \frac{-D}{C} f_t \tag{3.7}$$

The top surface heat flux boundary condition is given by the radial heat flux distribution of the pump beam on the surface:

$$I(r) = \frac{2A_{\text{pump}}}{\pi w_{\text{pump}}^2} \exp\left(\frac{-2r^2}{w_{\text{pump}}^2}\right) \tag{3.8}$$

where A_{pump} is the total absorbed pump power and w_{pump} is the $1/e^2$ radius of the pump beam on the surface. Taking the Hankel transform of Eq. 3.8 we get:

$$I(k) = \frac{A_{\text{pump}}}{2\pi} \exp\left(\frac{-k^2 w_{\text{pump}}^2}{8}\right) \tag{3.9}$$

Inserting Eq. 3.9 into Eq. 3.7, we get surface temperature in the spatial transform domain:

$$\theta_t(k) = \left(\frac{-D}{C}\right) \frac{A_{\text{pump}}}{2\pi} \exp\left(\frac{-k^2 w_{\text{pump}}^2}{8}\right) \tag{3.10}$$

We then get the surface temperature distribution in real space by taking inverse Hankel transform of Eq. 3.10:

$$\theta_t(r) = \int_0^\infty k J_0(kr) \left(\frac{-D}{C}\right) \frac{A_{\text{pump}}}{2\pi} \exp\left(\frac{-k^2 w_{\text{pump}}^2}{8}\right) dk \tag{3.11}$$

where $J_0(kr)$ is the zero-order Bessel function of the first kind. The final thermal response to the system, $H(\omega)$, can now be calculated by multiplying the weighted average of Eq. 3.11 by intensity of the co-axial probe beam with $1/e^2$ radius w_{probe}:

$$H(\omega) = \int_0^\infty \left(\frac{2}{\pi w_{\text{probe}}^2}\right) \exp\left(\frac{-2r^2}{w_{\text{probe}}^2}\right) 2\pi r dr \int_0^\infty k \left(\frac{-D}{C}\right) \frac{A_{\text{pump}}}{2\pi} \exp\left(\frac{-k^2 w_{\text{pump}}^2}{8}\right) dk \tag{3.12}$$

Rearranging and using Eq. 3.8 and Eq. 3.9 we obtain the final form of $H(\omega)$ that we can solve numerically:

$$H(\omega) = \frac{A_{\text{probe}}}{2\pi} \int_0^\infty k \left(\frac{-D}{C}\right) \exp\left(\frac{-k^2(w_{\text{pump}}^2 + w_{\text{probe}}^2)}{8}\right) dk \tag{3.13}$$

The phase data measured by the lock-in amplifier is given by:

$$\phi_{\text{LI}} = \tan^{-1}\left(\frac{\text{Im}\{H(\omega)\}}{\text{Re}\{H(\omega)\}}\right) - \phi_{\text{ext}} \tag{3.14}$$

where ϕ_{ext} is the net external phase introduced by the optical paths and electronic components discussed in section IIA. For analysis, we subtract the measured ϕ_{ext} at each frequency before fitting the lock-in phase data with our model for $H(\omega)$ in Eq. 3.13.

In Fig. 3·3, we show FDTR phase data of fused silica and silicon coated with 100 nm gold and their best fits to the heat transfer model of Eq. 3.14. A least squares algorithm is typically used to find the best model fit. Both the thermal conductivity of the substrate and the thermal boundary conductance of the gold-substrate interface can be extracted from the best fits.

Depending on the number and types of layers in the sample, several combinations of the properties illustrated in Fig. 3·2 may be determined from one FDTR measurement. The number of parameters that can be fit is maximized when the frequency

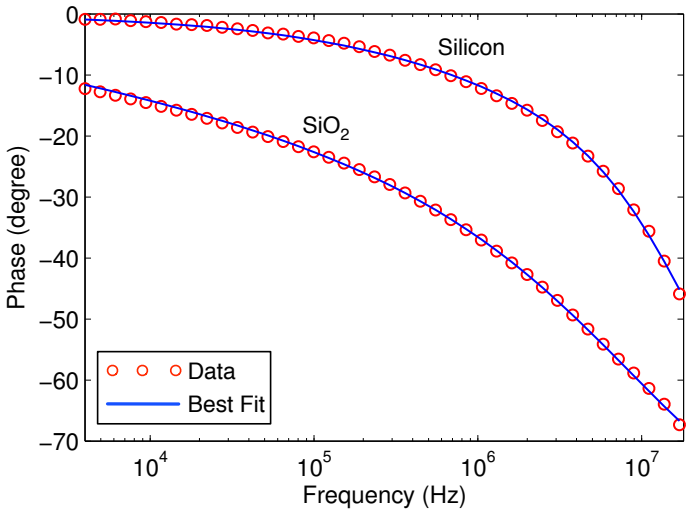

Figure 3·3: FDTR phase data for fused silica and silicon covered by 100 nm gold. The pump and probe spot radii are 5 μm and 1.6 μm, respectively. The best fit of the heat transfer model is also shown for each data set.

range is sufficiently large that the thermal penetration depth $\delta_{\mathrm{p}} = \sqrt{\frac{2\kappa}{C_{\mathrm{p}}\omega}}$ varies from being larger to smaller than the pump laser spot diameter, causing heat flow to transition from a two-dimensional, axisymmetric regime to a one-dimensional regime. In the former, the phase signal depends primarily on the quasi-isotropic thermal conductivity and is sensitive to in-plane transport, while at high frequency the phase is controlled by the thermal effusivity $\sqrt{\kappa C_{\mathrm{p}}}$ and the thermal boundary conductance of the surface layer. For a frequency range of 4 kHz - 50 MHz, δ_{p} varies from 84 μm to 753 nm in silicon (thermal diffusivity = $8.9 \times 10^{-5}\mathrm{m}^2\mathrm{s}^{-1}$ at 300 K) and from 8.2 μm to 73 nm in SiO_2 (thermal diffusivity = $8.46 \times 10^{-7}\mathrm{m}^2\mathrm{s}^{-1}$ at 300 K), so for the majority of materials, spot diameters on the order of a few μm effectively cover the 1D–2D transition.

3.4 Thermal Property Imaging

FDTR was recently extended to obtain thermal properties images, where samples are raster scanned and hundreds of thousands of FDTR measurements are taken to create thermal property maps (Yang et al., 2013). These maps are rich with thermal data, fast to obtain, and valuable in identifying defective regions. We demonstrate FDTR imaging for thermal conductivity measurements of AlN particles embedded in an epoxy. The AlN particles were candidates as filler material for a flexible thermal interface materials. AlN particles were mounted in epoxy by our collaborators at eM-tech and delivered to Boston University. An optical image of a 200 μm by 200 μm area of the sample is shown in Fig. 3·4(a). An SEM of a ion cleaved AlN particle taken by NAMICs is shown in Fig. 3·4(b).

Thermal images are obtained by scanning the sample while recording amplitude and phase data from the lock-in amplifier at multiple frequencies simultaneously. A schematic of our sample with the pump modulate at six frequencies is shown in Fig. 3·4(c). At each pixel a complete FDTR measurement is performed. In Fig. 3·4(d) we plot a 40 point FDTR taken for single-point measurements as well as the six data points taken at each pixel for FDTR imaging. These six data points are chosen based on the sensitivity to the properties of interest. We use phase sensitivity to visualize how much the phase-data varies in the thermal model with respect to the thermal properties. We calculate phase sensitivity, $S(\omega)$, to a parameter x as a function of frequency based on

$$S(\omega) = \frac{\partial \phi(\omega)}{\partial \ln x} \tag{3.15}$$

In Fig. 3·4(e), we show calculated phase sensitivity curves for thermal conductivity of the substrate κ and thermal boundary conductance between the metal transducer layer and the substrate G. The sensitivity to the various properties in the thermal model varies differently from low to high frequency. Based on the sensitivity curves,

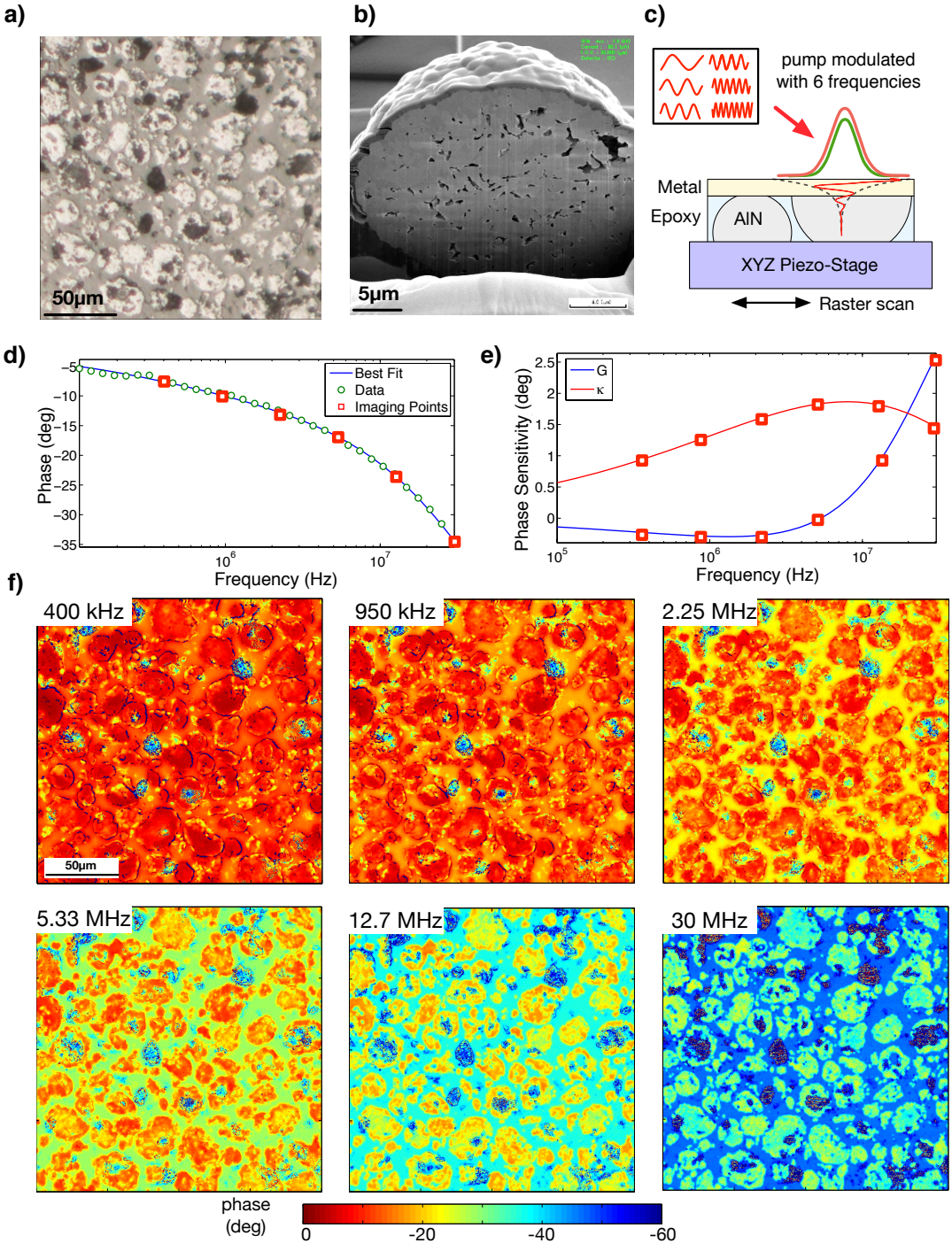

Figure 3·4: (a) Optical image of AlN particles in epoxy. (b) SEM cross section of AlN particle. (c) Sample schematic. (d) Full FDTR measurement and 6 points for FDTR image. (e) Sensitivty plots. (f) Six FDTR phase images.

six frequencies are selected to cover the range where the phase signal is sensitive to both G and κ, including 5.33 MHz, where the sensitivity to G is near zero.

The more frequencies that are scanned for FDTR measurements the more reliable the extracted parameters will be (Joint Committee for Guides in Metrology (JCGM), 2008). However, for FDTR imaging to be fast, we simultaneously modulate the pump at multiple frequencies so that one only needs to scan an area once. For our FDTR imaging setup, we modulate the pump at up to six frequencies at once per scan. Six simultaneously modulated frequencies is the limit because this is the maximum allowed by our lock-in amplifier. At every frequency we obtain both an amplitude and a phase image. Both images show the thermal response of the sample, but typically, the phase image is used for analysis because the interpretation of amplitude images is complicated by variations in the surface reflectivity of the sample and laser power fluctuations.

Figure 3·5(f) shows phase images acquired at these six frequencies with a 50X microscope objective (NA = 0.55), which yielded 0.8 μm and 0.7 μm for the pump and probe radii, respectively. These images are 800 × 800 pixels with a pixel size of 0.25 μm.

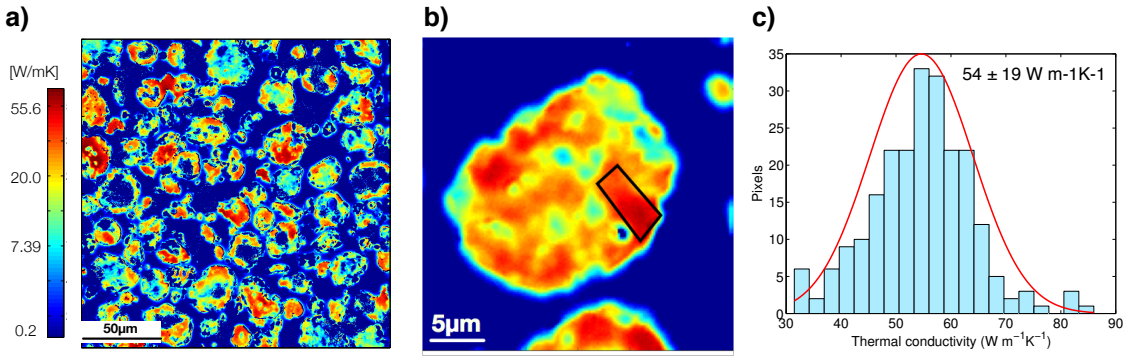

Figure 3·5: (a) Thermal conductivity map of AlN composite (b) thermal conductivity map of select particle and (c) statistical analysis to determine thermal conductivity within the particle.

We fit our phase images to our thermal model and obtain the quantitative thermal conductivity maps as shown in Fig. 3·5(a). A zoomed in view of a single particle is shown in Fig. 3·5(b). We use image statistics to obtain uncertainty in the property values shown in Fig. 3·5(c). We typically pick a region with homogenous property and fit the values with normal distribution. We set the mean as our measured value and the standard deviation as our uncertainty with 68% confidence interval. The uncertainty obtained from the property images depends on the signal to noise ratio. However, in FDTR uncertainty due to modeling parameters, such as the laser spot sizes and metal film properties, lead to a larger overall uncertainty (Yang et al., 2016b).

3.5 Spot Size Characterization

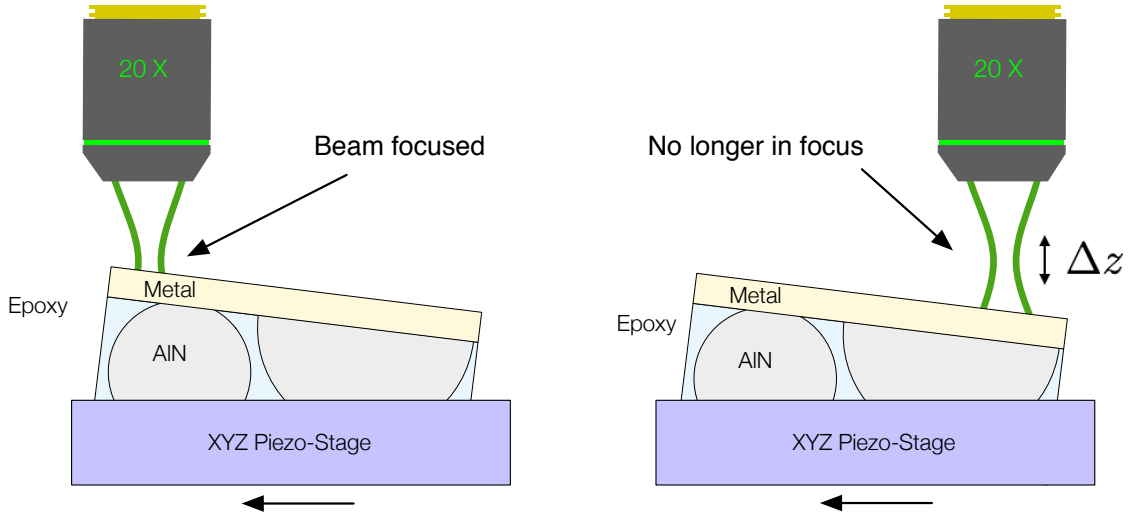

Figure 3·6: Beam geomtery is critical to thermal property extraction. Beam geomtry changes as a sample with an uneven surface is scanned. ΔZ is the allowable tolerance in z before the solution to our thermal model signifantly deviates due to inaccurate beam geometry.

The laser spot size is one of the primary sources of experimental uncertainty in FDTR measurements and must be carefully quantified for accurate extraction of

thermal properties (Schmidt et al., 2009; Malen et al., 2011). The sample must remain within the depth of focus of the objective lens during FDTR measurements to avoid defocusing of the laser spots enough to affect the measurement as seen in Fig. 3·6. Taking a typical tolerance of $w = 1.05w_0$, where w is the spot radius and w_0 is the minimum focused radius, the depth of focus can be determined using Gaussian beam optics: $\Delta z = \pm 0.32\pi w_0^2/\lambda$ where λ is the wavelength, and the minimum spot radius is determined by $w_0 = 0.61\lambda/\mathrm{NA}$ where NA is the numerical aperture (Hecht, 2002). For our 10X objective (NA = 0.25) at the probe wavelength of 532 nm, this yields a depth of focus of $\Delta z = \pm 3.18$ μm, and for our 20X objective (NA = 0.4), $\Delta z = \pm 1.24$ μm.

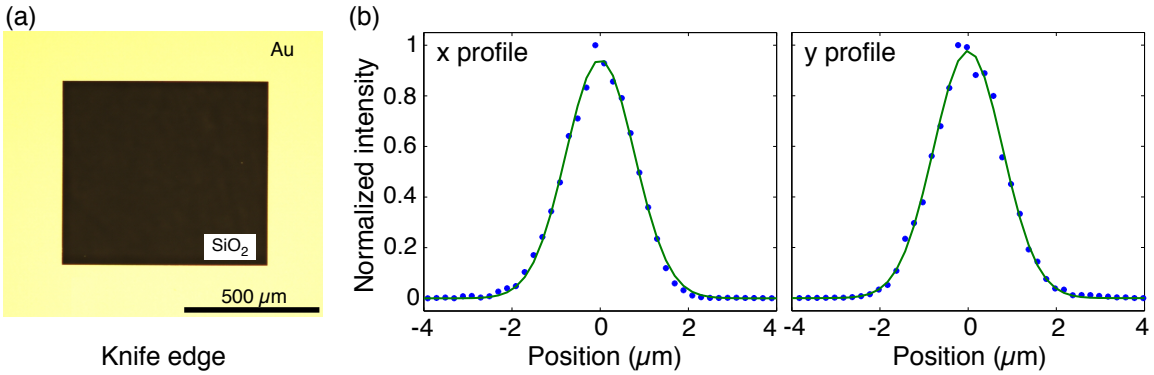

Figure 3·7: (a) Dark field image of the two-dimensional knife-edge pattern fabricated on a glass slide taken by a Nikon optical microscope in the shared clean room in the Photonics Center.(b) Kinfe-edge measurement of the focused probe spot in x and y directions. The $1/e^2$ radius is 1.6 μm in the x direction and 1.6 μm in the y direction.

We use a two-dimensional knife-edge technique to measure both pump and probe laser spot sizes at the focal plane for each microscope objective used in FDTR (Yang et al., 2013). To make the knife-edge sample, we deposited 100 nm gold and 5 nm titanium on fused silica using electron beam evaporation and patterned the gold film with a square transparent window using photolithography and lift-off techniques. The

optical image of the fabricated knife-edge sample is shown in Fig. 3·7(a). The sample surface is treated with oxygen plasma after fabrication to remove any photoresist residue. During the spot size measurement, the knife-edge sample is mounted on a closed-loop piezoelectric stage and positioned in the focal plane of the objective lens. The piezoelectric stage scans the sample in two dimensions with a repeatability of $\pm$ 0.01 μm and the transmitted light is measured with a photodetector placed underneath as shown in Fig. 3·8(a). We perform this measurement multiple times across different regions on the knife edge in both x and y directions for both the pump and probe laser beams to account for any error in the sharpness of the knife edge.

Figure 3·7(b) shows an example of our probe spot profile with a 10$\times$ objective, where the $1/e^2$ radius is 1.6 μm in the x and y directions. The $1/e^2$ radius is calculated as follows. The Gaussian intensity profile, I, in the radial direction r of a laser spot is given by:

$$I(r) = \frac{2A_0}{\pi w_0}\exp\left(\frac{-2r^2}{w_0^2}\right) \tag{3.16}$$

where A_0 is the total power and w_0 is the $1/e^2$ radius, the total transmitted power recorded by the photodetector when the knife-edge is scanning in the x direction is:

$$P(x) = \frac{2A_0}{\pi w_0}\int_{-\infty}^{\infty} dy\, \exp\left(\frac{-2y^2}{w_0^2}\right)\int_{-\infty}^{x} dx\, \exp\left(\frac{-2x^2}{w_0^2}\right) \tag{3.17}$$

We fit the spatial derivative of the photodetector output with a Gaussian profile in both the x and y directions to extract the $1/e^2$ radius of our pump and probe spots as shown in Fig. 3·7(b).

To ensure consistent spot size characterization from the knife edge measurements to sample measurements we develop a quantitative technique to determine the focal plane. Previously, we relied solely on using a CCD camera to visually identify the focal plane. Now, however, we verify the focal plane after adjusting the sample height

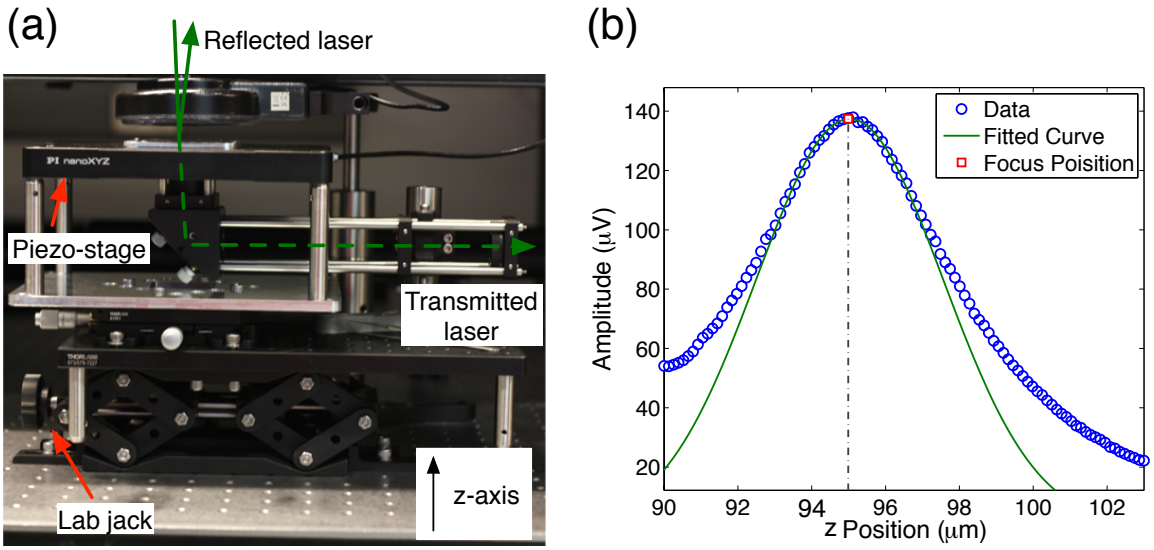

Figure 3·8: (a) Picture of our sample holding setup (b) Dat from the autofocusing technique. The blue dots are the measured amplitude of the probe beam μV as the piezo stage steps in the z-axis. A curve is then fitted to the data and the maximum of the curve is taken as the focus spot.

visually, we find the focal plane by maximizing the thermal signal. For this, we step the height of the sample using the piezostage until the amplitude of thermal signal is maximized. Finding the focus by maximizing the thermal signal provides a qualitative method of focusing enabling automatic focusing.

For automatic focusing, the piezo stage is set to 100 μm and the height of the sample is adjusted using the lab jack until the laser spots appear to be focused on the sample surface from the CCD camera. We modulate the pump laser at a frequency above 1MHz. Then the piezostage, which is directly connected to the lock-in, steps in small increments of z relative to the laser spot size. After each step in z, the piezostage sends a pulse to the lock-in to record a data point. The height of the piezostage and the phase and amplitude of the reflected probe beam are recorded. The amplitude of the probe beam in μV is plotted as a function of the piezostage height, z, as shown in Fig. 3·8(b). The data is then normalized and fit to a Gaussian

curve. The maximum value of the fitted curve is used to determine the focal plane. Practically, the Gaussian fit is done to reduce noise. This allows for the use of a low time constants on the lock-in and the autofocusing process to take only a couple of seconds. The ability to quickly focus is important especially for FDTR imaging of samples that are not perfectly flat.

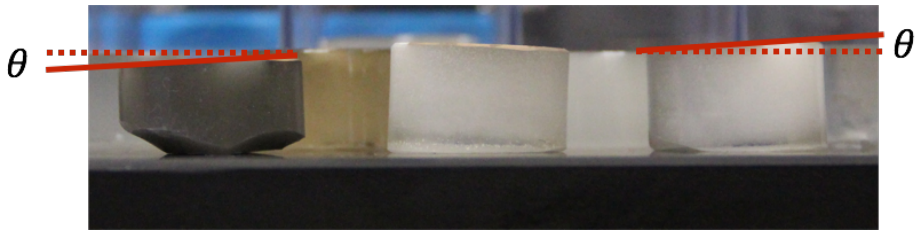

Figure 3·9: Actual measured samples mounted in epoxy. They are uneven.

Figure 3·9 shows actual samples measured in this thesis. These samples are not flat and raster scanning of the sample while keeping the z-plane fixed results in significant change in beam geometry as seen in Fig. 3·6. As previously mentioned for our 10X objective the depth of focus is approximately $\Delta z = \pm 3.18$ μm, and for our 20X objective $\Delta z = \pm 1.24$ μm. This means while scanning over the full range of the piezo stage, 200 μm, the sample must not vary in z by a distance greater than a couple microns.

To overcome this tight tolerance we take advantage of our qualitative autofocusing method and develop a technique to keep the sample in focus during the imaging process. We do this by finding a plane to define the sample surface and stepping the z plane with steps in x and y such that:

$$z(x, y) = c_1 \times x + c_2 \times y + c_3 \tag{3.18}$$

where c_1, c_2, and c_3 are constants that define the plane of a sample surface. An example of this method is shown in Fig. 3·10. Four points are chosen across the

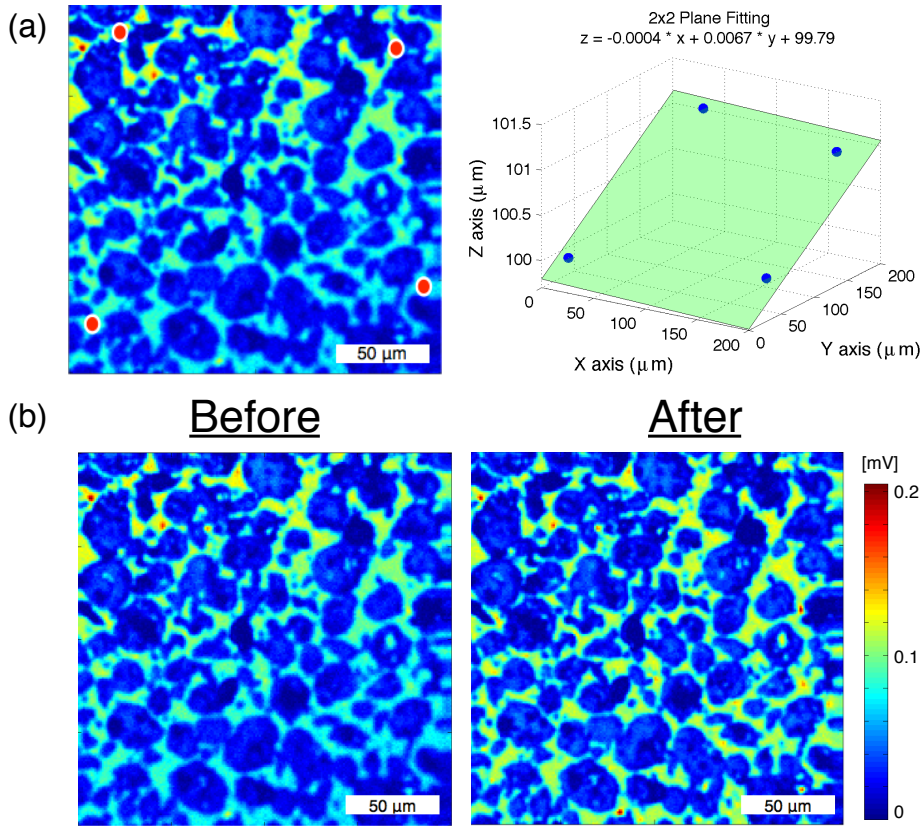

Figure 3·10: (a) The user can select points on the four corners to perform a plane fit to the sample. The formula for z(x,y) is inputed into the piezo stage so that the sample is always within the focal plane. (b) A reflection image taken before autofocusing and after autofocusing. The laser defocuses from top to bottom of the image and sharpness is lost.

sample by the user after a quick 200 by 200μm^2 image is taken. Four points are chosen by the user, although, the four corners of the image could be used automatically. A plane is fit through the four points chosen and an equation for z is calculate. The image is taken again and the sample stays within the focal plane of the objective seen in Fig. 3·10(b). In the before image it is clear that the beam is defocusing from the top of the image to the bottom. It should be clear that in the after image the beam geometry is constant and there is no shift from the top to the bottom of the image.

3.6 Temperature dependent measurements

Temperature dependent measurements were done by placing the sample inside a commercially bought MMR Joule Thompson refrigerator. A picture of the refrigerator is shown in Fig. 3·11(a). For measurements, the chamber is evacuated with the MMR recommended and included scroll pump capable of reaching a vacuum as low as 5 mTorr.

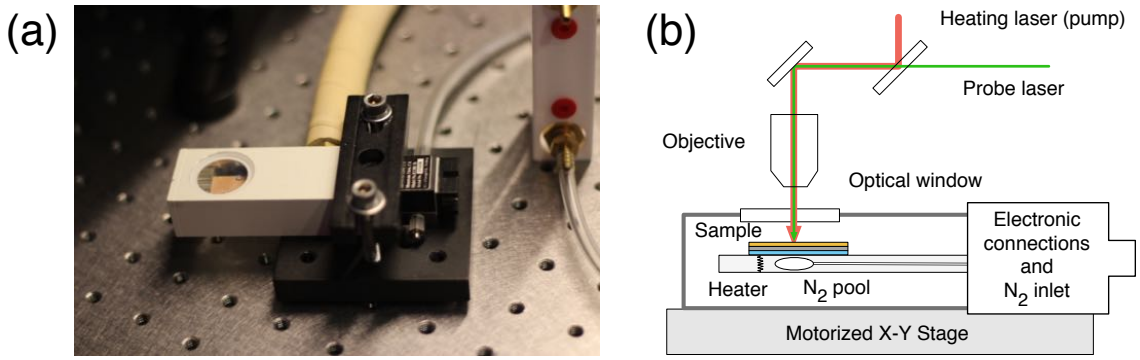

Figure 3·11: (a) Joule Thompson refrigerator from MMR Technologies.(b) Schematic of operation using the refrigerator.

The MRR refrigerator has a temperature range of 77 – 730 K. High temperatures are achieved with a resistive heater located underneath the sample. Low temperatures are achieved by the expansion of compressed nitrogen at the cold finger. The nitrogen, which was originally at a pressure greater than 1800 psi, expands rapidly and forms a pool of liquid nitrogen under the sample cooling the sample to 77K. This solid state setup provides for a low vibration environment for thermal measurements. Unfortunately, we were only able to use the system for measurements from 300 – 730 K because of ice formation on the sample surface. At temperatures below 273 K, ice particles form on the sample. This is seen in the optical images shown in Fig. 3·12 at 300K, 270K and 150K.

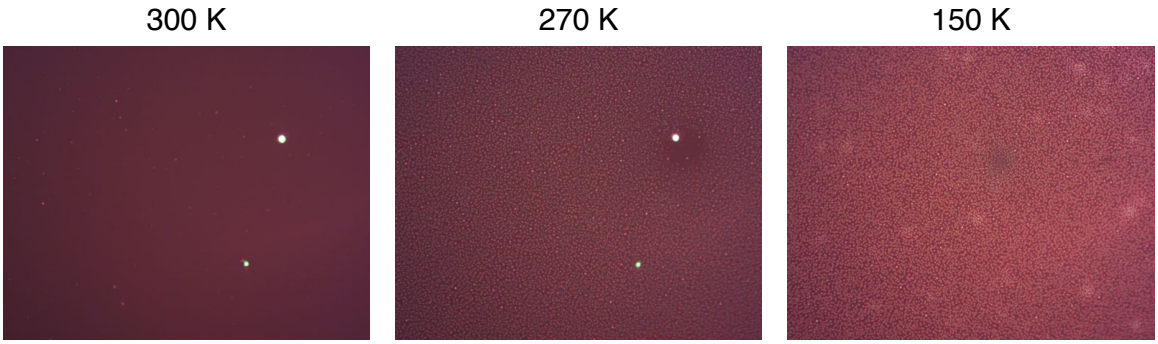

Figure 3·12: Particles form on sample as soon as it is cooled below room temperature. Chamber pressure was 5mTorr.

3.7 Software

We developed software based on Matlab shown in Fig. 3·13 to generate FDTR single-point data and FDTR images. This graphical user interface makes our data acquisition both convenient, easy to use, and efficient. The backend of the this software synchronizes the lock-in amplifier and piezostage. The user is able to take a reference 200 by 200 μm^2 image in approximately 5 minutes. From the image the user can select the autofocusing points, select a region for high-resolution image acquisition, or to select an array of points for single-point FDTR measurements. The software also communicates with the MMR temperature stage for automated temperature dependent measurements.

One of the major improvements of FDTR imaging developed while writing this software was the enhancement of imaging time. This was achieved by continuously scanning the stage while acquiring data from the lock-in. The lock-in amplifier and piezostage were synchronized using a trigger pulse from the piezostage. The trigger pulse was spaced depending on the filter integration time of the lock-in such that 99% of the data in each pixel was new. The remaining 1% of the data is from the memory in the previous pixel. This insured that the maximum amount of data was collected and

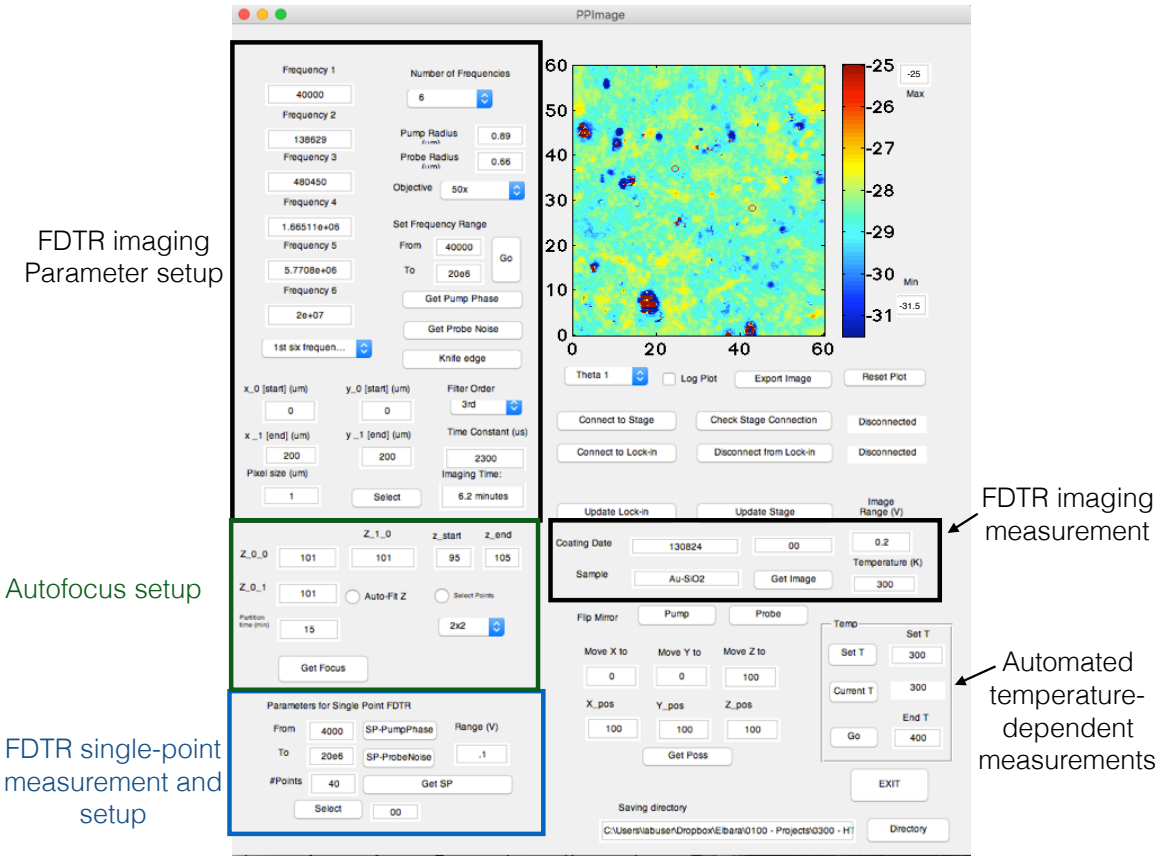

Figure 3·13: Matlab software used to generate FDTR data. Both single point measurements and images can be created the software.

that no commands to clear the buffer of the lock-in were required. Such improvements allowed for an order of magnitude decrease in imaging times compared to our previous imaging algorithm, which flushed the lock-in buffer and did not continuously scan the sample.

3.8 Summary

We have described an FDTR experimental system based on cw lasers that incorporates balanced photodetection to give a large signal-to-noise ratio for frequencies from 4 kHz to 50 MHz. We applied an exact analytical model for diffusive heat flow in

a multilayer sample, including radial heat transfer and the effect of finite laser spot sizes. Using this model, we computed the sensitivity of the thermal phase signal to various properties as a function of modulation frequency. The sensitivities are used to select a set of imaging frequencies that allow us to simultaneously fit multiple properties from a small number of images, which we acquire by scanning the sample while modulating the pump laser with up to six frequencies at once. AlN particles embedded in epoxy were measured to demonstrate our technique, and maps of thermal conductivity were obtained by simultaneously fitting phase images acquired at six frequencies. An autofocusing algorithm was presented to ensure that beam geometry is consistent while performing FDTR imaging.

Chapter 4

Thermal Conductance of Nanoscale Langmuir-Blodgett Films

Hybrid structures of organic and inorganic materials are widely used in devices such as batteries, solar cells, transistors, and flexible electronics (Choi et al., 2008; Chen et al., 2009; Arora and Zhang, 2004; Briseno et al., 2006; Forrest, 2004; Song and Evans, 2000; Hoppe and Sariciftci, 2004). As these devices continue to miniaturize and develop, a clear picture of thermal transport at the organic–inorganic interface becomes critical to thermal management. It is difficult to model transport across such interfaces due to their complex bonding and large mismatch in atomic structure (Malen et al., 2010; Ong et al., 2014; Ong, 2015). In this chapter, we describe how the Langmuir-Blodgett (LB) technique can be used to experimentally determine the thermal interface conductance between polymers and solid substrates.

4.1 Organic-Inorganic Interfaces

It is a challenge to directly probe the thermal interface conductance between polymers and inorganic materials due to the low thermal conductivity of most polymers. To experimentally isolate the thermal interface conductance, the thickness of the polymer film must be close to its Kapitza length, which is on the order of a few nanometers (Losego et al., 2010). It is therefore necessary to fabricate nanometer-thick polymer films. While techniques such as spin casting and grafting can be used to make polymer films as thin as 2 nm (Losego et al., 2010; Shin et al., 2002; Liu et al., 2014),

they offer limited control over the film structure. The LB technique offers a way to repeatedly deposit nanometer-thick films at different phases with a varying degree of chain ordering (Garcia-Manyes et al., 2007; Agarwal, 1988; Albrecht et al., 1978; Ulman, 1991). Depositions at different phases are achieved by controlling the lateral surface pressure of the polymer film on a liquid bath. For LB deposition with a water bath, an amphiphilic polymer is deposited on the air-water interface to form a monolayer. By dipping a chip through the polymer monolayer into the water bath, the polymer is transferred onto the chip while preserving its structure from the water surface (Ni et al., 2006; Zhai and Kleijn, 1997). Multiple dips will lead to thicker polymer films. In this chapter, we describe how we used the LB technique to study the thermal conductivity and thermal interface conductance of poly(vinyl acetate) (PVAc) on silicon and gold substrates. We chose PVAc because of its many uses in industry and its ability to form homogeneous films with the LB technique (Ohkita et al., 2005).

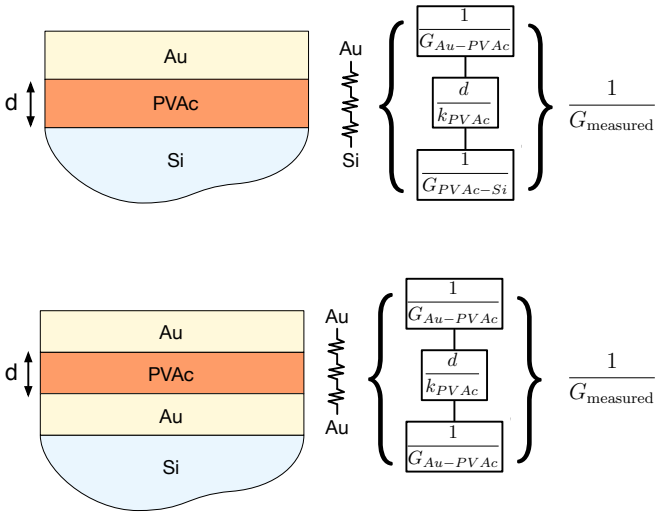

Figure 4·1: Sample schematics and thermal resistance model.

We extracted the thermal interface conductance by fabricating multiple chips with

different polymer thicknesses, coating them with a thin gold film, and then measuring the total thermal conductance to the substrate using Frequency Domain Thermoreflectance (FDTR) (Schmidt et al., 2009). For this work we fabricated two sequences of chips with variable polymer thickness. The first set of depositions was done on a gold-coated silicon wafer, while the second set was done on a bare silicon wafer. The two types of samples are shown schematically in Fig. 4·1. By plotting the measured thermal conductance, $G_{measured}$, as a function of the polymer film thickness, we can isolate the thermal interface conductances between PVAc-Au and PVAc-Si using the thermal circuit models given in Eq. 4.1 and 4.2. These equations assume zero interfacial resistance between successive dips and give an effective value for the polymer films thermal conductivity.

$$\frac{1}{G_{\text{measured}}} = \frac{1}{G_{\text{Au-PVAc}}} + \frac{d}{k_{\text{PVAc}}} + \frac{1}{G_{\text{Au-PVAc}}} \tag{4.1}$$

$$\frac{1}{G_{\text{measured}}} = \frac{1}{G_{\text{Au-PVAc}}} + \frac{d}{k_{\text{PVAc}}} + \frac{1}{G_{\text{Si-PVAc}}} \tag{4.2}$$

4.2 Nanometer-Thick Polymer Film Fabrication

Silicon chips were cleaned by sonication in acetone, methanol, isopropyl alcohol, and deionized water for five minutes each to remove organic contaminants. We coated half of the Si chips with 100 nm of gold by electron-beam evaporation, along with fused silica and silicon reference samples that were used to characterize the gold film. PVAc with a weight average molecular weight of 121,700 and a number average molecular weight of 52,700 was purchased from Sigma Aldrich (St. Louis, MO) and used without further purification. The polymer was dissolved into toluene (>99%, Sigma Aldrich) to obtain a final concentration of 1% by weight. 10μl of the solution was dispersed on the air-water interface in a Langmuir trough (NIMA, UK) with a surface area of 500cm^2, forming a monolayer. The temperature of the deionized water bath was kept

constant at 10°C. We waited at least 15 minutes before proceeding to ensure that the toluene evaporated from the water surface. We then compressed the monolayer at a rate of 40 mm^2/s and monitored the mean lateral pressure (Π) of the monolayer with a Wilhelmy plate. A typical compression curve, or isotherm, is shown in Fig. 4·3(a).

We conducted depositions at two different polymer phases, indicated with red circles in Fig. 4·3(a). The phase corresponding to the larger area per polymer is called the Liquid expanded (Le) phase while the phase corresponding to the smaller area per polymer is called the Liquid condensed (Lc) phase (Ni et al., 2006). Once the PVAc monolayer reached the desired point on the isotherm curve, we dipped the chips at a speed of 0.05 mm/s while maintaining a constant Π. We deposited polymer films on the chips using 1–7 dips. The thickness (Garcia-Manyes et al., 2007) and roughness of the resulting PVAc film on bare silicon were measured using Atomic Force Microscopy (AFM) as shown in Fig.4·2. Four AFM images of PVAc on silicon are shown in Fig. 4·3(b). We see that the Lc films tended to be more disorganized with larger peaks and valleys. After the first dip, the Le chips tended to have an ordered structure with a domain size of approximately 100 nm, shown in the five-dip Le image. The results for thickness and roughness vs. the number of dips for the silicon chips are plotted in Fig. 4·3(c) and 4·3(d).

We can see from Fig. 4·3(c) and Fig. 4·3(d) that the Lc films are significantly rougher than the Le films and exhibit more variability in film thickness. We note that thickness does not always increase linearly with the number of dips. In a few instances, dips in the Lc phase did not increase the film thickness, only the measured roughness, e.g. dips 5–7 in Lc batch 1 and dip 3 of Lc batch 3, indicating that an incomplete film deposition occurred. Because of the larger variation and inconsistent deposition in the Lc phase compared to the Le phase, we performed an additional batch of Lc depositions and 1-2 additional dips per Lc batch. We assumed that the

thickness of the polymer on the gold-coated substrate was the same as on the silicon chips.

Depositions in the Lc phase were done at an area of 40 nm^2/polymer and resulted in a film thickness of 5.4 $\pm$ 0.9 nm for one dip, while depositions in the Le phase were done at 80 nm^2/polymer and had a thickness of 1.3 $\pm$ 0.1 nm for one dip. This indicates that the single-dip Lc polymer film has approximately 50% the density of the Le film. A possible explanation for this might be that the radius of gyration of PVAc, which is close to 10nm (Van Krevelen and Te Nijenhuis, 2009), is much larger than the monolayer thickness of our films. We believe that in the Le region, PVAc self assembles into large area domains. As we continue to compress the film, the domains remain but more free volume is created as they are pushed together and detach from the water surface, as shown schematically in the inset of Fig. 4·3(a). This is consistent with previous simulations (Müller, 2002) and experiments (Soles and Ding, 2008) that predict confined polymer thin films do not continue to compress but instead fold onto themselves and limit interchain entanglement.

4.3 Thermal Conductance Measurements

We coated the polymer samples with gold and used FDTR to measure the thermal conductance, G_{measured}, from the gold to the substrate (gold or silicon). We performed a single parameter fit to determine G_{measured}. The properties of the gold films were obtained separately by measurements of reference samples. We fit Eq. 4.1 to the data for the gold substrates to extract $G_{\text{PVAc}-\text{Au}}$ and the thermal conductivity of the PVAc on gold. Then using $G_{\text{PVAc}-\text{Au}}$, we fit Eq. 4.2 to the data for the silicon substrates to extract $G_{\text{PVAc}-\text{Si}}$ and the thermal conductivity of the PVAc on silicon. The results are plotted in Fig. 4·4 and summarized in Table 4.1.

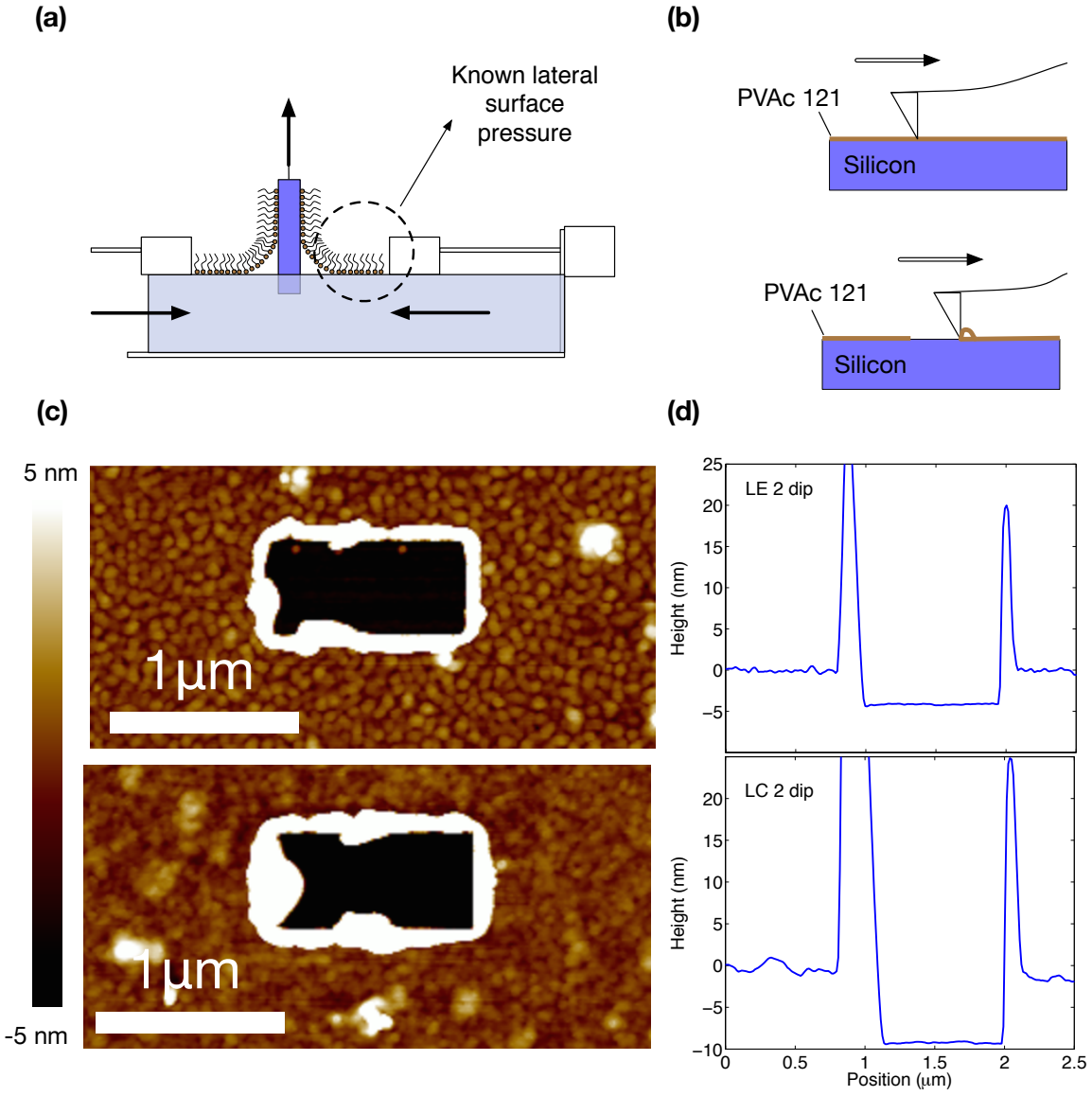

Figure 4·2: (a) Schematic of LB technique to deposit nanometer-thick polymer films (b) AFM scratch method to determine the thickness of the polymer film (c) AFM height graph after the film has been scratched (d) the resulting thickness measurement

4.4 Results and Discussion

The thermal conductivity values for both the Lc and Le phases are higher than the value for bulk PVAc, 0.16 W/mK (Van Krevelen and Te Nijenhuis, 2009). We

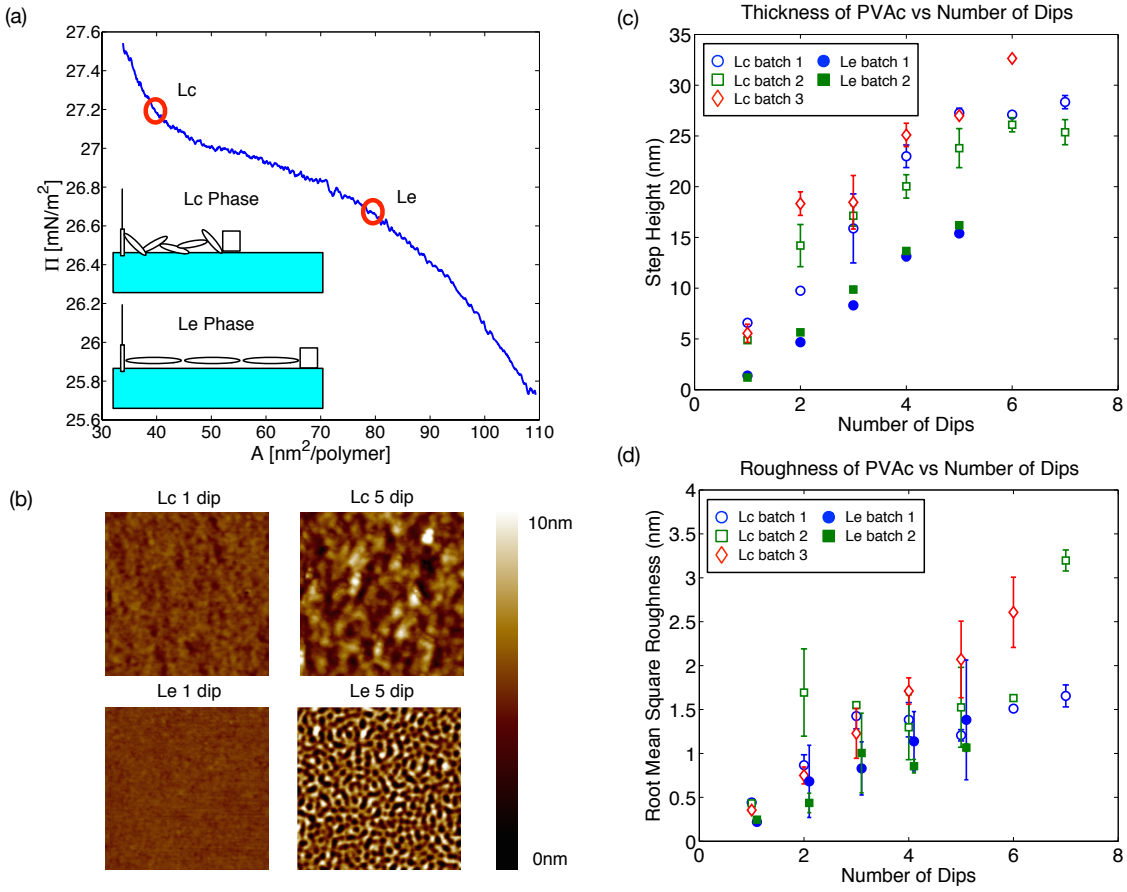

Figure 4·3: a) Isotherm of PVAc at 10°C. Red circles highlight the Lc and Le phases. The inset shows a schematic of the Lc and Le structure on the water surface. b) AFM micrographs of one and five dips of PVAc films on Si in the Lc and Le phase. The images are 2μm by 2μm. c) PVAc film thickness vs. number of dips. Chips fabricated in the Lc phase have a higher variation in thickness when compared to those fabricated in the Le phase d) PVAc film roughness vs. number of dips. The closed shapes represent chips fabricated in the Le phase and the open shapes represent chips fabricated in the Lc phase

believe this is due to reordering and chain alignment in films thinner than 6-10x the bulk radius of gyration (Tomczak et al., 2004). We expect that thick PVAc films fabricated with multiple LB dips of 1-5nm of polymer film per deposition will have a higher degree of chain ordering than bulk PVAc, and will therefore not achieve

Table 4.1: Calculated effective thermal conductivity (k), thermal interface conductance (G), calculated DMM, and the corrected DMM in parenthesis

Sample	k [W/mK]	G [MW/m^{2}K]	DMM [MW/m^{2}K]
Le PVAc-Si	0.34 ± 0.05	69.3 ± 17.1	43 (52)
Lc PVAc-Si	0.23 ± 0.02	74.9 ± 18.1	43 (52)
Le PVAc-Au	0.27 ± 0.02	80.8 ± 9.4	350 (95)
Lc PVAc-Au	0.21 ± 0.01	93.6 ± 18	350 (95)

the bulk value for thermal conductivity without annealing. When we compare the Le and Lc films, we find that the Le films exhibit 48% and 30% higher thermal conductivity than the Lc films on silicon and gold, respectively. From kinetic theory, thermal conductivity, k, relates to density through $k = \frac{1}{3}\rho c_p v \Lambda$, where v is the average velocity of the heat carriers, ρ is the density, and Λ is the mean free path (Chen et al., 2005). This may explain the higher thermal conductivity of the more dense Le phase compared to the Lc phase.

Our results show that the thermal interface conductance of the Lc phase is slightly higher than the Le phase on both substrates. Additionally, the thermal interface conductance is higher for PVAc-Au than PVAc-Si. To gain some insight, we used the Diffuse Mismatch Model (DMM) to calculate $G_{\mathrm{PVAc-Au}}$ and $G_{\mathrm{PVAc-Si}}$ (Swartz and Pohl, 1989). We computed the DMM using measured temperature-dependent volumetric heat capacity of the two materials (Bellis et al., 2000), and assumed single event, fully diffuse, and elastic phonon scattering at the interface, which implies that phonons will scatter once at the interface but may scatter into different phonon branches (Duda et al., 2010). The thermal interface conductance is then given by

$$G_{\mathrm{DMM}} = \left(\frac{v_{1D}^3 \sum_j v_{1,j}^{-2} \sum_j v_{2,j}^{-2}}{12(\sum_j v_{1,j}^{-2} + \sum_j v_{2,j}^{-2})} \right) \rho_1 c_{p,1}(T) \tag{4.3}$$

where $\rho_1 c_{p,1}(T)$ is the volumetric heat capacity of material 1 at temperature T, $v_{i,j}$

is the phonon velocity in material i for the jth phonon mode, and $v_{1,D}$ is the average phonon velocity in material 1. Bulk values for PVAc were used in this calculation because it is difficult to predict the phonon velocities based on density alone due to additional changes in stiffness of thin polymer films (Soles and Ding, 2008). The parameters used for the DMM calculation are given in Table 4.2.

Table 4.2: Values used to calculate DMM. Obtained from Refs. (Haynes, 2015; Swartz and Pohl, 1989; Ashcroft, N.W. and Mermin, 1976) for Gold and Silicon and Refs. (Van Krevelen and Te Nijenhuis, 2009; Buchenau and Wischnewski, 2004; Hong et al., 2011; Sakaguchi et al., 2005) for PVAc.

	c_p (J/kg K)	ρ (g/cm^3)	V_l (m/s)	V_t (m/s)	Θ_D (K)
Gold	129	19.3	3390	1290	170
Silicon	713	2.33	8970	5332	640
PVAc	1470	1.19	2492	1370	105

The DMM is known to under-predict or over-predict G based on the ratio of the Debye temperatures, Θ_D, of the two materials (Norris and Hopkins, 2009). Therefore, we compute adjusted DMM values using an empirical correction, Z, based on the Debye temperature ratios of our materials (Ziade et al., 2015b) where:

$$Z = 0.157 \left(\frac{\Theta_{D,1}}{\Theta_{D,2}} \right)^{-1.127} \tag{4.4}$$

and

$$G_{\text{corrected}} = G_{\text{DMM}} \times Z \tag{4.5}$$

For PVAc, we used the Debye temperature reported for Poly(vinylethylene) because of its close chemical structure to PVAc (Sakaguchi et al., 2005). Our DMM values are reported in the last column of Table 4.1, with the adjusted values given in parenthesis. We see that the DMM predicts $G_{\text{PVAc-Au}}$ to be larger than $G_{\text{PVAc-Si}}$ due to their more closely matched phonon properties. With the correction factor we

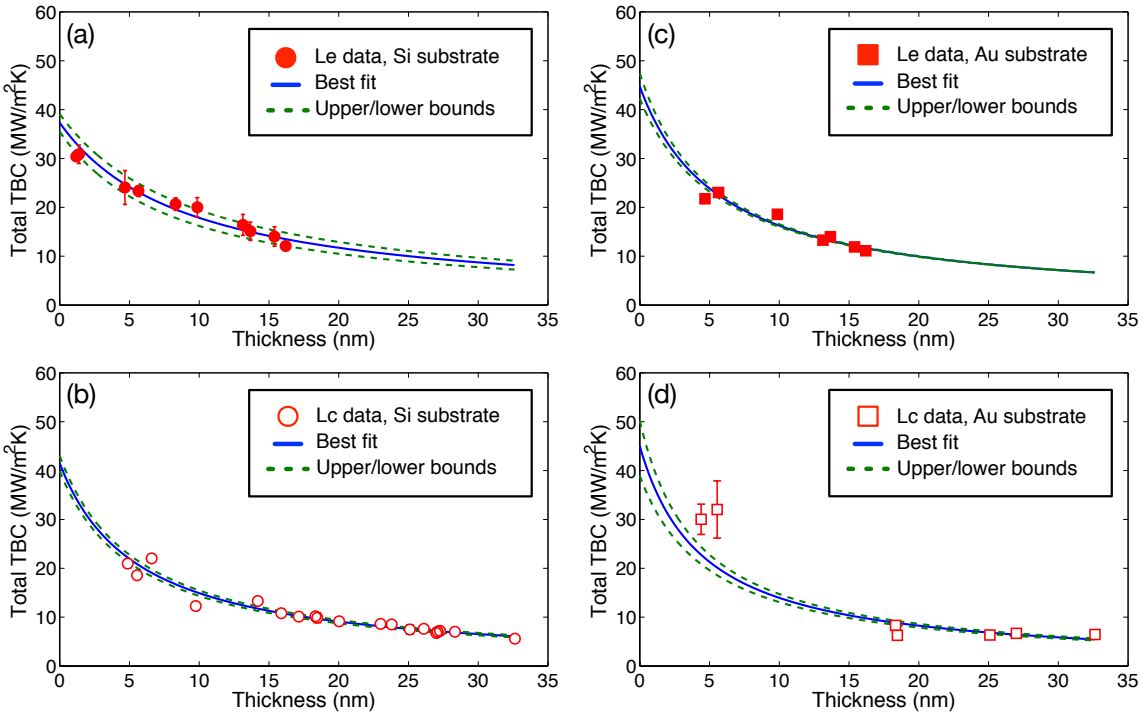

Figure 4·4: Total interface conductance (G_{measured}) as a function of film thickness for the Lc and Le phases on Si (circles) and Au (squares). The solid blue line is the best fit curve to the mean measured values while the dashed green lines are the best fit curves for the upper and lower values of the error bars.

calculate the DMM within a factor of two of the measured value.

The resistor model with constant thermal conductivity is generally in good agreement with the data. The outliers in Fig. 4·4(d) are possibly Lc films that were discontinuous. We note that chips with a similar thickness of PVAc resulted in similar values for G_{measured}, regardless of the number of dips it took to achieve that thickness. This indicates that PVAc films formed by multiple dips can be treated as a single homogenous layer. However, if we assume that the films have a regular layered structure caused by multiple dips, we can estimate the thermal interface conductance between successive dips i and $i+1$ by including thermal resistances of the form $G^{-1}_{i\rightarrow(i+1)}$ in the resistor model from Eq. 4.1 and Eq. 4.2. If we assume that

the layers have the same thermal conductivity as bulk PVAc, this results in negative values for the thermal interface conductance between layers, indicating that the film thermal conductivity must be higher than bulk, possibly due to a higher degree of chain ordering. We can calculate a lower bound on the thermal interface conductance between successive dips i and $i+1$ by assuming that the polymer film has an infinite thermal conductivity, such that $G_{i\rightarrow(i+1)} = (G^{-1}_{\text{measured},i} - G^{-1}_{\text{measured},i+1})^{-1}$. This results in $G_{i\rightarrow(i+1)} \sim 100$ MW/m^{2}K for the Le films. The dip-to-dip conductance computed this way for the Lc films is inconsistent due to the variation in the amount of polymer deposited in each dip, ranging from $\sim$1,500MW/m^{2}K when the thickness did not significantly increase from a dip to as low as 28MW/m^{2}K when the thickness increased by $\sim$5 nm. This suggests that a single homogenous layer is a better model than a layered structure for these films, unlike regular structures of alternating organic-inorganic interfaces with sharp interfaces formed by molecular beam epitaxy (Liu et al., 2013a).

4.5 Summary

In conclusion, the LB technique is an effective method for studying the thermal interface conductance between polymers and substrates. We found that the thermal conductivity of the LB films was up to two times the value for bulk PVAc, with the Le phase exhibiting higher thermal conductivity than the Lc phase. The thermal interface conductance was on the order of 70 MW/m^{2}K between PVAc and silicon, and 90 MW/m^{2}K between PVAc and gold, with the Lc phase exhibiting slightly higher thermal interface conductance. The LB approach can be applied to study thermal transport at the interface between many combinations of polymers and substrates, and may be useful for designing composite materials and microelectronic devices that incorporate polymers. The work presented in this chapter has been published in

Applied Physics Letters (Ziade et al., 2015a).

Chapter 5

Wide bandgap Semiconductor: GaN

5.1 Thermal Transport Through GaN–SiC Interfaces from 300 to 600 K

Gallium Nitride is a wide bandgap semiconductor that has attracted significant interest for many microelectronics applications including high electron mobility transistors, which are promising for next-generation RF devices operating beyond 200 GHz, amplifiers and power converters (Albrecht et al., 2010; Rosker, 2007; Su et al., 2013b). Performance of these devices at high frequencies is limited by heat removal to the substrate (Meneghesso et al., 2008; Won et al., 2013; Chou et al., 2004; Bloschock and Bar-Cohen, 2012). Silicon carbide is used as a substrate for high-power GaN-based transistors (Albrecht et al., 2010) and blue LEDs (Brummer et al., 2015) because of its high thermal conductivity and closely-matched lattice spacing to GaN. In these devices heat flow from GaN to SiC is limited by the thermal boundary conductance (TBC) between the two materials (Cho et al., 2014). It is important to minimize the temperature rise in GaN devices because an increase in temperature will reduce GaN transistors channel electron mobility, the maximum drain current, increase the gate leakage, and further degrade the lifetime of the device (Xu et al., 2007; Meneghesso et al., 2008). However, despite the importance of heat transfer across the GaN–SiC interface, there have been no measurements of the TBC of GaN grown directly on SiC without a transition layer. In this section, we present measurements in the temperature range of 300–600 K of the TBC of 640 nm GaN heteroepitaxially grown on

SiC.

5.1.1 Sample Preperation

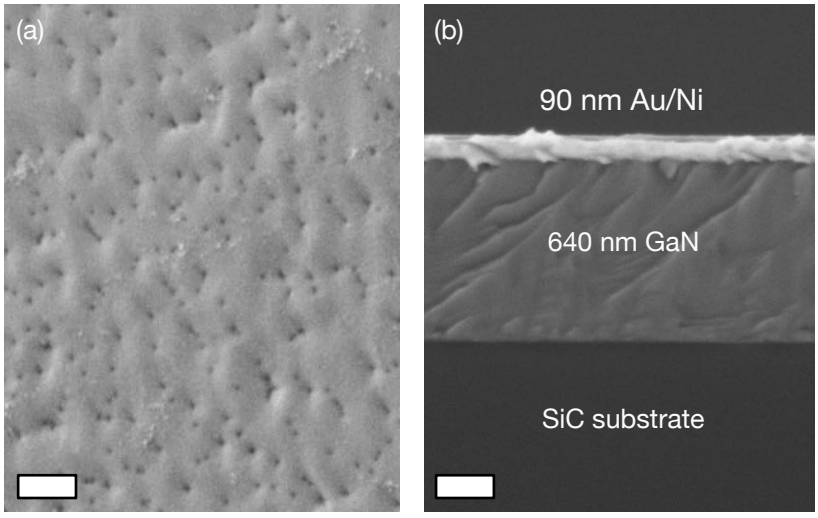

Figure 5·1: (a) SEM micrograph of GaN surface used to calculate the dislocation density (b) SEM micrograph of the cross-section of GaN coated with Au/Ni transducer for the FDTR measurement. Scale bar is 200 nm.

The GaN film was grown by RF plasma-assisted MBE in a Veeco GEN-II MBE system. Nitrogen activation was achieved with a Veeco UNI-Bulb RF plasma source operated at 300 W and flow rate of 1.2 sccm. The substrate was 4H-SiC which was doped p-type with a resistivity of 0.25 Ω-cm and miscut 8 degrees towards the <11-20> planes. Before growth, the substrate was degreased and etched sequentially in 3:1 H_2SO_4:H_2O_2 solution and HF. Nickel was deposited by electron beam evaporation on the backside (C-face) of the substrate to assist bonding to a silicon carrier wafer (also coated with Ni) with InGa solder. Finally, the substrate was cleaned in the MBE growth chamber by multiple cycles of Ga deposition and evaporation. The GaN was grown directly on the Si-face of the SiC under slightly Ga-rich conditions. Under these

growth conditions, GaN with the metal-polar orientation was grown. We estimated the dislocation density of this thin GaN film (see Fig. 5·1(a)) to be approximately 8×10^{9} cm^{-2} from high-magnification Scanning Electron Microscope (SEM) images such as the one shown in Fig. 5·1(a). The thickness of the GaN was measured to be 640 ± 10 nm via the cross-sectional SEM micrograph shown in Fig. 5·1(b).

5.1.2 Sample Characterization

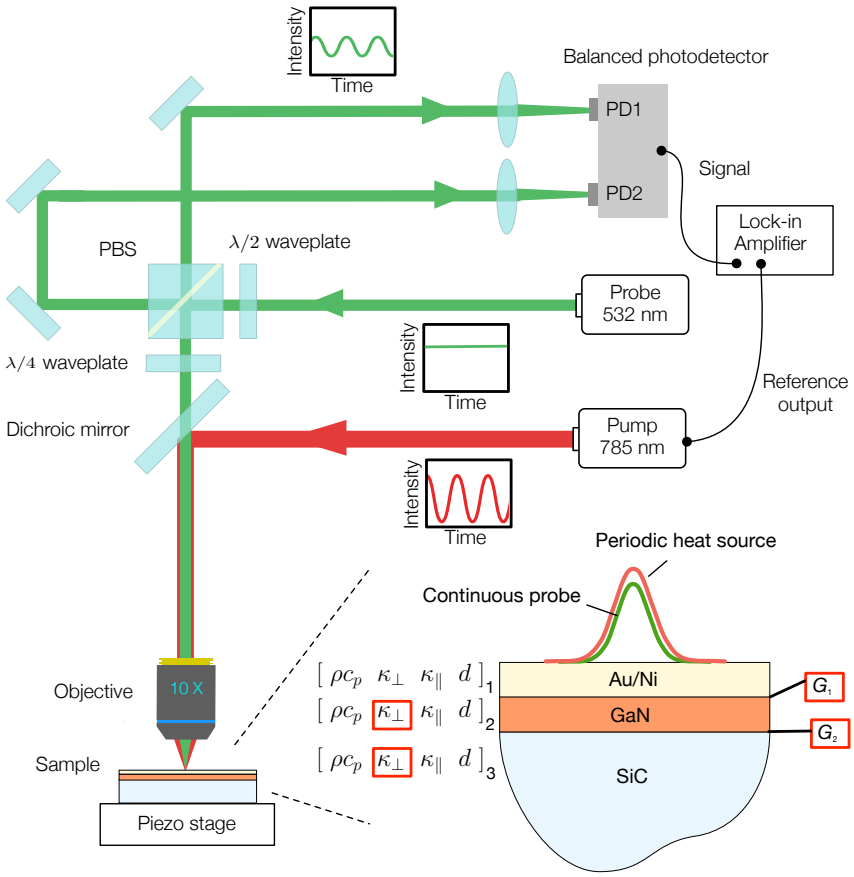

Figure 5·2: FDTR schematic and sample configuation. Each of the four fitted parameters are higlighted with a red box.

We used frequency domain thermoreflectance (FDTR) to characterize the thermal properties of the GaN sample (Schmidt et al., 2009). A schematic of our setup,

described in Ref. (Yang et al., 2013), is shown in Fig. 5·2. The GaN sample was coated with a 5 nm Ni adhesion layer and an 85 nm Au transducer layer with electron beam deposition at a nominal pressure of 1 μTorr. A periodically modulated pump laser was focused to a Gaussian spot to locally heat the sample while an unmodulated probe laser beam measured the surface temperature through a proportional change in the reflectivity of gold. We varied the pump beam modulation frequency from 100 kHz to 50 MHz. A lock-in amplifier recorded the amplitude and phase response of the reflected probe beam. The $1/e^2$ radii of the pump and probe beams were 2.8 μm and 2.3 μm, respectively, at the sample surface. The FDTR measurements were performed in vacuum (<5 mTorr) in 15 degree increments from 300 to 600 K. Unknown thermal properties were extracted by minimizing the error between the measured probe phase lag at each frequency and an analytical solution to the heat diffusion equation in a multilayer stack of materials (Schmidt et al., 2009).

The investigated sample is modeled as three layers as shown in Fig. 5·2. Each layer is characterized by five physical parameters: the volumetric heat capacity (ρc_p), the cross-plane thermal conductivity ($\kappa_\perp$), the in-plane thermal conductivity ($\kappa_\parallel$), the layer thickness (d), and the TBC to the next layer (G). We performed a four-parameter fit of the thermal model to the measured phase data to extract the thermal conductivity of GaN ($\kappa_{\perp,\mathrm{GaN}}$), the thermal conductivity of SiC ($\kappa_{\perp,\mathrm{SiC}}$), the TBC between Au/Ni–GaN ($G_{\mathrm{Au/Ni-GaN}}$), and the TBC between GaN–SiC ($G_{\mathrm{GaN-SiC}}$). Prior to measurements of the GaN sample, we characterized the Au/Ni transducer layer.

Several reference samples of fused silica were co-deposited with the GaN chip to determine the thermal properties of the Au/Ni transducer layer. The total thickness of the Au/Ni layer was measured by atomic force microscopy on a reference glass slide to be 91 $\pm$ 1.5 nm. The temperature dependent values of κ and ρc_p of Au/Ni from 300 to 600 K were determined by FDTR measurements of the reference samples

using literature values of κ and ρc_p for fused silica (Cahill, 1990; Touloukian, Y S ; Buyco et al., 1970). We show the measured values of Au/Ni at 300 K in the first row of Table 5.1. The standard deviations given are from five measurements at different locations on the sample.

Table 5.1: Parameters used to calculate the sensitivity at 300 K. Literature value for ρc_p for GaN was obtained from Ref. (Lee et al., 2011), ρc_p for SiC from Ref. (Hitova et al., 2000) and $\kappa_\parallel/\kappa_\perp$ for SiC from Ref. (Su et al., 2013a).

	ρc_p [MJ/m^{3}K]	$\kappa_\perp$ [W/mK]	$\kappa_\parallel/\kappa_\perp$	d [nm]
Au/Ni	2.44 ± 0.1	115 ± 5	1	91 ± 1.5
GaN	2.61 ± 0.08	130	1	640 ± 10
SiC	2.13 ± 0.06	370	1.16 ± 0.1	-

5.1.3 Results and Discussion

In Fig. 5·3 we plot the FDTR measurement sensitivity to the four fitted parameters of the investigated sample: $\kappa_{\perp,\mathrm{GaN}}$, $\kappa_{\perp,\mathrm{SiC}}$, $G_{\mathrm{Au/Ni-GaN}}$ and $G_{\mathrm{GaN-SiC}}$. Sensitivity to a property x is computed as $\partial\phi/\partial \ln x$, where ϕ is the phase calculated from the thermal model (Schmidt et al., 2009). The properties used to calculate the sensitivity are given in rows 2 and 3 in Table 5.1. We assume an isotropic thermal conductivity of GaN based on first principal calculations by Lindsay *et al.* (Lindsay et al., 2012). We use an in-plane to cross-plane ratio of 1.16 for 4H-SiC (Su et al., 2013a), where our cross-plane direction is parallel to the C-axis of SiC. Values for the cross-plane thermal conductivities of GaN and SiC are taken from Ref. (Levinshtein et al., 2001). For the two interfaces of Au/Ni–GaN and GaN–SiC, we used 120 MW/m^{2}K and 200 MW/m^{2}K, respectively. The sensitivity to each parameter in Fig. 5·3 follows a

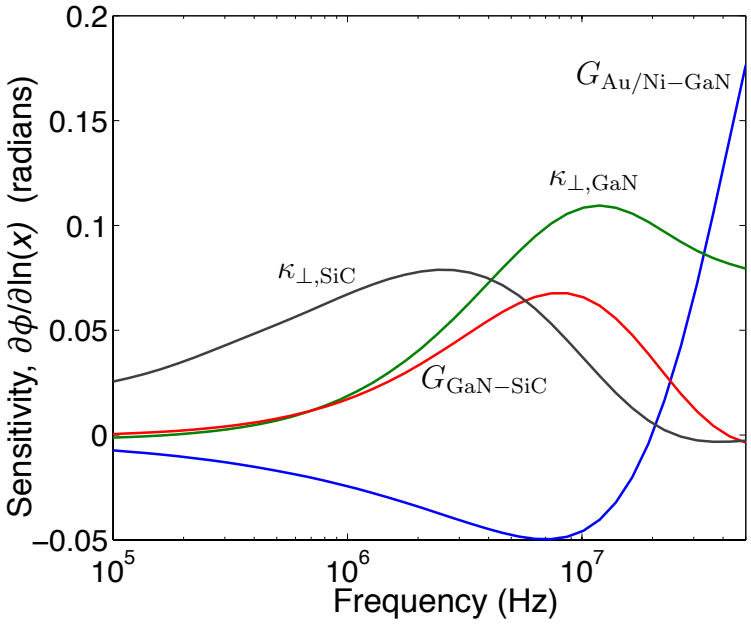

Figure 5·3: Sensitivity plot a four parameter fit. Sensitivty to property x is calculated from $\partial\phi/\partial \ln x$.

different trend, indicating that it is possible to extract these four parameters with least square minimization. The measurement results are plotted in Fig. 5·4.

We implemented a Monte Carlo method in Matlab to verify the uniqueness of the four fitted parameters and determine the error bars shown in Fig. 5·4. Each known parameter in the thermal model was assumed to have a normal distribution about a mean value with a standard deviation. The heat capacity values obtained from literature were assumed to have a standard deviation of 3%, while the anisotropic ratio of SiC was given a standard deviation of 10%. For the Au/Ni transducer layer, the standard deviation values were obtained from multiple measurements of the reference sample. In each iteration of the Monte Carlo simulation, the program randomly generated values for the known parameters based on their distributions and performed a nonlinear least squares fit of the thermal model to the measured data. The resulting distributions of best-fit values obtained from 2000 iterations were fit with normal

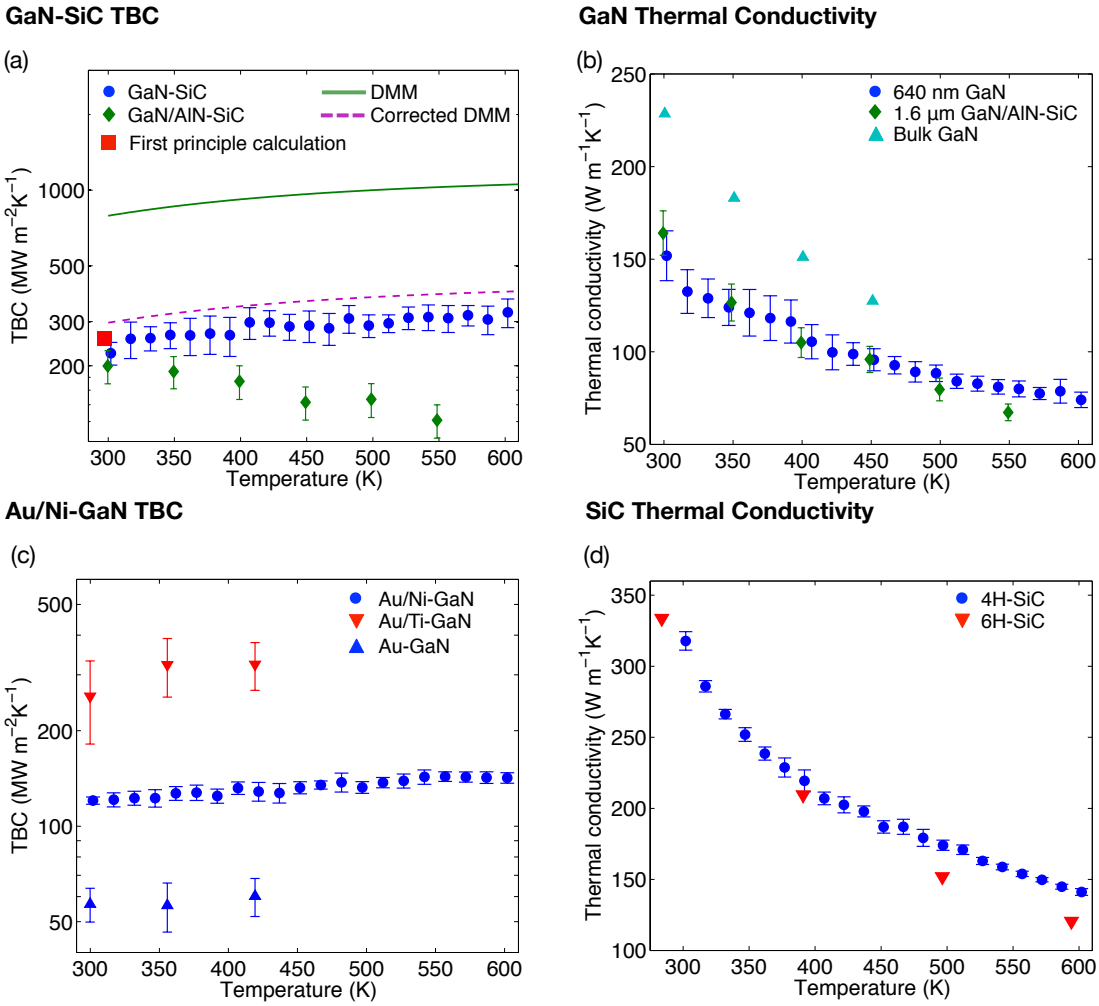

Figure 5·4: Measured values for (a) $G_{\mathrm{GaN-SiC}}$, (b) $\kappa_{\perp,\mathrm{GaN}}$, (c) $G_{\mathrm{Au/Ni-GaN}}$, and (d) $\kappa_{\perp,\mathrm{4H-SiC}}$. References included are (a) $G_{\mathrm{GaN/AlN-SiC}}$ (Cho et al., 2012); first principle calculations (Kazan, 2009) (b) 1.6 μm GaN (Cho et al., 2012) and bulk GaN (Mion et al., 2006) (c) Au/Ti–GaN and Au–GaN (Donovan et al., 2014) (d) 6H-SiC (Nilsson et al., 1997).

distributions. We report the mean as the measured value and the standard deviation as the uncertainty with a 68% confidence interval (Beckwith et al., 2007).

DMM Modeling

Measured values for the TBC of GaN–SiC are compared to the Diffuse Mismatch Model (DMM) in Fig. 5·4(a). The DMM is used to predict the TBC when phonons are the dominant heat carriers in the two materials and the majority of scattering at the interface is diffuse, which is the case for the temperature range of this study (Swartz and Pohl, 1989). We implement the DMM for GaN–SiC as described by Bellis *et al.* (Bellis et al., 2000). This variant of the DMM uses the measured temperature-dependent heat capacity of the two materials instead of phonon density of states estimated from the Debye model. This model also assumes single event, fully diffuse, and elastic phonon scattering at the interface. This implies that phonons will scatter once at the interface but may scatter into different phonon branches (Duda et al., 2010). The TBC is calculated as:

$$G_{\mathrm{DMM}} = \left(\frac{\zeta^{1\to 2} v_{1D}^3}{12} \sum_j v_{1,j}^{-2} \right) \rho c_{p,1}(T) \tag{5.1}$$

where $\rho c_{p,1}(T)$ is the volumetric heat capacity of material 1 at temperature T, $v_{i,j}$ is the phonon velocity in material i for the jth phonon mode, $v_{1,D}$ is the average phonon velocity in material 1, and $\zeta^{1\to 2}$ is the transmission coefficient from material 1 to 2, given by:

$$\zeta^{1\to 2} = \frac{\sum_j v_{2,j}^{-2}}{\sum_j v_{1,j}^{-2} + \sum_j v_{2,j}^{-2}} \tag{5.2}$$

Phonon velocities for this calculation in the [0001] direction of GaN and SiC are taken from Ref. (Levinshtein et al., 2001) and are reported in Table 5.2.

The DMM is known to under-predict or over-predict the TBC depending on the ratio of the Debye temperatures of the two materials (Norris and Hopkins, 2009). In our case, the DMM over-predicts the TBC of GaN–SiC. To adjust the DMM, we performed a logarithmic fit of data for many material pairs presented by (Norris and

Table 5.2: GaN and SiC properties used to calculate DMM. Values are taken for waves propagating in the [0001] direction from Ref. (Levinshtein et al., 2001).

	v_t [m/s]	v_l [m/s]	v_{avg} [m/s]	Θ_D [K]
GaN	8040	4130	4750	600
SiC	13100	7100	8120	1300

Hopkins, 2009) and obtained an empirical correction factor:

$$Z = 0.157 \left(\frac{\Theta_{D,\text{film}}}{\Theta_{D,\text{substrate}}} \right)^{-1.127} \tag{5.3}$$

which is used to modify Eq. 1 according to

$$G_{\text{modified}} = Z \times G_{\text{DMM}} \tag{5.4}$$

We plot this modified DMM for $G_{\text{GaN-SiC}}$ in Fig. 5·4(a). In addition, we show results from a more detailed calculation by Kazan that accounts for surface scattering and roughness (Kazan, 2009). Our calculated and measured values for $G_{\text{GaN-SiC}}$ increase with temperature, which is expected due to the participation of more phonon modes. We also plot the results of a previous measurement by Cho *et al.* (Cho et al., 2012) of GaN grown on SiC with a 36 nm AlN transition layer. The total TBC values for the GaN–AlN–SiC interface decrease with increasing temperature, which may be due to crystal imperfections in the AlN transition layer that scatter phonons at the GaN–AlN and AlN–SiC interfaces, and the decreasing thermal conductivity of AlN as temperature increases (Cho et al., 2012; Su et al., 2013c).

In Figures 5·4(b-d) we plot the remaining three fitted parameters along with values from literature. Figure 5·4(b) shows our measured thermal conductivity for 640 nm GaN along with values for bulk GaN from (Mion et al., 2006) and a 1.6 μm

thick GaN film from (Cho et al., 2012). Our results for GaN grown on SiC are comparable to GaN grown on SiC with an AlN transition layer. This suggests that the AlN transition layer, which is meant to decrease the dislocation density in GaN (Cho et al., 2014), may not improve the thermal conductivity of the GaN film. Figure 5·4(c) shows our measured values of $G_{\mathrm{Au/Ni-GaN}}$, $G_{\mathrm{Au-GaN}}$ (Donovan et al., 2014), and $G_{\mathrm{Au/Ti-GaN}}$ (Donovan et al., 2014). Finally in Fig. 5·4(d), we plot our measured values for $\kappa_{\perp,\mathrm{SiC}}$ of 4H-SiC and literature values for the 6H-SiC polytype (Nilsson et al., 1997).

5.1.4 Summary

In conclusion, we have presented the first measurements of the TBC between GaN and 4H-SiC with no transition layer from 300–600 K. We found that the TBC between GaN–SiC increases with temperature and is generally greater than the TBC for GaN grown on an AlN transition layer. The work presented in this chapter has been published in Applied Physics Letters (Ziade et al., 2015b).

5.2 Thickness Dependent Thermal Conductivity Of Gallium Nitride

As the gate size of GaN-based transistors decreases to achieve higher operating frequencies, the thermal transport properties of GaN are expected to degrade due to size effects as well as boundary, dislocation, and impurity scattering of phonons (Chou et al., 2004; Bloschock and Bar-Cohen, 2012; Won et al., 2013; Cahill et al., 2014). It is important to understand the role of these various scattering mechanisms in order to engineer GaN films that can effectively dissipate heat. Despite the importance of characterizing thermal transport in submicron GaN films, the literature remains unclear on the dominant phonon scattering mechanisms.

In this section, we present thermal conductivity measurements of a GaN film 15–

1000 nm thick that was heteroepitaxially grown directly on 4H-SiC without a transition layer. We used frequency domain thermoreflectance (FDTR) to measure both the GaN film thermal conductivity and the thermal boundary conductance (TBC) between GaN and an Au/Ni metal contact. A Monte Carlo technique was used to compare the results of a one- and two-parameter fit of these properties, indicating an enhancement in TBC for thickness below 150 nm. In order to understand the dependence of thermal conductivity on film thickness, we first measured the thermal conductivity of 1 μm-thick GaN in the temperature range of $300 < T < 600$ K to extract the impurity scattering rate, and then incorporated this into a Boltzmann Transport Equation (BTE) model.

5.2.1 Sample Preperation

The GaN film was grown on a 4H-SiC substrate with a Veeco GEN-II RF plasma-assisted molecular beam epitaxy system. Nitrogen activation was achieved with a Veeco UNI-Bulb RF plasma source operated at 300 W and flow rate of 1.2 sccm. The 4H-SiC was miscut 8 degrees towards the <11-20> planes and was p-type doped with a resistivity of 2.5 Ω-cm. Metal-polar oriented GaN was grown directly on the silicon-face of the SiC under slightly gallium-rich conditions. A portion of the substrate was covered with a molybdenum clip that slowed the growth of GaN in the surrounding region as seen in Fig. 1(a), resulting in a region with a thickness gradient from 15-1000 nm.

5.2.2 Sample Characterization

The thickness and surface quality of the GaN film were determined by optical profilometer, Fig. 5·5(a), and SEM images, Fig. 5·5(b), respectively. Thickness was also determined with AFM measurements of the GaN film relative to the two scratches seen in Fig. 5·6(d). A magnified SEM and profilometer image of the two scratches

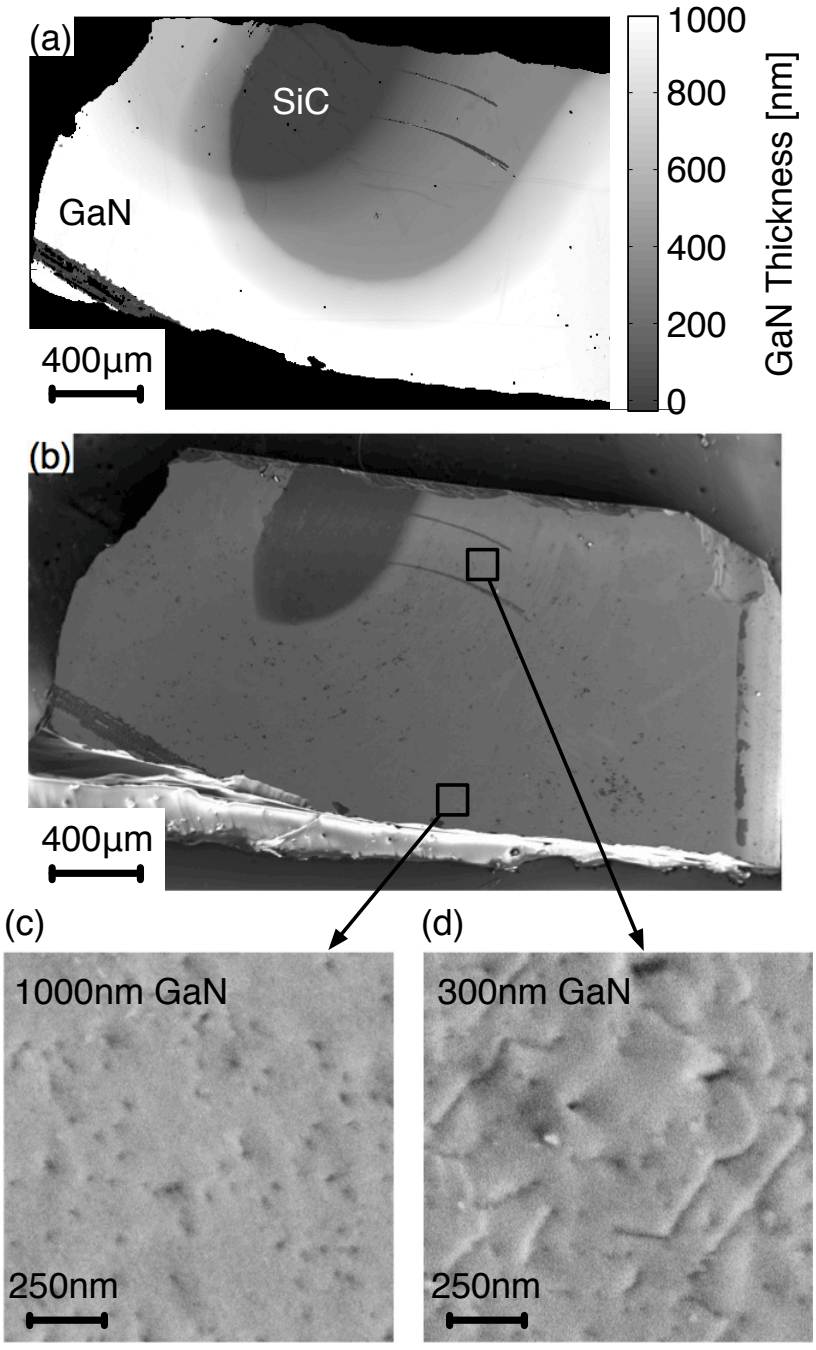

Figure 5·5: (a) Optical profilometer image showing the GaN film with thickness from 15-1000 nm. (b) SEM micrograph of the GaN sample grown on SiC. Magnified views of surface morphology for (c) 1000 nm and (d) 300 nm thick GaN.

are shown in Fig. 5·6(a) and Fig. 5·6(b), respectively.

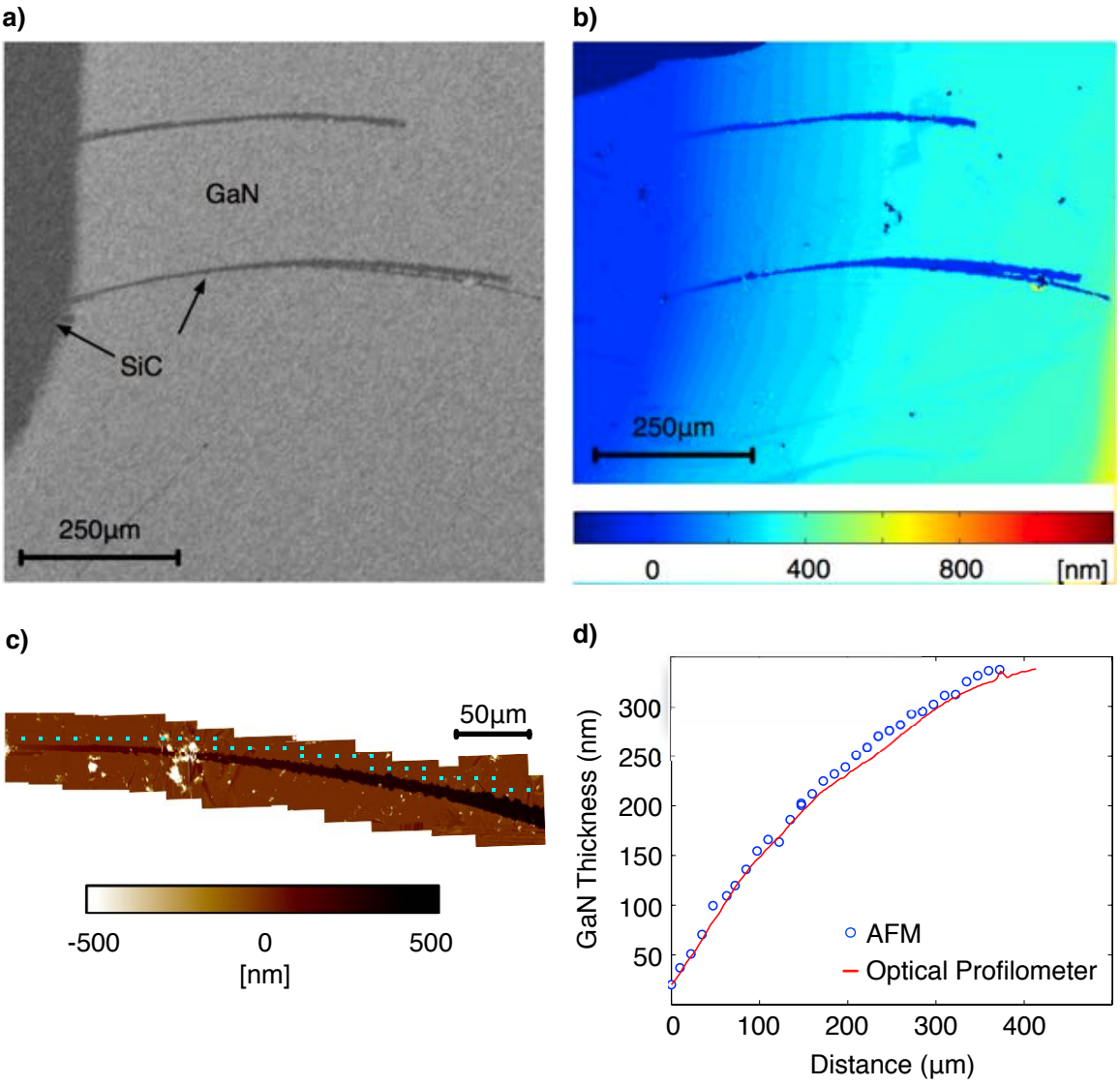

Figure 5·6: (a) SEM (b) optical profilometer, and (c) AFM images of the sample. (d) Thickness of the GaN film measured by AFM and optical profilometer images. The AFM data points are labeled in (c) as cyan squares.

Figure 5·6(a) and Fig. 5·6(b) are SEM and profilometer images of the two scratches. Figure 5·6(d) shows AFM and Zygo optical profilometer data compared using a line scan and discrete AFM measurements shown as cyan squares in Fig. 5·6(c).

This measurement was used to verify the accuracy of the optical height map.

SEM micrographs were used to determine the surface quality of the sample. The thinner GaN regions exhibited a higher defect concentration than the thicker regions. This is seen qualitatively in Fig. 5·5(c) and Fig. 5·5(d). In the thickness range between 340–430 nm we observe significant pitting on the sample surface shown in the SEM micrographs of Fig. 5·7(b). We believe these to be a result of dislocations annihilating in this thickness range, creating a large number of pits in the sample (Moustakas, 2013). For this reason, we exclude data points in this thickness region from our thermal analysis

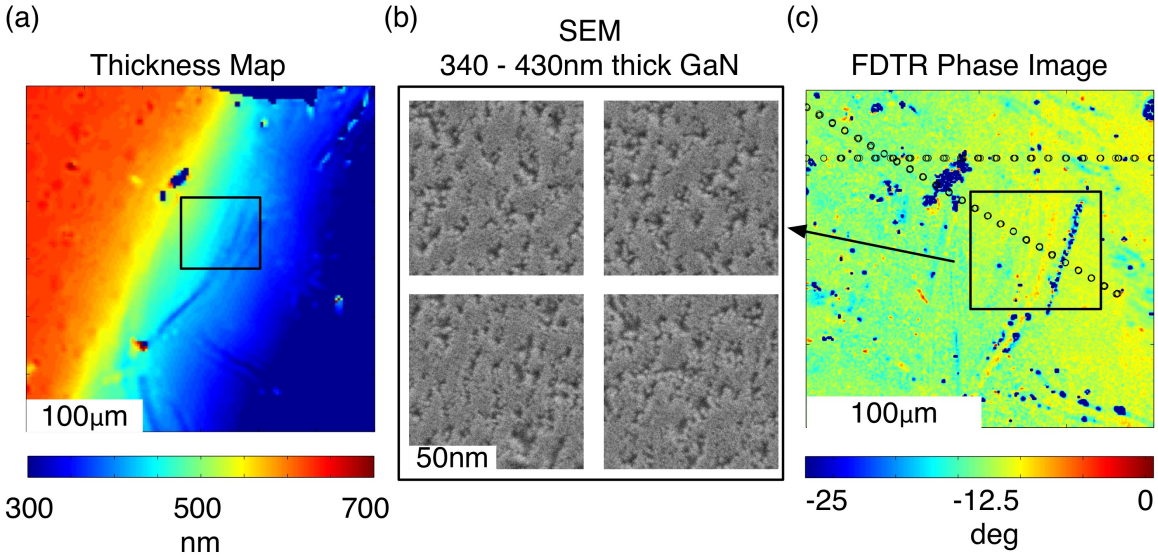

Figure 5·7: (a) Optical profilomter thickness map. The black box represents the investigated region. (b) SEM micrographs of GaN surface at four locations inside this region. (c) FDTR phase image at 5MHz. The black dots represent the locations of FDTR single point measurements. The black box highlights where the GaN film thickness is within the range of 340 - 430 nm.

Dislocation density was estimated using SEM images and X-Ray diffraction (XRD) measurements. For the SEM dislocation estimates, six high-magnification images were obtained with a total area of 12 μm^2. The total number of visible pits were

counted and divided by the total area (Su et al., 2012). We obtained a dislocation density of 5.2×10^{9} cm^{-2}. In addition, we estimate the screw and edge dislocation density with XRD measurements.

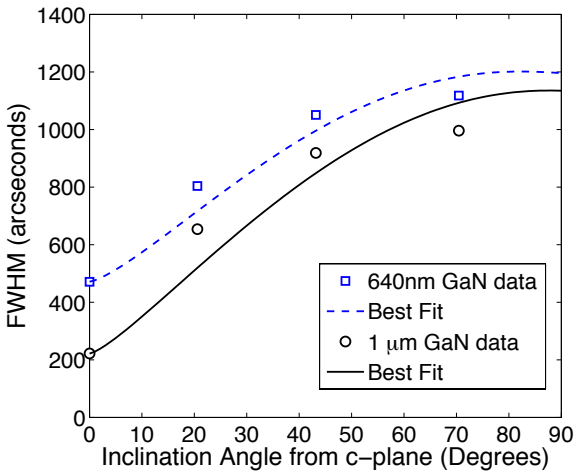

Figure 5·8: Rocking curve full-width at half-maximum of (0002), $(10\bar{2}5)$, $(10\bar{1}2)$, and $(30\bar{3}2)$ planes as a function of the planes inclination angle from the c-plane.

XRD rocking curves were obtained with a Bruker D8 Discover high-resolution X-ray diffraction system. Rocking curves associated with the (0002), $(10\bar{2}5)$, $(10\bar{1}2)$, and $(30\bar{3}2)$ planes were measured in the skew-symmetric geometry. Figure 5·8 shows each plane's rocking curve full-width at half-maximum versus the plane's inclination angle from the c-plane, and a fit to these data points based on the model described by Srikant, Speck and Clarke (Srikant et al., 1997). These data points indicate the out-of-plane mosaic angular spread is 221", and in-plane mosaic angular spread is 1135". Therefore, using the methods described by Metzger *et. al.* (Metzger et al., 1998), we estimate the GaN contains 9.9×10^{7} cm^{-2} screw dislocations, and 6.8×10^{9} cm^{-2} edge dislocations for the 1μm sample in this study. We also include the XRD curves for the 640 nm sample used in the previous study. We estimate the GaN contains 4.5×10^{8} cm^{-2} screw dislocations, and 7.6×10^{9} cm^{-2} edge dislocations for the 640 nm

sample of the previous study.

Cross-section SEM images of the sample are shown in Fig. 5·9. The coating seen on top of the GaN film in Fig. 5·9 is the Au/Ni transducer layer used for thermal measurements.

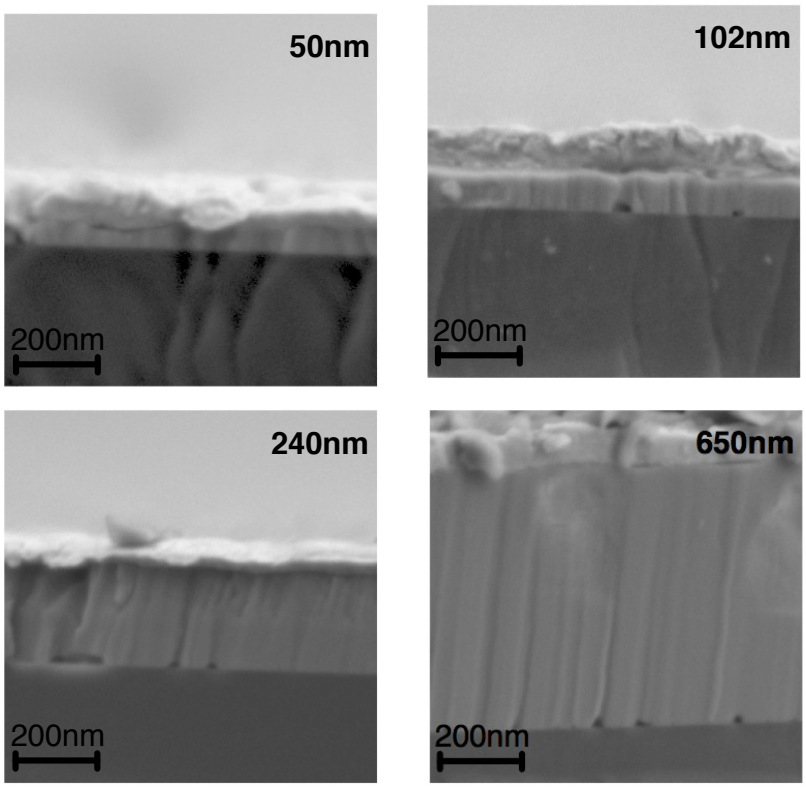

Figure 5·9: Cross section SEM images of GaN grown on 4H-SiC.

5.2.3 Results and Discussion

We used frequency domain thermoreflectance (FDTR) (Schmidt et al., 2009; Yang et al., 2013) to measure the thermal conductivity of the GaN sample as a function of thickness and temperature. Details about our setup can be found in Ref. (Yang et al., 2013). Briefly, a periodically modulated pump laser was focused to a Gaussian spot to locally heat the sample while an unmodulated probe laser beam measured the

surface temperature through a proportional change in the surface reflectivity. The $1/e^2$ radii of the pump and probe beams were 1.55 μm and 1.2 μm, respectively, at the sample surface. A 5 nm Ni adhesion layer and 85 nm Au transducer layer were deposited without breaking vacuum using electron beam deposition at a nominal chamber pressure of 1 μTorr. This Au/Ni transducer layer was deposited prior to FDTR measurements to absorb the pump beam and to reflect the probe beam. We varied the pump modulation frequency with a logarithmic spacing from 200 kHz to 30 MHz while a lock-in amplifier recorded the phase lag of the reflected probe beam at each frequency with respect to the pump beam.

Thermal properties were extracted by minimizing the error between the measured probe phase lag at each frequency and an analytical solution to the heat diffusion equation in a multilayer stack of materials (Schmidt et al., 2009). We modeled the GaN sample as three layers. Each layer was characterized by five physical parameters: the volumetric heat capacity (ρc_p), the cross-plane thermal conductivity ($\kappa_\perp$), the in-plane thermal conductivity ($\kappa_\parallel$), the layer thickness (d), and the conductance to the next layer (G). In addition, we account for volumetric heating of the 785 nm laser into the Au/Ni transducer layer based on its optical absorption depth (Yang et al., 2016a).

For this study, our measurement was mainly sensitive to transport in the cross-plane direction in the GaN film, although we assumed isotropic thermal conductivity of the GaN. We analyzed the experimental data using two types of fits: 1) a one-parameter fit of κ_{GaN} holding the TBC $G_{\mathrm{Au/Ni-GaN}}$ constant, and 2) a two-parameter fit of κ_{GaN} and $G_{\mathrm{Au/Ni-GaN}}$. All controlled properties in our thermal model were determined from separate measurements or obtained from literature. The following properties were obtained from literature and are summarized in Table 5.3: $(\rho c_p)_{\mathrm{GaN}}$ (Lee et al., 2011), $(\rho c_p)_{\mathrm{SiC}}$ (Hitova et al., 2000), and $(\kappa_\parallel/\kappa_\perp)_{\mathrm{SiC}}$ (Su et al., 2013a). How

we obtained the properties and uncertainties of the transducer layer, the thickness of the GaN layer, $G_{\mathrm{GaN-SiC}}$, and κ_{SiC} are explained in the following paragraphs.

Table 5.3: Parameters used to fit $\kappa_{\perp,\mathrm{GaN}}$.

	$1/e^2$ radii pump [μm]	$1/e^2$ radii probe [μm]	$\mathrm{G_{Au/Ni-GaN}}$ [MW/m^{2}K]	$\mathrm{G_{GaN-SiC}}$ [MW/m^{2}K]
	1.55 ± 0.05	1.2 ± 0.05	180 ± 60	225 ± 55
	ρc_p [MJ/m^{3}K]	$\kappa_\perp$ [W/mK]	$\kappa_\parallel/\kappa_\perp$	d [nm]
Au/Ni	2.3 ± 0.1	109 ± 5	1	89 ± 1.5
GaN	2.61 ± 0.1	$\kappa_{\perp,\mathrm{GaN}}$	1	$d_{\mathrm{GaN}} \pm \sigma$
SiC	2.13 ± 0.1	300 ± 15	1.16	-

5.2.4 FDTR measurement of the transducer layer

The properties of the Au/Ni film were determined from reference samples that were simultaneously coated with the investigated sample. The total thickness of the Au/Ni layer was measured to be 89 ± 1.5 nm by AFM on a reference glass slide. The values of $\kappa_{\mathrm{Au/Ni}}$ and $(\rho c_p)_{\mathrm{Au/Ni}}$ were determined by FDTR measurements of fused silica reference samples using literature values of thermal conductivity, $\kappa_{\mathrm{SiO_2}}$, and volumetric heat capacity, $(\rho c_p)_{\mathrm{SiO_2}}$ (Cahill, 1990), for SiO_2. The standard deviations for $(\rho c_p)_{\mathrm{Au/Ni}}$ and $\kappa_{\mathrm{Au/Ni}}$ were obtained from fifteen measurements at different locations on the reference sample.

We consider the thickness of the transducer layer to be relatively thick enough to neglect weak electron-phonon coupling and ballistic effects. The deposited Au/Ni layer was 89nm thick with a thermal conductivity of 109 W/mK. We estimate the thermalization length of electrons in the transducer to be approximately 67 nm using:

$$L_e = \sqrt{\frac{k_e \cdot \tau_{\mathrm{e,ph}}}{C_e}} \tag{5.5}$$

Where k_e is the thermal conductivity of the gold transducer, $\tau_{\mathrm{e,ph}}$ is the electron-phonon relaxation time taken to 840 fs (Groeneveld et al., 1995), and C_e is the electronic heat capacity and taken to be 20.3 kJ/m^{3}K (Kittel, 2004). If we include the optical absorption depth of Au at our pump wavelength of 785 nm, which we take to be 12.8 nm (Palik, 1985), we estimate 87% of the electrons have thermalized in our transducer layer prior to reaching the interface and therefore we have minimum effects from heating at the interface between the transducer layer and the GaN and ballistic transport.

5.2.5 Thickness measurements

The thickness of the GaN layer for each measurement point, d_{GaN}, was determined with FDTR images overlayed onto optical profilometer images. FDTR images of 200 μm by 200 μm were created by modulating the pump beam at 1MHz and raster scanning the sample with a piezo-stage. A lock-in amplifier recorded the amplitude and phase response of the reflected probe beam at each pixel. Subsequent FDTR measurements at each pixel were then assigned a coordinate in the FDTR image that could be mapped to the profilometer image.

Figure 5·10 plots the overlap of nine FDTR images onto the optical profilometer image used to determine the thickness of each FDTR measurement. The FDTR images have an arbitrary unit and the image contrast is only used to overlap features to the optical image. An expanded view of FDTR image 6 is shown in Fig. 5·7(c). Black circles mark where FDTR measurements were taken with a sweep of 40 frequencies. Multiple FDTR single-pixel measurements consisting of a sweep of 40 frequencies were taken on each image with over 1,000 of them taken across the nine images.

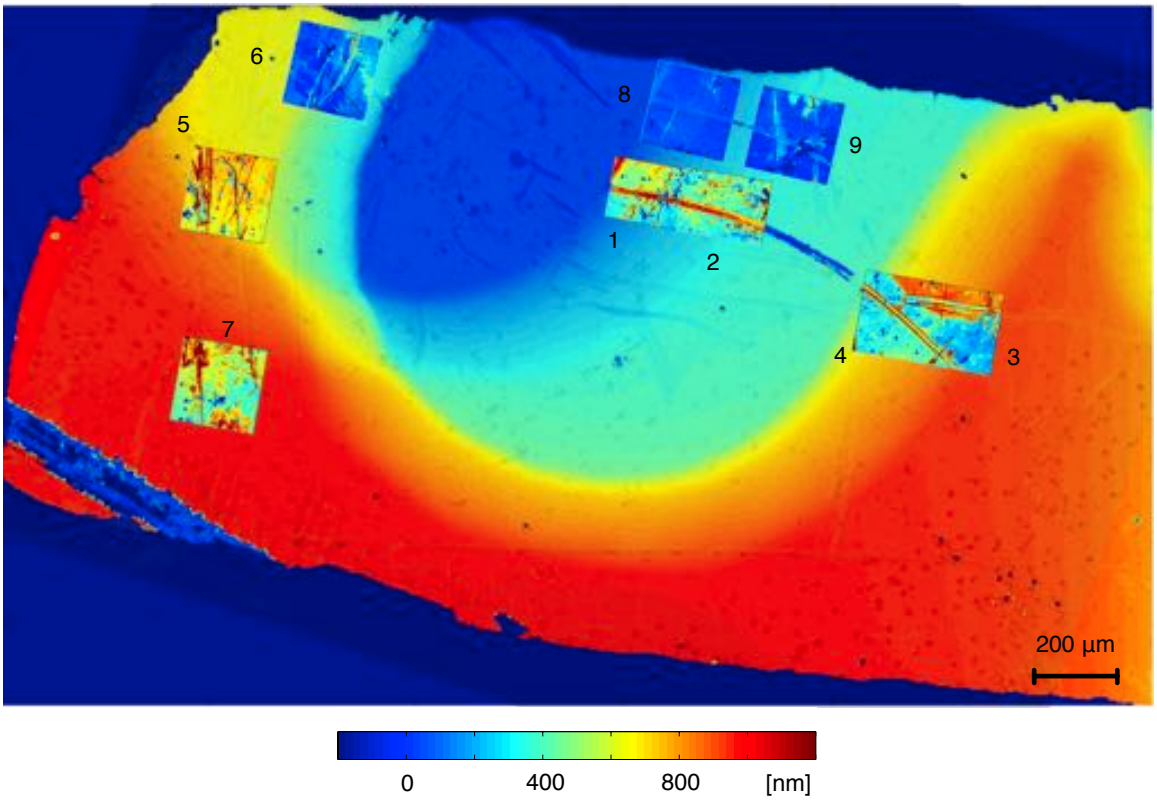

Figure 5·10: An overlap of nine FDTR images onto an optical profilometer image super imposed on an optical image used to determine the thickness of each FDTR measurement.

The overlap of FDTR, optical, and optical profilometer images allowed us to accurately map thickness to FDTR single-pixel measurements. Our FDTR images had spatial resolution of 1 μm while the optical profilometer image had spatial resolution of 1.5 μm. We obtained d_{GaN} by averaging the heights of the profilometer micrographs within a 5 μm box around each FDTR single-pixel coordinate. The standard deviation, σ, of the average was taken as the uncertainty in d_{GaN}.

5.2.6 FDTR measurement of $G_{GaN-SiC}$ and κ_{SiC}

To determine $G_{GaN-SiC}$ and κ_{SiC}, a four-parameter fit of $G_{Au/Ni-GaN}$, $G_{GaN-SiC}$, κ_{SiC}, and κ_{GaN} was performed at two locations on the sample surface for thickness ranging

between 800-1000 nm. The average and standard deviation of 50 measurements at each location was taken to obtain $G_{\mathrm{GaN-SiC}}$ and κ_{SiC} and their respective uncertainties. Additionally, we measured the 1 μm-thick region from $300 < T < 600$ K fitting the same four parameters. The measured room temperature values are reported in Table 5.3 and the temperature dependent thermal conductivity of the 1 μm-thick region is shown in Fig. 5·11.

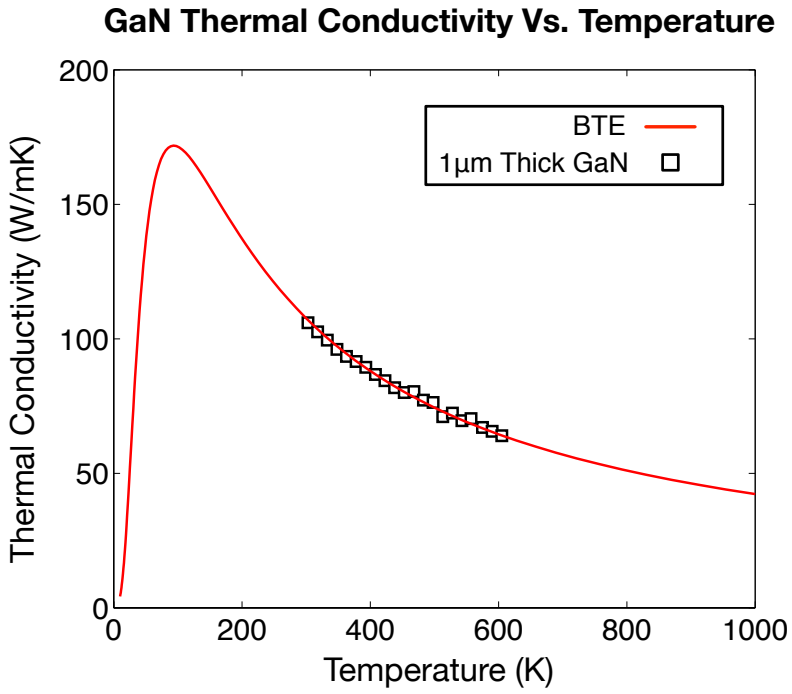

Figure 5·11: (a) Thermal conductivity of 1 μm-thick GaN. The solid line represent are the solution to Eq. 5.6 while fitting only impurity scattering in the form of $\tau_I = A\omega^4$

5.2.7 FDTR results for thickness dependent measurements

Finally, with all controlled model parameters and their uncertainties known, we performed two types of fits to determine the thermal conductivity of GaN for all the data points from 15-1000 nm: 1) A one-parameter fit of κ_{GaN} while holding $G_{\mathrm{Au/Ni-GaN}}$ constant at 180 MW/m^{2}K; and 2) a two-parameter fit of κ_{GaN} and $G_{\mathrm{Au/Ni-GaN}}$.

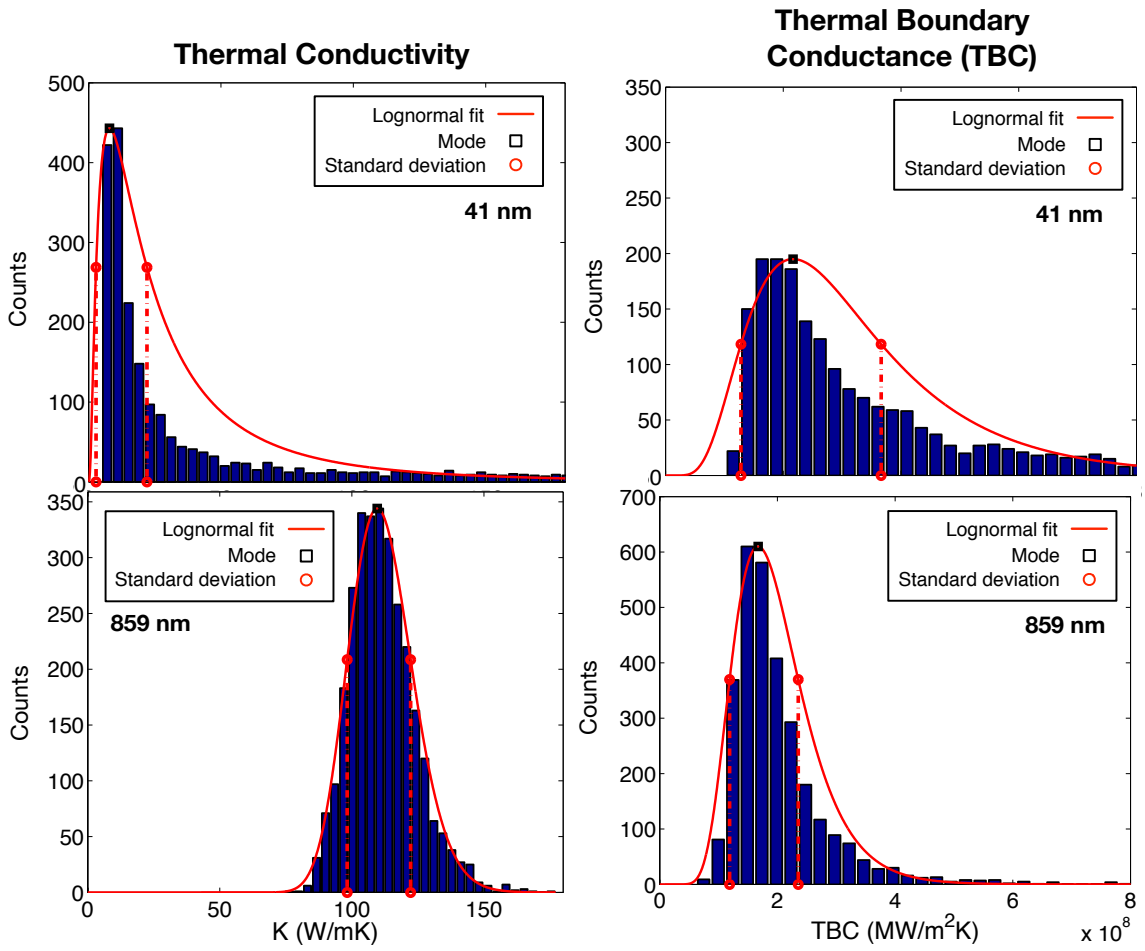

Figure 5·12: Monte Carlo results fitted with a lognormal distribution. The fitted parameters of κ_{GaN} (left) and $G_{\mathrm{Au/Ni-GaN}}$ (right) are shown for data points at a thickness of 41 nm and 859 nm.

The uniqueness of the fitted parameters was determined with Monte Carlo simulations (Yang et al., 2016b). Each controlled parameter in the thermal model was assumed to have a normal distribution about a mean value with a standard deviation, provided in Table 5.3. In each iteration of the Monte Carlo simulation, the program randomly generated values for the known parameters based on their distributions and performed a nonlinear least squares fit of the thermal model to the measured data. Each data point was fit 500 times. The data was then binned into 15 nm intervals

across the thickness range and a lognormal distribution was fit to the data. We report the mode of the distribution as the measured value and the uncertainty as one standard deviation from the mode. Figure 5·12 shows sample Monte Carlo results from thick (859 nm) and thin (41 nm) regions of the GaN film.

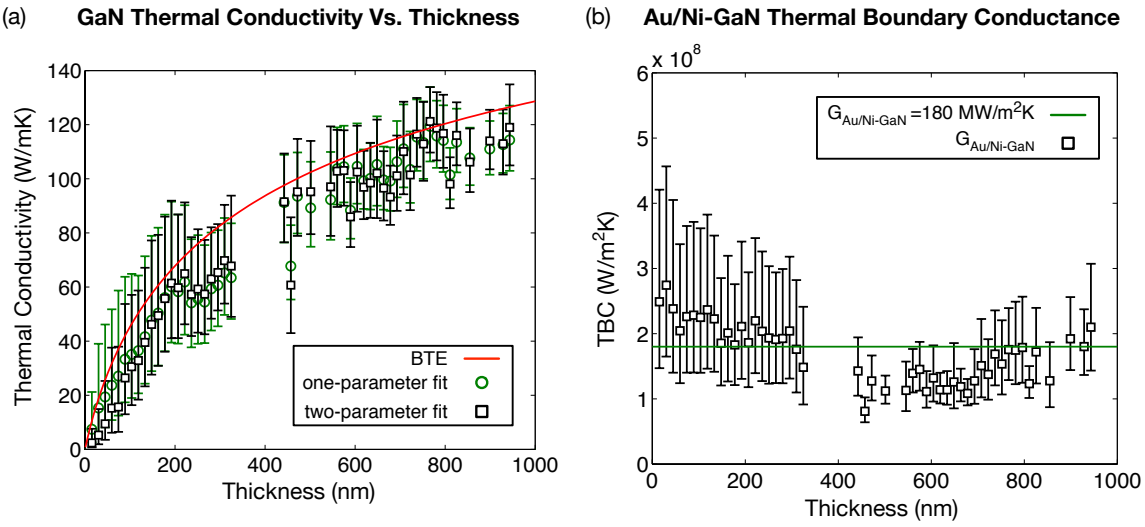

Figure 5·13: (a) Thickness dependent thermal conductivity of GaN for a one-parameter fit of κ_{GaN} (green circles) where $G_{\mathrm{Au/Ni-GaN}} = 180$ MW/m^{2}K and κ_{GaN} from the 2-parameter fit of both κ_{GaN} (black squares) and $G_{\mathrm{Au/Ni-GaN}}$. The solid line is the solution to Eq. 1 as a function of thickness. (b) Fitted $G_{\mathrm{Au/Ni-GaN}}$ (black squares) and $G_{\mathrm{Au/Ni-GaN}} = 180$ MW/m^{2}K.

The results of both the one- and two-parameter fits are plotted in Fig. 5·13(a) and Fig. 5·13(b). We see that both fits give similar values and uncertainties for thermal conductivity for thickness above 150 nm. Below this thickness the two-parameter fitted values for thermal conductivity decreased compared to the one-parameter fit, while the value for thermal boundary conductance of Au/Ni-GaN increases above the fixed value of 180 MW/m^{2}K that was used in the one-parameter fit. This increase in $G_{\mathrm{Au/Ni-GaN}}$ and corresponding decrease in κ_{GaN} is possibly due to ballistic transport across the GaN film as observed by Willson *et al.* (Wilson and Cahill, 2014).

We used a model based on the Boltzmann Transport Equation (BTE) to explain the trend of thermal conductivity versus thickness. We used a variant of the BTE described by Beechem *et al.* (Beechem et al., 2016), which uses the a polynomial fit to the true phonon dispersion curve of wurtzite GaN in the Γ-A direction (Davydov et al., 1998) and the relaxation time approximation in conjunction with Matthiessen's rule, which implies that the phonon-scattering mechanisms are independent from one another and add for each phonon branch j, as $\tau_j^{-1} = \sum_i \tau_i^{-1}$, where τ_i is the relaxation time per scattering type i. The scattering types accounted for in our model are: phonon-phonon Umklapp scattering (τ_U), phonon-impurity scattering (τ_I), phonon-boundary scattering (τ_B), and phonon-dislocation scattering (τ_D). The thermal conductivity, κ_{GaN} is then calculated as:

$$\kappa_{GaN} = \frac{1}{6\pi^2} \sum_j \int_0^{q_{m,j}} \frac{\hbar^2 \omega_j^2}{k_B T^2} v_j^2 \tau_j f(x) q^2 dq \tag{5.6}$$

where the summation is over all phonon branches, v_j is the phonon velocity per phonon branch j, q is the wave vector, ω is the phonon frequency, $x = \frac{\hbar\omega_j}{k_B T}$ is a dimensional phonon frequency, $f(x) = \frac{e^x}{(e^x-1)^2}$, k_B is the Boltzmann constant, T is the temperature, $\hbar$ is the modified Planck's constant, and τ_j is the relaxation time calculated through Matthiessen's rule.

For this study, we obtained the Umklapp scattering constants by fitting the BTE model to the bulk GaN measurements reported by Morelli *et al.* (Morelli et al., 2002). Specifically, we obtained $P = 6.5 \times 10^{-20}$ s/K and $C_u = 86$ K in the Umklapp relaxation term: $\tau_U^{-1} = P\omega^2 T \exp(-C_u/T)$. Maintaining constant Umklapp scattering parameters, we then performed a one-parameter fit of the impurity scattering constant, A, in the impurity relaxation term $\tau_I^{-1}(\omega) = A\omega^4$ using temperature dependent thermal conductivity measurements of 1μm-thick GaN as shown in Fig. 5·11. Finally, we solved Eq. 5.6 to predict thermal conductivity as a function of thickness, varying

the thickness d in the boundary scattering term $\tau_{B,j}^{-1}(\omega) = \frac{v_j}{2.38d}$. We plot the result in Fig. 5·13(a) and find that this model is in good agreement with our data.

Dislocation density in the form of screw, edge, and mixed defects should be a dominant phonon-scattering mechanism in GaN films (Mion et al., 2006; Cho et al., 2014; Kotchetkov et al., 2001). We accounted for dislocation density in our BTE model as suggested by Zou *et al.* (Zou et al., 2002). Specifically, our phonon-dislocation relaxation time constant was computed as $\tau_D^{-1} = \tau_{DC}^{-1} + \tau_S^{-1} + \tau_E^{-1} + \tau_M^{-1}$, where τ_{DC}^{-1} accounts for phonon scattering on the core of dislocations and τ_S^{-1}, τ_E^{-1}, and τ_M^{-1} account for phonon scattering on the elastic field of screw, edge, and mixed dislocations, respectively. It has been shown that dislocation density should increase exponentially with a decreasing film thickness (Mion et al., 2006). However, for our BTE model, we fixed the dislocation densities as the values measured in our 1 μm-thick GaN film and noticed no large deviation in our model from the data as a function of thickness due to this assumption. This suggests that phonon-boundary scattering dominates at this dislocation density and in this thickness range.

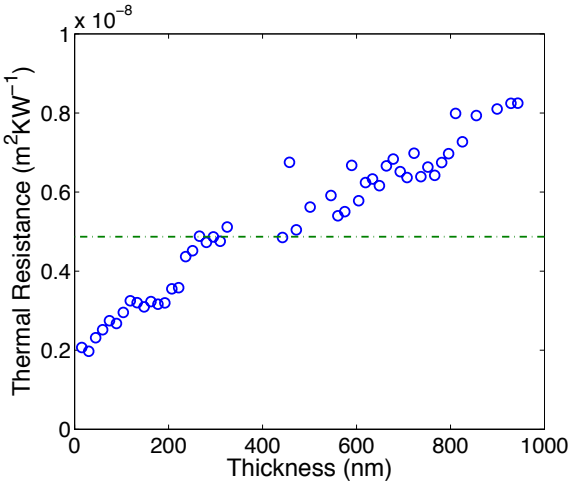

Figure 5·14: a plot of thermal resistance as a function of GaN thickness. The green dotted line is a guide to the eye.

Finally, we plot the total resistance of the GaN film as a function of thickness in

Fig. 5·14. This is done by dividing the thickness by the thermal conductivity such that $R = l/\kappa$. By doing this we can determine if there is an optimum thickness to grow the GaN film. We see that the thermal resistance does not significantly change between 300-500 nm. This suggests that the optimum GaN buffer layer thickness might be in this range. However, this could also be a result of insufficient data points in the 340-430 nm thickness range and other effects might be seen due to the GaN islands being not fully coalesced.

5.2.8 Summary

In conclusion, we used FDTR to study thermal transport in a GaN film grown on SiC in the thickness range of 15-1000 nm. Using Monte Carlo simulations, we compared the results of a one-parameter fit of κ_{GaN} with $G_{\mathrm{Au/Ni-GaN}}$ held constant and a two-parameter fit of κ_{GaN} and $G_{\mathrm{Au/Ni-GaN}}$, and found evidence of ballistic transport across the film at thicknesses below 150 nm. The dependence of thermal conductivity on film thickness is in good agreement with a BTE model based on the relaxation time approximation. These results may be useful for engineering future generations of wide-bandgap semiconductor devices. The work presented in this chapter has been published in Applied Physics Letters (Ziade et al., 2017).

Chapter 6

Anisotropic Thermal Conductivity of Polycrystalline Diamond Films

6.1 Introduction

As discussed in the previous chapter, nitride material systems are promising wide-bandgap semiconductors for next-generation RF electronics due to their high breakdown voltages and carrier densities. However, performance of these devices at high frequencies is limited by heat removal from the active region (Meneghesso et al., 2008; Won et al., 2013; Chou et al., 2004; Bloschock and Bar-Cohen, 2012). Silicon carbide (SiC) has been used as the substrate in a majority of today's high power GaN-based devices because of its closely-matched lattice spacing to GaN and its high thermal conductivity (κ = 330 W/mK) (Kukushkin et al., 2008). However, A more worthwhile effort would focus on putting GaN devices on diamond substrates, which have a thermal conductivity approaching 2000 W/mK (Graebner et al., 1992; Fournier and Plamann, 1995) and 5000 W/mK if enriched (Ward et al., 2009). The challenge with GaN-on-diamond is the large lattice mismatch between these two crystals, which unfortunately requires a transition layer that introduces defects and additional thermal resistance at the interface. However, simulations predict that GaN-on-diamond devices with a TBC above 30 MW/m^{2}K will have a lower temperature rise than GaN-on-SiC devices with infinite TBC (Cho et al., 2013; Cho et al., 2014) making this a promising direction for wide-bandgap device design (Francis et al., 2010). Addition-

ally, high quality polycrystalline diamond has become readily available because of recent advances in the synthesis of high quality films (Graebner et al., 1992; Fournier and Plamann, 1995).

In order to take advantage of the high thermal conductivity diamond film growth must be integrated into high power device structures. Growth conditions and nucleation layers impact the thermal conductivity of the diamond film. In this chapter, nano-crystalline diamond was grown on silicon in the thickness range of 1.3 μm to 10 μm. The diamond was grown at a temperature T and a temperature $T + \Delta T$ where ΔT was on the order of 70K to study the effect of growth temperature on thermal conductivity. We measured the anisotropic thermal conductivity of these thin film diamond films and the thermal boundary conductance from these diamond films to the substrate as a function of growth temperature and thickness.

6.2 Sample preperation

Five diamond samples were obtained from Element6. The diamond films were grown via chemical vapor deposition on the $< 111 >$ plane of a silicon substrates. Once received, the samples were cleaned for 30 minutes using a Piranha solution, 4:1 (H_2SO_4):(30% H_2O_2), to remove organic residue. The samples were then plasma treated in an M4L RF plasma asher with an oxygen flow rate of 300 sccm and a plasma power of 500W for 5 minutes. This step was taken to modify the surface of the film from hydrogen to oxygen terminated carbon. Such a procedure is expected to improve the thermal boundary conductance between our metal transducer and the diamond substrate (Monachon and Weber, 2013) improving the sensitivity of a thermal measurement to the thermal conductivity of diamond. Finally, we delaminated two diamond films from the silicon substrate using UV adhesive tape. A schematic of the two types of films we measured is shown in Fig. 6·1.

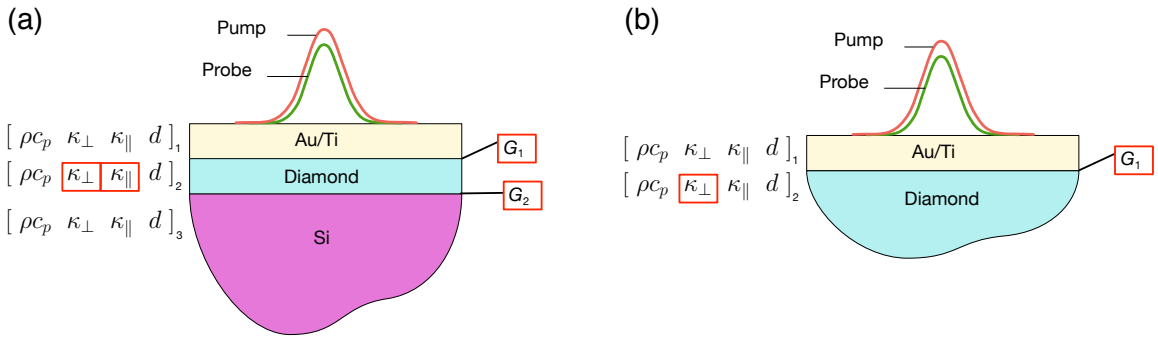

Figure 6·1: Sample schematic of (a) CVD diamond grown on silicon substrate (b) delaminated diamond film. The Au/Ti layer is deposited for the thermal measurements. The properties of interest are highlighted with red boxes.

6.3 AFM and SEM

The thickness, surface quality, and grain size of the diamond films were determined by SEM and AFM images. Cross-sectional SEM images were used to determine the thickness of the diamond films as shown in Fig. 6·2(a). SEM images were also used to determine the film quality at the surface as shown in Fig. 6·2(b). AFM images such as the ones shown in Fig. 6·2(c) were used to determine the roughness. Lastly, phase images from AFM tapping mode measurements of the surface of the delaminated film shown in Fig. 6·2(d) were used to determine the grain-size of the the diamond films at interface between the diamond and the Si substrate. Qualitatively, we see that the grain-size is slightly larger for the diamond grown at higher temperature.

6.4 Thermal Characterization

We used frequency domain thermoreflectance (FDTR) (Schmidt et al., 2009; Yang et al., 2013) to measure the thermal conductivity of the diamond sample as a function of thickness. A periodically modulated pump laser was focused to a Gaussian spot to locally heat the sample while an unmodulated probe laser beam measured the surface temperature through a proportional change in the surface reflectivity. The

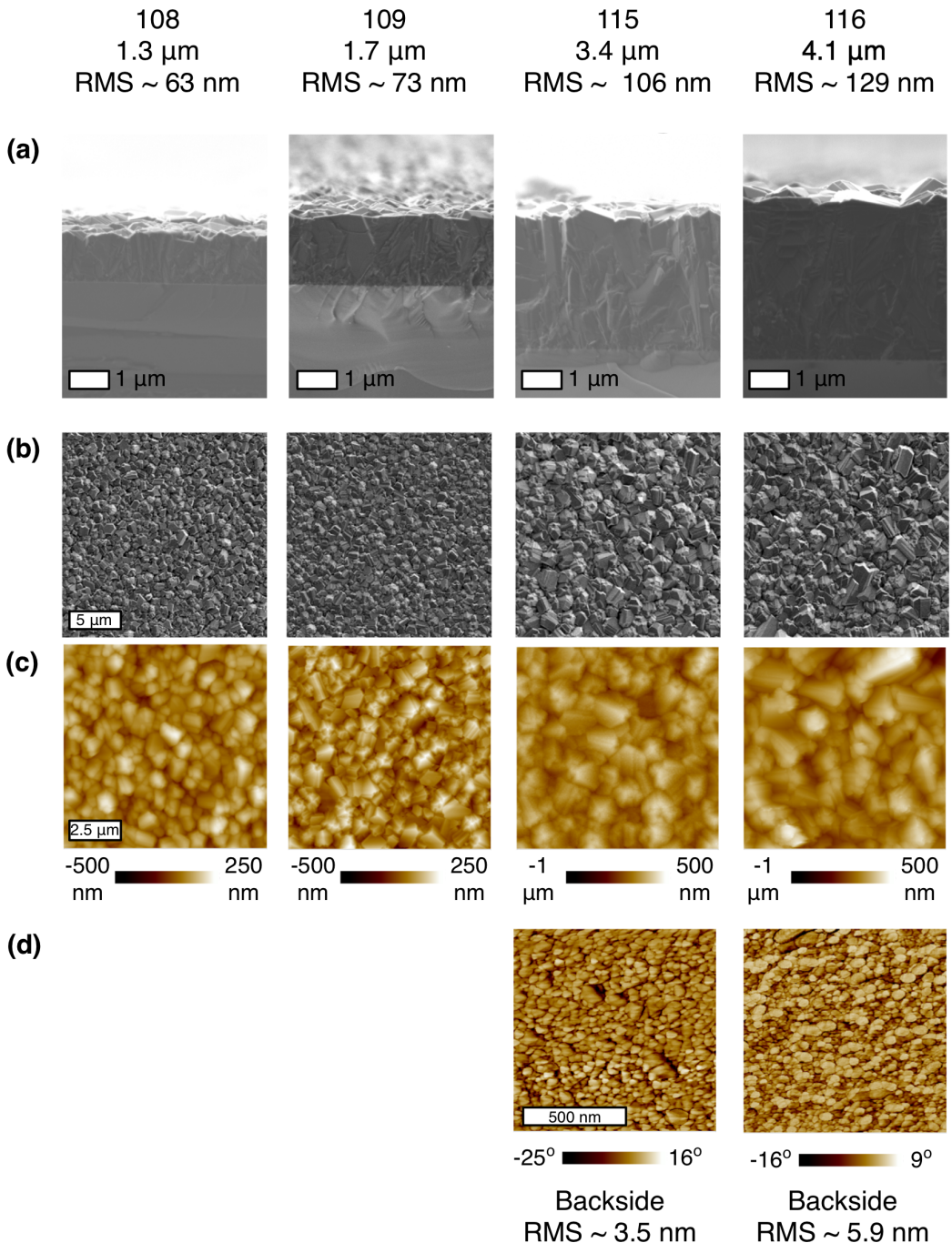

Figure 6·2: (a) SEM cross-section micrographs of the diamond films (b) SEM micrographs of sample surface. The images are 20 by 20 μm^2 in size. (c) AFM micrographs images of the diamond surface. The images are 10 by 10 μm^2 in size. (d) Phase maps from tapping mode AFM scans showing the grain-size of the diamond as they nucleated on the silicon surface. The images are 1 by 1 μm^2 in size.

$1/e^2$ radii of the pump and probe beams were 1.55 μm and 1.2 μm, respectively, at the sample surface. A 5 nm Ti adhesion layer and 95 nm Au transducer layer were deposited without breaking vacuum using electron beam deposition at a nominal chamber pressure of 1 μTorr. This Au/Ti transducer layer was deposited prior to FDTR measurements to absorb the pump beam and to reflect the probe beam. We varied the pump modulation frequency with a logarithmic spacing from 10 kHz to 50 MHz while a lock-in amplifier recorded the phase lag of the reflected probe beam at each frequency with respect to the pump beam.

Thermal properties were extracted by minimizing the error between the measured probe phase lag at each frequency and an analytical solution to the heat diffusion equation in a multilayer stack of materials (Schmidt et al., 2009). We modeled the diamond sample with the silicon substrates as three layers, Fig. 6·1(a), and the free-standing diamond sample as two layers Fig. 6·1(b). Each layer was characterized by five physical parameters: the volumetric heat capacity (ρc_p), the cross-plane thermal conductivity ($\kappa_\perp$), the in-plane thermal conductivity ($\kappa_\parallel$), the layer thickness (d), and the conductance to the next layer (G).

6.4.1 Sensitivity analysis and affect of thermal penetration depth

It is difficult to isolate the thermal conductivity of diamond when the thermal boundary conductance of the metal transducer is low. This is because of diamonds high thermal conductivity. We use phase sensitivity to estimate how sensitive the phase signal is to multiple properties in the thermal model. We calculate phase sensitivity, $S(\omega)$, to a parameter x as a function of frequency based on:

$$S(\omega) = \frac{\partial \phi(\omega)}{\partial \ln x} \tag{6.1}$$

The sensitivity plots for 20% change in parameter x for the four parameters of

interest are shown in Fig. 6·3. The values used in this sensitivity are given in Table 6.1. The noise floor of our measurement apparatus is about 0.2 deg.

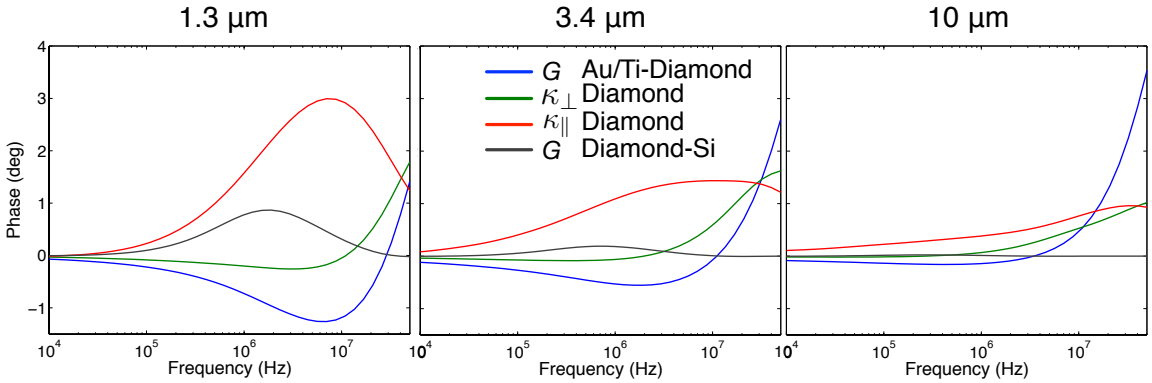

Figure 6·3: Sensitivity analysis of a diamond film with three thicknesses 1.3μm, 3.4μm , and 10μm. The values assumed for this analyis can be found in Table. 6.1

Table 6.1: Parameters used to calculate the sensitivity curves in Fig. 6·3. The pump and probe $1/e^2$ radii were 1.55 $\pm$ 0.05 μm and 1.2 $\pm$ 0.05 μm respectively.

	ρc_p [MJ/m^{3}K]	$\kappa_\perp$ [W/mK]	$\kappa_\parallel$ [W/mK]	d [nm]	G [MW/m^{2}K]
Au/Ti	2.48 $\pm$ 0.1	174 $\pm$ 10	174 $\pm$ 10	100 $\pm$ 2	300
Diamond	1.816 $\pm$ 0.1	250	250	1.3 μm	25
		500	500	3.4 μm	
		1000	1000	10 μm	
Si	1.65 $\pm$ 0.1	143.5	143.5	-	

We notice a couple trends from Fig. 6·3 that help determine what parameters to fit. First, the sensitivity to $G_{\mathrm{Diamond-Si}}$ is almost zero for the films that are 3.4 μm and thicker. Second, our measurement is most sensitive to $\kappa_\parallel$ and $G_{\mathrm{Au/Ti-Diamond}}$. Lastly, the sensitivity to $\kappa_\perp$ is the most at frequencies greater than 1 MHz, which overlaps with the peak sensitivity of $G_{\mathrm{Au/Ti-Diamond}}$. Therefore, it may be difficult to separate $G_{\mathrm{Au/Ti-Diamond}}$ and $\kappa_\perp$.

We also investigated the effects of the thermal wave penetration depth at low and high pump-modulation frequencies. We do this to identify what frequency range

should be used to for our thermal wave to remain within the dimensions of the diamond film. A first order approximate to thermal penetration depth is given by (Koh and Cahill, 2007):

$$\delta_{\text{Thermal}} = \sqrt{\frac{\kappa}{\pi \rho c_p f}} \tag{6.2}$$

where f is the pump-modulation frequency. We again look at the case of a film with three different values for thermal conductivity: 250, 500, and 1000 [W/mK] as was done in our sensitivity plots. The value for δ_{Thermal} as a function of frequency is plotted in Fig. 6·4.

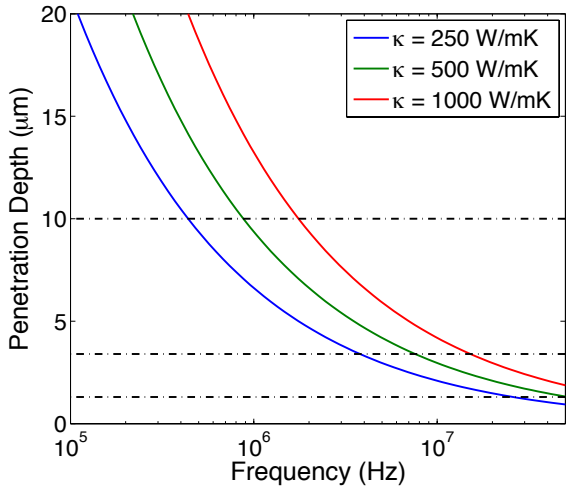

Figure 6·4: Thermal penetration depth as a function of thickness and isotropic thermal conductivity, κ. The dashed horizontal lines are plotted for thicknesses of 1.3 μm, 3.4 μm, and 10 μm.

The results of Fig. 6·4 suggest what frequency range we should use to ensure that thermal wave remains within the diamond film. For the diamond film with thickness 1.3 μm it appears that we should use frequency ranges above 30 MHz, for the 3.4 μm thick film a frequency range above 400 KHz, and for the 10 μm thick film a frequency range above 200 KHz.

6.4.2 Results

For this study, our measurement was mainly sensitive to transport for in-plane thermal conductivity of the diamond film. However, by fitting over different frequency ranges we are able to extract both in-plane and cross-plane thermal conductivity of the diamond film. We analyzed the experimental data using three types of fits: 1)

a four-parameter fit of $\kappa_{\parallel}$, $\kappa_{\perp}$, $G_{\mathrm{Au/Ti-Diamond}}$, and $G_{\mathrm{Diamond-Si}}$, 2) three-parameter fit of $\kappa_{\parallel}$, $\kappa_{\perp}$, and $G_{\mathrm{Au/Ti-Diamond}}$, and finally 3) a two-parameter fit of $\kappa_{\mathrm{Diamond}}$ and $G_{\mathrm{Au/Ti-Diamond}}$ where the thermal conductivity of the diamond is assumed to be isotropic. All controlled properties in our thermal model were determined from separate measurements or obtained from literature.

The properties of the Au/Ti film were determined from reference samples that were simultaneously coated with the investigated sample. The total thickness of the Au/Ti layer was measured to be 100 ± 2 nm by AFM on a reference glass slide. The values of $\kappa_{\mathrm{Au/Ti}}$ and $(\rho c_p)_{\mathrm{Au/Ti}}$ were determined by FDTR measurements of fused silica reference samples using literature values of thermal conductivity, $\kappa_{\mathrm{SiO_2}}$, and volumetric heat capacity, $(\rho c_p)_{\mathrm{SiO_2}}$ (Cahill, 1990), for SiO_2. The standard deviations for $(\rho c_p)_{\mathrm{Au/Ti}}$ and $\kappa_{\mathrm{Au/Ti}}$ were obtained from fifteen measurements at different locations on the reference sample. The results are given in Table 6.1.

We consider the thickness of the transducer layer to be relatively thick to neglect weak electron-phonon coupling and ballistic effects. The deposited Au/Ti layer was 100 nm thick with a thermal conductivity of 174 W/mK. We estimate the thermalization length of electrons in the transducer to be approximately 85 nm using:

$$L_e = \sqrt{\frac{k_e \cdot \tau_{\mathrm{e,ph}}}{C_e}} \tag{6.3}$$

Where k_e is the thermal conductivity of the gold transducer, $\tau_{\mathrm{e,ph}}$ is the electron-phonon relaxation time taken to 840 fs (Groeneveld et al., 1995), and C_e is the electronic heat capacity and taken to be 20.3 kJ/m^{3}K (Kittel, 2004). If we include the optical absorption depth of Au at our pump wavelength of 785 nm, which we take to be 12.8 nm (Palik, 1985), we estimate 84% of the electrons have thermalized in our transducer layer prior to reaching the interface and therefore we have minimum effects from heating at the interface between the transducer layer and the diamond and ballistic transport.

A four-parameter fit of $\kappa_{\parallel}$, $\kappa_{\perp}$, $G_{\mathrm{Au/Ti-Diamond}}$, and $G_{\mathrm{Diamond-Si}}$ was performed at multiple locations on the diamond samples surface with thickness ranging between 1.3 μm and 4.3 μm. The average and standard deviation of over 10 measurements at each location is taken to obtain $\kappa_{\parallel}$, $\kappa_{\perp}$, $G_{\mathrm{Au/Ti-Diamond}}$, and $G_{\mathrm{Diamond-Si}}$ and their respective uncertainties. A three-parameter fit of $\kappa_{\parallel}$, $\kappa_{\perp}$, and $G_{\mathrm{Au/Ti-Diamond}}$ was performed on the diamond film with thickness of 10 μm. The same procedure as just described was used to obtain the average and standard deviation of these values. The

results of this analysis are shown in Table 6.2. Finally, a two-parameter fit of κ_{Diamond} and $G_{\text{Au/Ti−Diamond}}$ where the thermal conductivity of the diamond was assumed to be isotropic was performed on the delaminated samples with thickness of 3.4 μm and 4.1 μm. The results of this analysis are shown in Table 6.3. A summary of all the results are plotted in Fig. 6·5.

Table 6.2: Measurements of diamond from top. T1 (low T). T2 (high T). Samples 108, 109, 115, and 116 results from a three parameter fit where G_{Di-Si} is fixed to 25e6 MW/m^{2}K.

Wafer ID	Measured Thickness [μm]	G1 [MW/m^{2}K]	k$_{cross}$ [W/mK]	k$_{in}$ [W/mK]	Fitting Frequency [Hz]
108 (T1)	1.3	304 ± 150	235 ± 69	223 ± 169	3e7 to 6.2e7
109 (T2)	1.7	265 ± 61	379 ± 148	300 ± 86	1e7 to 6.2e7
115 (T1)	3.4	218 ± 40	1121 ± 419	351 ± 136	1e6 to 6.2e7
116 (T2)	4.1	208 ± 33	1026 ± 418	285 ± 162	1e6 to 6.2e7
120	10	228 ± 43	1613 ± 370	446 ± 143	1e6 to 6.2e7

Table 6.3: Backside measurements. T1 (low T). T2 (high T).

Wafer ID	Measured Thickness [μm]	G1 [MW/m^{2}K]	k$_{cross}$ [W/mK]	k$_{in}$/k$_{cross}$
115 (T1)	3.4	49.5 ± 1.1	552 ± 35.4	1
116 (T2)	4.1	83 ± 5.7	697.7 ± 53.0	1

6.5 Discussion

The final results for thermal conductivity of the diamond film are plotted in Fig. 6·5(a) and for thermal boundary conductance from the Au/Ti film to the diamond and the thermal boundary conductance of the diamond film to the silicon substrate in 6·5(b). We also plot the results from Ref. (Sood et al., 2016) in Fig. 6·5(a).

The cross-plane thermal conductivity of the diamond film increases with thickness. The film does not reach bulk value even at 10 μm. This trend of increasing thermal conductivity with film thickness is expected as the crystal size of the diamond should increase with thickness, therefore, the phonons will travel further before scattering on the grain boundaries (Goodson, 1996). First principles calculations using the full

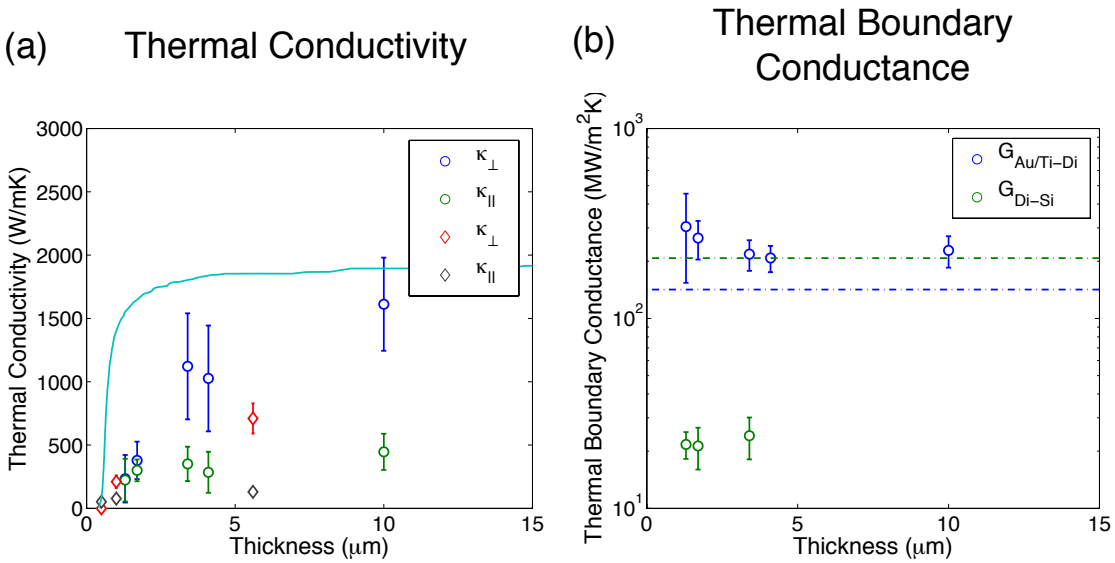

Figure 6·5: (a) Anisotropic thermal conductivity of mircon-thick diamond films. The diamonds are taken from Ref. (Sood et al., 2016). Cyan line is the thermal conductivity accumulation function of diamond as a function of mean free path calculated from first principles in Ref. (Li et al., 2012). (b) Thermal boundary conductance G. The dotted lines are DMM calculations using the correction factor. The green dashed line corresponds to $G_{\mathrm{DMM-Di-Si}}$ while the blue dashed line corresponds to $G_{\mathrm{DMM-Ti-Di}}$.

solution to the BTE suggested that approximately 80% of phonons have a mean free path less than 1.5 μm (Li et al., 2012). The thermal conductivity accumulation function as a function of mean free path (approximated to be film thickness) from Ref. (Li et al., 2012) is plotted as the teal solid line in Fig. 6·5(a). Our data points are below the curve suggesting that phonon scattering on the surface of our films is not the dominant form of phonon-scattering.

Phonons in polycrystalline diamond should be primarily scattered at the grain boundary of the diamond films (Bozorg-Grayeli et al., 2013). The cross-plane thermal conductivity measurements from Ref. (Sood et al., 2016) are plotted in Fig. 6·5(a). Sood *et* al. measured the anisotropic thermal conductivity of suspended diamond films using Time-Domain Thermoreflectance (TDTR). At low thickness, the cross-plane thermal conductivity values are quite similar. However the results for our 3.4 and 4.1 μm film exceed those of their 5 μm film. In addition, the in-plane thermal conductivity of the diamond films in our study had a larger value than those measured by Sood *et* al.. This is most likely a result from larger grain size in our samples as noted in our SEM images.

The thermal boundary conductance between the Au/Ti transducer and diamond and diamond/silicon are plotted in Fig. 6·5(b). The value for $G_{\mathrm{Au/Ti-Di}}$ ranges from 200-300 MW/m^{2}K while $G_{\mathrm{Di-Si}}$ ranges from 20-25 MW/m^{2}K. There are no values for $G_{\mathrm{Di-Si}}$ for the diamond films greater than 4 μm due to the low sensitivity. The low value of $G_{\mathrm{Di-Si}}$ is not surprising. Obtaining a large between any material and diamond has traditionally been difficult due to the high phonon frequency of diamond, which results in a poor phonon-matching (Bozorg-Grayeli et al., 2013; Cho et al., 2014; Swartz and Pohl, 1989). We found it very easy to delaminate the diamond films from silicon. Applying UV tape onto a sample and peeling the tape would exfoliate the diamond from the silicon substrate. This suggests weak chemical bonding between the diamond and silicon atoms.

Improving the adhesion strength between two materials should increase the thermal boundary conductance (Losego et al., 2012). This concept was implemented to achieve the relatively high TBC between the Au/Ti transducer layer and diamond substrate by oxygen plasma ashing the film prior to metallization. The oxygen plasma changed the termination of the diamond film from hydrogen to oxygen terminated allowing for a stronger chemical bond between the metal and diamond (Monachon et al., 2014). In a previous study by Hohensee *et al.* (Hohensee et al., 2015) the authors found that the TBC between Platinum and Aluminum increased with an increase in pressure. Surprisingly, they found that after a critical pressure was crossed and the pressure was removed, the TBC between the metal and diamond remained higher than the original state.

To gain some additional insight, we used the Diffuse Mismatch Model (DMM) to calculate $G_{\mathrm{PVAc-Au}}$ and $G_{\mathrm{PVAc-Si}}$ (Swartz and Pohl, 1989). We computed the DMM using measured temperature-dependent volumetric heat capacity of the two materials (Bellis et al., 2000), and assumed single event, fully diffuse, and elastic phonon scattering at the interface, which implies that phonons will scatter once at the interface but may scatter into different phonon branches (Duda et al., 2010). The thermal interface conductance is then given by

$$G_{\mathrm{DMM}} = \left(\frac{v_{1D}^3 \sum_j v_{1,j}^{-2} \sum_j v_{2,j}^{-2}}{12(\sum_j v_{1,j}^{-2} + \sum_j v_{2,j}^{-2})} \right) \rho_1 c_{p,1}(T) \tag{6.4}$$

where $\rho_1 c_{p,1}(T)$ is the volumetric heat capacity of material 1 at temperature T, $v_{i,j}$ is the phonon velocity in material i for the jth phonon mode, and $v_{1,D}$ is the average phonon velocity in material 1. Bulk values for diamond, Ti, and Si were used in

this calculation (Swartz and Pohl, 1989). The DMM is known to under-predict or over-predict G based on the ratio of the Debye temperatures, Θ_D, of the two materials (Norris and Hopkins, 2009). Therefore, we compute adjusted DMM values using an empirical correction, Z, based on the Debye temperature ratios of our materials where:

$$Z = 0.157 \left(\frac{\Theta_{D,1}}{\Theta_{D,2}} \right)^{-1.127} \tag{6.5}$$

and

$$G_{\text{corrected}} = G_{\text{DMM}} \times Z \tag{6.6}$$

The final results of the DMM are plotted in Fig. 6·5(b) for $G_{\text{DMM-Au/Ti-Diamond}}$ and $\text{G}_{\text{DMM-Diamond-Si}}$. The value predicted for $G_{\text{Au/Ti-Diamond}}$ is 141 MW/m^{2}K and 207 MW/m^{2}K for $G_{\text{Diamond-Si}}$. Both predictions are within an order of magnitude of the measured value, however, the predicted value for $G_{\text{Diamond-Si}}$ is very far off. We believe this to be a result of the weak physical bonding of the diamond film to the silicon substrate.

6.6 Summary and Future Work

In this section we measured the anisotropic thermal conductivity of diamond films in the thickness range of 1 μm to 10 μm. We find that the cross plane thermal conductivity of the 10 μm film reaches about 75% of bulk value. However, the in-plane thermal conductivity does not increase significantly. We believe this to be a result of the phonon-scattering on the grain boundaries of the polycrystalline films. Finally, the thermal boundary conductance of a metal to diamond was improved by plasma ashing the sample. However, the TBC between the diamond to the silicon substrate was limited by weak adhesion of the film. Future work includes using a thermal model to capture the trend of in-plane and cross-plane thermal conductivity as a function of thickness and grain size.

Chapter 7

Summary and Outlook

7.1 Summary

Thermal transport in size-constrained thin-films and across interfaces is critical to current and emerging technologies. Frequency Domain Thermoreflectance (FDTR) is a powerful tool for studying a wide variety of thermal transport phenomena. This thesis makes several contributions toward improving and extending its use for the characterization of thermal properties.

Chapter two reviewed thermal conductivity and thermal boundary conductance. We defined a phonon and gave simple equations to predict thermal transport across interfaces through the Diffuse Mismatch Model (DMM) and in size constrained materials through the relaxation time approximation to the Boltzmann Transport Equation (BTE).

Chapter three reviewed the optical pump-probe thermal microscope, frequency domain thermoreflectance (FDTR). We gave details about the setup, software and imaging techniques. FDTR imaging was demonstrated for a test sample and for measurements of AlN micro-particles embedded in an epoxy host.

Chapter four focused on thermal transport in polymer films. We discussed the Langmuir-Blodgett (LB) technique for creating nanometer-thick polymer films to study the thermal boundary conductance across polymers-substrate interfaces. We found that the thermal conductivity of polymer films made through the LB technique were up to two times high than their bulk value. We also found the thermal boundary conductance between the polymer PVAc and silicon to be on the order of 70 MW/m^2K, and 90 MW/m^2K between PVAc and gold, with the Lc phase exhibiting slightly higher thermal interface conductance. This chapter demonstrated that the LB approach can be applied to study thermal transport at the interface between many combinations of polymers and substrates, and may be useful for designing composite materials and microelectronic devices that incorporate polymers.

Chapter five focused on thermal transport in gallium nitride (GaN) material systems. Gallium nitride is a wide-bandgap semiconductor materials that has promising application in high frequency devices and LEDs. High frequency operation of GaN-based devices is limited by heat removal from the active region. In this chapter, we presented the first measurements of the thermal boundary conductance between GaN and 4H-SiC with no transition layer from 300–600 K. We found that the TBC of GaN–SiC increases with temperature and is generally greater than the TBC for GaN grown on an AlN transition layer. Additionally, we used FDTR to study thermal transport in a GaN film grown on SiC in the thickness range of 15-1000 nm. Using Monte Carlo simulations, we compared the results of a one-parameter fit of κ_{GaN} with $G_{\mathrm{Au/Ni-GaN}}$ held constant and a two-parameter fit of κ_{GaN} and $G_{\mathrm{Au/Ni-GaN}}$, and found evidence of ballistic transport across the film at thicknesses below 150 nm. The dependence of thermal conductivity on film thickness is in good agreement with a BTE model based on the relaxation time approximation.

Chapter six focused on the measurement of the anisotropic thermal conductivity of diamond films in the thickness range of 1-10 μm. Diamond has an extremely high thermal conductivity, about five times higher than SiC, and is the ideal material for near-junction thermal management in GaN-based devices. We find that the cross plane thermal conductivity of a 10 μm diamond film reaches about 75% of bulk value. However, the in-plane thermal conductivity remains around 200-400 W/m^{2}K. Finally, the thermal boundary conductance between Au/Ti and diamond was improve by plasma ashing the sample. However, the TBC between the diamond to the silicon substrate was limited by weak adhesion of the film. Future work includes using a thermal model to capture the trend of in-plane and cross-plane thermal conductivity as a function of thickness and grain size.

7.2 Future Work on FDTR

7.2.1 Sweeping spot sizes

An improvement to FDTR measurements can be done. Sweeping the height of the sample and changing the laser spot size could provide another degree of freedom for thermal measurements. Varying the laser spot can be used to extract multiple thermophysical properties (Liu et al., 2013b). As was discussed in the Experiment chapter we perform autofocusing by stepping the sample along the z-axis. This technique finds the effective thermal spot size as a function of z, where $z = 0$ is the focal

plane at the beam waste. One could also use beam equations to estimate the spot size according to Ref. (Hecht, 2002):

$$w(z) = w_0\sqrt{1+\left(\frac{z\lambda}{0.32\pi w_0^2}\right)^2} \tag{7.1}$$

where λ is the wavelength of the light and w_0 is the diffraction limited spot size, which can be measured or calculated with:

$$w_0 = 0.61\lambda/\mathrm{NA} \tag{7.2}$$

where NA is the numerical aperture of the objective. Using this technique, Eq. 7.1 is plotted for our 785nm pump and 532nm probe in Fig. 7·1(a). The effective spot size is also plotted where w_{eff} is defined as:

$$w_{\mathrm{eff}} = \sqrt{\frac{w_{\mathrm{pump}}^2 + w_{\mathrm{probe}}^2}{2}} \tag{7.3}$$

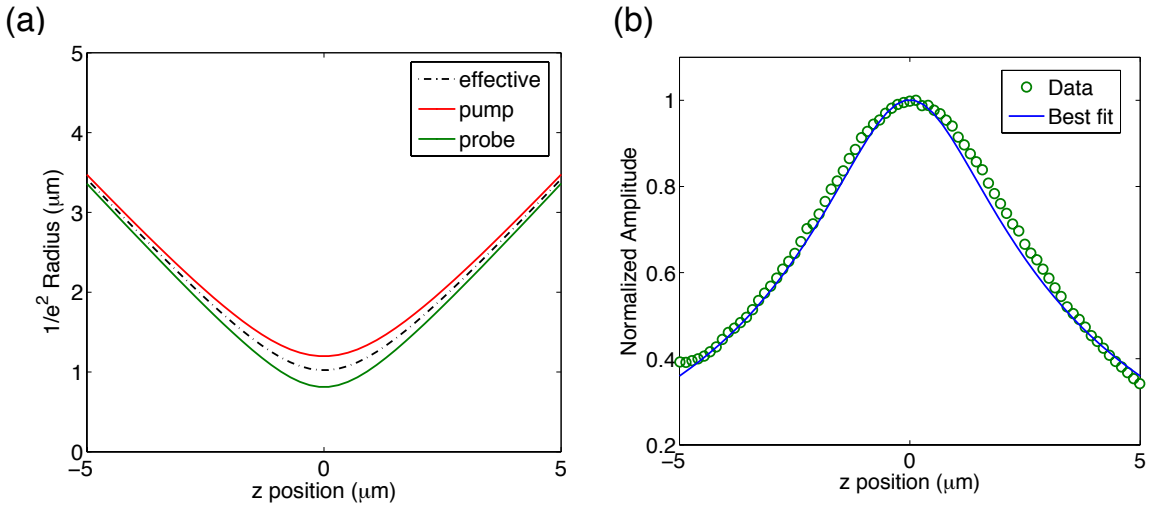

Figure 7·1: (a) Change in spot sizes as a function of position of sample relative to the focal plane, z. (b) FDTR data at 5MHz fit as a function of z.

It is possible that if the effective spot size as a function of sample height is known then the thermal properties of the material could be extracted through a least square fit such as the one shown in Fig. 7·1(b).

References

Abeles, B. (1963). Lattice thermal conductivity of disordered semiconductor alloys at high temperatures. *Physical Review*, 131(5):1906–1911.

Agarwal, V. K. (1988). Langmuir-Blodgett Films. *Physics Today*, 41(6):40.

Albrecht, J. D., Chang, T.-H., Kane, A. S., and Rosker, M. J. (2010). DARPA's Nitride Electronic NeXt Generation Technology Program. In *2010 IEEE Compound Semiconductor Integrated Circuit Symposium (CSICS)*, pages 1–4. IEEE.

Albrecht, O., Gruler, H., Sackmann, E., Albrecht, O., Gruler, H., and Polymorphism, E. S. (1978). Polymorphism of phospholipid monolayers. *Journal de Physique*, 39(3):301–313.

Arora, P. and Zhang, Z. (2004). Battery separators. *Chemical Reviews*, 104(10):4419–4462.

Asen-Palmer, M., Bartkowski, K., Gmelin, E., Cardona, M., Zhernov, A. P., Inyushkin, A. V., Taldenkov, A., Ozhogin, V. I., Itoh, K. M., and Haller, E. E. (1997). Thermal conductivity of germanium crystals with different isotopic compositions. *Physical Review B*, 56(15):9431–9447.

Ashcroft, N.W. and Mermin, N. (1976). *Solid State Physics*. Saunders College.

Babic, D. I., Diduck, Q., Yenigalla, P., Schreiber, A., Francis, D., Faili, F., Ejeckam, F., Felbinger, J. G., and Eastman, L. F. (2010). GaN-on-diamond field-effect transistors: from wafers to amplifier modules. *MIPRO, 2010 Proceedings of the 33rd International Convention*.

Beckwith, T. G., Marangoni, R. D., and Lienhard, J. H. (2007). *Mechanical Measurements*. Pearson Prentice Hall Upper Saddle River, NJ.

Beechem, T. E., McDonald, A. E., Fuller, E. J., Talin, A. A., Rost, C. M., Maria, J.-P., Gaskins, J. T., Hopkins, P. E., and Allerman, A. A. (2016). Size dictated thermal conductivity of GaN. *Journal of Applied Physics*, 120(9):095104.

Bellis, L. D., Phelan, P. E., and Prasher, R. S. (2000). Variations of Acoustic and Diffuse Mismatch Models in Predicting Thermal-Boundary Resistance. *Journal of Thermophysics and Heat Transfer*, 14(2):144–150.

Bloschock, K. P. and Bar-Cohen, A. (2012). Advanced thermal management technologies for defense electronics. In *Proceedings of SPIE*, pages 8405:OI–OI12.

Bozorg-Grayeli, E., Sood, A., Asheghi, M., Gambin, V., Sandhu, R., Feygelson, T. I., Pate, B. B., Hobart, K., and Goodson, K. E. (2013). Thermal conduction inhomogeneity of nanocrystalline diamond films by dual-side thermoreflectance. *Applied Physics Letters*, 102(11):111907.

Briseno, A. L., Mannsfeld, S. C. B., Ling, M. M., Liu, S., Tseng, R. J., Reese, C., Roberts, M. E., Yang, Y., Wudl, F., and Bao, Z. (2006). Patterning organic single-crystal transistor arrays. *Nature*, 444(7121):913–917.

Brummer, G., Nothern, D., Nikiforov, A. Y., and Moustakas, T. D. (2015). Deep ultraviolet distributed Bragg reflectors based on graded composition AlGaN alloys. *Applied Physics Letters*, 106(22):221107.

Buchenau, U. and Wischnewski, A. (2004). Fragility and compressibility at the glass transition. *Physical Review B - Condensed Matter and Materials Physics*, 70(9):1–4.

Cahill, D. G. (1990). Thermal conductivity measurement from 30 to 750 K: The 3ω method. *Review of Scientific Instruments*, 61(2):802–808.

Cahill, D. G., Braun, P. V., Chen, G., Clarke, D. R., Fan, S., Goodson, K. E., Keblinski, P., King, W. P., Mahan, G. D., Majumdar, A., Maris, H. J., Phillpot, S. R., Pop, E., and Shi, L. (2014). Nanoscale thermal transport. II. 2003-2012. *Applied Physics Reviews*, 1(1):011305.

Callaway, J. (1959). Model for Lattice Thermal Conductivity at Low Temperatures. *Physical Review*, 113(4):1046–1051.

Cardenas, C., Fabris, D., Tokairin, S., Madriz, F., and Yang, C. Y. (2012). Thermoreflectance Measurement of Temperature and Thermal Resistance of Thin Film Gold. *Journal of Heat Transfer*, 134(11):111401.

Carslaw, H. and Jaeger, J. (1959). *Conduction of Heat in Solids*. Oxford University Press, 2nd edition.

Chen, G. (2005). *Nanoscale Energy Transport and Conversion*. Oxford University Press, New York.

Chen, H.-Y., Hou, J., Zhang, S., Liang, Y., Yang, G., Yang, Y., Yu, L., Wu, Y., and Li, G. (2009). Polymer solar cells with enhanced open-circuit voltage and efficiency. *Nature Photonics*, 3(11):649–653.

Chen, Y., Li, D., Lukes, J. R., and Majumdar, A. (2005). Monte Carlo Simulation of Silicon Nanowire Thermal Conductivity.

Cho, J. and Goodson, K. E. (2015). Thermal transport: Cool electronics. *Nature Materials*, 14(2):136–137.

Cho, J., Li, Y., Altman, H., Hoke, W. E., Asheg, M., and Goodson, K. E. (2012). Temperature Dependent Thermal Resistances at GaN-Substrate Interfaces in GaN Composite Substrates. In *2012 IEEE Compound Semiconductor Integrated Circuits Symposium (CSICS)*, pages 1–4.

Cho, J., Li, Z., Asheghi, M., and Goodson, K. E. (2014). Near-junction thermal management: thermal conduction in gallium nitride composite substrates. *Annual Review of Heat Transfer*, 18:1–65.

Cho, J., Li, Z., Bozorg-Grayeli, E., Kodama, T., Francis, D., Ejeckam, F., Faili, F., Asheghi, M., and Goodson, K. E. (2013). Improved Thermal Interfaces of GaN–Diamond Composite Substrates for HEMT Applications. *IEEE Transactions on Components, Packaging and Manufacturing Technology*, 3(1):79–85.

Choi, M. C., Kim, Y., and Ha, C. S. (2008). Polymers for flexible displays: From material selection to device applications. *Progress in Polymer Science (Oxford)*, 33(6):581–630.

Chou, Y. C., Leung, D., Smorchkova, I., Wojtowicz, M., Grundbacher, R., Callejo, L., Kan, Q., Lai, R., Liu, P. H., Eng, D., and Oki, A. (2004). Degradation of AlGaN/GaN HEMTs under elevated temperature lifetesting. *Microelectronics Reliability*, 44(7):1033–1038.

Davydov, V. Y., Kitaev, Y. E., Goncharuk, I. N., Smirnov, a. N., Graul, J., Semchinova, O., Uffmann, D., Smirnov, M. B., Mirgorodsky, a. P., and Evarestov, R. a. (1998). Phonon dispersion and Raman scattering in hexagonal GaN and AlN. *Physical Review B*, 58(19):12899–12907.

Dobos, L., Pécz, B., Tóth, L., Horváth, Z., Horváth, Z., Tóth, a., Horváth, E., Beaumont, B., and Bougrioua, Z. (2006). Metal contacts to n-GaN. *Applied Surface Science*, 253(2):655–661.

Donovan, B. F., Szwejkowski, C. J., Duda, J. C., Cheaito, R., Gaskins, J. T., Peter Yang, C.-Y., Constantin, C., Jones, R. E., and Hopkins, P. E. (2014). Thermal boundary conductance across metal-gallium nitride interfaces from 80 to 450K. *Applied Physics Letters*, 105(20):203502.

Duda, J. C., Hopkins, P. E., Smoyer, J. L., Bauer, M. L., English, T. S., Saltonstall, C. B., and Norris, P. M. (2010). On the Assumption of Detailed Balance in Prediction of Diffusive Transmission Probability During Interfacial Transport. *Nanoscale and Microscale Thermophysical Engineering*, 14(1):21–33.

Duda, J. C., Yang, C.-Y. P., Foley, B. M., Cheaito, R., Medlin, D. L., Jones, R. E., and Hopkins, P. E. (2013). Influence of interfacial properties on thermal transport at gold:silicon contacts. *Applied Physics Letters*, 102(8):081902.

English, T. S., Duda, J. C., Smoyer, J. L., Jordan, D. a., Norris, P. M., and Zhigilei, L. V. (2012). Enhancing and tuning phonon transport at vibrationally mismatched solid-solid interfaces. *Physical Review B - Condensed Matter and Materials Physics*, 85(3):1–14.

Forrest, S. R. (2004). The path to ubiquitous and low-cost organic electronic appliances on plastic. *Nature*, 428(6986):911–918.

Fournier, D. and Plamann, K. (1995). Thermal measurements on diamond and related materials. *Diamond and Related Materials*, 4(5-6):809–819.

Francis, D., Faili, F., Babić, D., Ejeckam, F., Nurmikko, A., and Maris, H. (2010). Formation and characterization of 4-inch GaN-on-diamond substrates. *Diamond and Related Materials*, 19(2-3):229–233.

Garcia-Manyes, S., Domènech, O., Sanz, F., Montero, M. T., and Hernandez-Borrell, J. (2007). Atomic force microscopy and force spectroscopy study of Langmuir-Blodgett films formed by heteroacid phospholipids of biological interest. *Biochimica et biophysica acta*, 1768(5):1190–8.

Gong, L., Wang, Y., Cheng, X., Zhang, R., and Zhang, H. (2014). International Journal of Heat and Mass Transfer A novel effective medium theory for modelling the thermal conductivity of porous materials. *International Journal of Heat and Mass Transfer*, 68:295–298.

Goodson, K. E. (1996). Thermal Conduction in Nonhomogeneous CVD Diamond Layers in Electronic Microstructures. *Journal of Heat Transfer*, 118(2):279.

Graebner, J. E., Jin, S., Kammlott, G. W., Herb, J. A., and Gardinier, C. F. (1992). Large anisotropic thermal conductivity in synthetic diamond films. *Nature*, 359(6394):401–403.

Groeneveld, R. H. M., Sprik, R., and Lagendijk, A. (1995). Femtosecond spectroscopy of electron-electron and electron-phonon energy relaxation in Ag and Au. *Physical Review B*, 51(17):11433–11445.

Haynes, W. M. (2015). *CRC handbook of chemistry and physics*. CRC Press.

Hecht, E. (2002). *Optics*. Addison Wesley, 4th edition.

Hitova, L., Yakimova, R., Trifonova, E. P., Lenchev, A., and Janzen, E. (2000). Heat Capacity of 4H-SiC Determined by Differential Scanning Calorimetry. *Journal of The Electrochemical Society*, 147(9):3546.

Hohensee, G. T., Wilson, R. B., and Cahill, D. G. (2015). Thermal conductance of metal-diamond interfaces at high pressure. *Nature communications*, 6:6578.

Holland, M. G. (1963). Analysis of Lattice Thermal Conductivity. *Physical Review*, 132(6):2461–2471.

Hong, L., Novikov, V. N., and Sokolov, A. P. (2011). Is there a connection between fragility of glass forming systems and dynamic heterogeneity/cooperativity? *Journal of Non-Crystalline Solids*, 357(2):351–356.

Hopkins, P. E. (2013). Thermal Transport across Solid Interfaces with Nanoscale Imperfections: Effects of Roughness, Disorder, Dislocations, and Bonding on Thermal Boundary Conductance. *ISRN Mechanical Engineering*, 2013:1–19.

Hopkins, P. E., Kassebaum, J. L., and Norris, P. M. (2009). Effects of electron scattering at metal-nonmetal interfaces on electron-phonon equilibration in gold films. *Journal of Applied Physics*, 105(2):023710.

Hoppe, H. and Sariciftci, N. S. (2004). Organic solar cells: An overview. *Journal of Materials Research*, 19(07):1924–1945.

Iacopi, F., Van Hove, M., Charles, M., and Endo, K. (2015). Power electronics with wide bandgap materials: Toward greener, more efficient technologies. *MRS Bulletin*, 40(05):390–395.

Joint Committee for Guides in Metrology (JCGM) (2008). *Evaluation of Measurement Data: Guide to the Expression of Uncertainty in Measurement*. Number September.

Joshi, A. A. and Majumdar, A. (1993). Transient ballistic and diffusive phonon heat transport in thin films. *Journal of Applied Physics*, 74(1):31–39.

Kazan, M. (2009). First principles calculation of the thermal conductance of GaN/Si and GaN/SiC interfaces as functions of the interface conditions. *Applied Physics Letters*, 95(14):141904.

Kittel, C. (2004). *Introduction to Solid State Physics*. Wiley, 8 edition.

Koh, Y. K. and Cahill, D. G. (2007). Frequency dependence of the thermal conductivity of semiconductor alloys. *Physical Review B - Condensed Matter and Materials Physics*, 76(7):1–5.

Kotchetkov, D., Zou, J., Balandin, A. A., Florescu, D. I., and Pollak, F. H. (2001). Effect of dislocations on thermal conductivity of GaN layers. *Applied Physics Letters*, 79(26):4316–4318.

Krupa, I., Mikova, G., and Prokes, J. (2007). Electrically conductive composites of polyethylene filled with polyamide particles coated with silver. *European Polymer Journal*, 43:2401–2413.

Kukushkin, S. A., Osipov, A. V., Bessolov, V. N., Medvedev, B. K., Nevolin, V. K., and Tcarik, K. A. (2008). Substrates for epitaxy of gallium nitride: New materials and techniques. *Reviews on Advanced Materials Science*, 17(1-2):1–32.

Lee, S., Kwon, S. Y., and Ham, H. J. (2011). Specific Heat Capacity of Gallium Nitride. *Japanese Journal of Applied Physics*, 50(11):11RG02.

Levinshtein, M. E., Rumyantsev, S. L., and Shur, M. S. (2001). *Properties of Advanced Semiconductor Materials: GaN, AIN, InN, BN, SiC, SiGe*. John Wiley & Sons.

Li, W., Carrete, J., Katcho, N. A., and Mingo, N. (2014). ShengBTE: A solver of the Boltzmann transport equation for phonons. *Computer Physics Communications*, 185(6):1747–1758.

Li, W., Mingo, N., Lindsay, L., Broido, D. A., Stewart, D. A., and Katcho, N. A. (2012). Thermal conductivity of diamond nanowires from first principles. *Physical Review B - Condensed Matter and Materials Physics*, 85(19):1–5.

Lindsay, L., Broido, D. A., and Reinecke, T. L. (2012). Thermal conductivity and large isotope effect in GaN from first principles. *Physical Review Letters*, 109(9):1–5.

Liu, J., Ju, S., Ding, Y., and Yang, R. (2014). Size effect on the thermal conductivity of ultrathin polystyrene films. *Applied Physics Letters*, 104(15):153110.

Liu, J., Yoon, B., Kuhlmann, E., Tian, M., Zhu, J., George, S. M., Lee, Y. C., and Yang, R. (2013a). Ultralow thermal conductivity of atomic/molecular layer-deposited hybrid organic-inorganic zincone thin films. *Nano Letters*, 13:5594–5599.

Liu, J., Zhu, J., Tian, M., Gu, X., Schmidt, A. J., and Yang, R. (2013b). Simultaneous measurement of thermal conductivity and heat capacity of bulk and thin film materials using frequency-dependent transient thermoreflectance method. *Review of Scientific Instruments*, 84(3):034902.

Losego, M. D., Grady, M. E., Sottos, N. R., Cahill, D. G., and Braun, P. V. (2012). Effects of chemical bonding on heat transport across interfaces. *Nature materials*, 11(6):502–6.

Losego, M. D., Moh, L., Arpin, K. A., Cahill, D. G., and Braun, P. V. (2010). Interfacial thermal conductance in spun-cast polymer films and polymer brushes. *Applied Physics Letters*, 97(1):011908.

Majumdar, A. and Reddy, P. (2004). Role of electron-phonon coupling in thermal conductance of metal-nonmetal interfaces. *Applied Physics Letters*, 84(23):4768–4770.

Malen, J. A., Baheti, K., Tong, T., Zhao, Y., Hudgings, J. A., and Majumdar, A. (2011). Optical measurement of thermal conductivity using fiber aligned frequency domain thermoreflectance. *Journal of Heat Transfer*, 133(8):81601.

Malen, J. A., Yee, S. K., Majumdar, A., and Segalman, R. A. (2010). Fundamentals of energy transport, energy conversion, and thermal properties in organic-inorganic heterojunctions. *Chemical Physics Letters*, 491(4-6):109–122.

Meneghesso, G., Verzellesi, G., Danesin, F., Rampazzo, F., Zanon, F., Tazzoli, A., Meneghini, M., and Zanoni, E. (2008). Reliability of GaN high-electron-mobility transistors: State of the art and perspectives. *IEEE Transactions on Device and Materials Reliability*, 8(2):332–343.

Metzger, T., Höpler, R., Born, E., Ambacher, O., Stutzmann, M., Stömmer, R., Schuster, M., Göbel, H., Christiansen, S., Albrecht, M., and Strunk, H. P. (1998). Defect structure of epitaxial GaN films determined by transmission electron microscopy and triple-axis X-ray diffractometry. *Philosophical Magazine A*, 77(4):1013–1025.

Mion, C., Muth, J. F., Preble, E. A., and Hanser, D. (2006). Accurate dependence of gallium nitride thermal conductivity on dislocation density. *Applied Physics Letters*, 89(9):092123.

Mishra, U. K., Shen, L., Kazior, T. E., and Wu, Y. F. (2008). GaN-based RF power devices and amplifiers. *Proceedings of the IEEE*, 96(2):287–305.

Monachon, C., Schusteritsch, G., Kaxiras, E., and Weber, L. (2014). Qualitative link between work of adhesion and thermal conductance of metal/diamond interfaces. *Journal of Applied Physics*, 115:123509.

Monachon, C. and Weber, L. (2013). Influence of diamond surface termination on thermal boundary conductance between Al and diamond. *Journal of Applied Physics*, 113(18):183504.

Morelli, D., Heremans, J., and Slack, G. (2002). Estimation of the isotope effect on the lattice thermal conductivity of group IV and group III-V semiconductors. *Physical Review B*, 66(19):1–9.

Moskalyk, R. (2003). Gallium: the backbone of the electronics industry. *Minerals Engineering*, 16(10):921–929.

Moustakas, T. D. (2013). The role of extended defects on the performance of optoelectronic devices in nitride semiconductors. *Physica Status Solidi (A) Applications and Materials Science*, 210(1):169–174.

Müller, M. (2002). Chain conformations and correlations in thin polymer films: A Monte Carlo study. *Journal of Chemical Physics*, 116(22):9930–9938.

Ni, S., Lee, W., Li, B., and Esker, A. (2006). Thermodynamics of the liquid expanded to condensed phase transition of poly (L-lactic acid) in Langmuir monolayers. *Langmuir*, 22(8):3672–7.

Nilsson, O., Mehling, H., Horn, R., Fricke, J., Hofmann, R., Müller, S. G., Eckstein, R., and Hofmann, D. (1997). Determination of the thermal diffusivity and conductivity of monocrystalline silicon carbide (300-2300 K). *High Temperatures-High Pressures*, 29:73–79.

Norris, P. M. and Hopkins, P. E. (2009). Examining Interfacial Diffuse Phonon Scattering Through Transient Thermoreflectance Measurements of Thermal Boundary Conductance. *Journal of Heat Transfer*, 131(4):043207.

Ohkita, M., Higuchi, M., and Kawaguchi, M. (2005). AFM studies on LB films of poly(n-hexyl isocyanate), poly(vinyl acetate), and their binary mixtures. *Journal of colloid and interface science*, 292(1):300–3.

Ong, W. L. (2015). *Thermal Properties of Organic-Inorganic Materials Superstructured at the Nanoscale*. PhD thesis, Carnegie Mellon University.

Ong, W. L., Majumdar, S., Malen, J. a., and McGaughey, A. J. H. (2014). Coupling of organic and inorganic vibrational states and their thermal transport in nanocrystal arrays. *Journal of Physical Chemistry C*, 118(14):7288–7295.

Palik, E. D. (1985). *Handbook of optical constants of solids*. Academic Press, Orlando.

Ravichandran, J., Yadav, A. K., Cheaito, R., Rossen, P. B., Soukiassian, A., Suresha, S. J., Duda, J. C., Foley, B. M., Lee, C.-H. C.-H., Zhu, Y., Lichtenberger, A. W., Moore, J. E., Muller, D. A., Schlom, D. G., Hopkins, P. E., Majumdar, A., Ramesh, R., and Zurbuchen, M. A. (2013). Crossover from incoherent to coherent phonon scattering in epitaxial oxide superlattices. *Nature Materials*, 13:168–72.

Rosker, M. J. (2007). The Present State of the Art of Wide-Bandgap Semiconductors and Their Future. In *2007 IEEE Radio Frequency Integrated Circuits (RFIC) Symposium*, pages 159–162. IEEE.

Ruf, T., Serrano, J., Cardona, M., Pavone, P., Pabst, M., Krisch, M., D'Astuto, M., Suski, T., Grzegory, I., and Leszczynski, M. (2001). Phonon dispersion curves in wurtzite-structure GaN determined by inelastic X-ray scattering. *Physical Review Letters*, 86(5):906–909.

Sakaguchi, T., Taniguchi, N., Urakawa, O., and Adachi, K. (2005). Calorimetric study of dynamical heterogeneity in blends of polyisoprene and poly(vinylethylene). *Macromolecules*, 38(2):422–428.

Schmidt, A. J. (2008). *Optical Characterization of Thermal Transport from the Nanoscale to the Macroscale*. PhD thesis, Massachusetts Institute of Technology.

Schmidt, A. J., Cheaito, R., and Chiesa, M. (2009). A frequency-domain thermoreflectance method for the characterization of thermal properties. *The Review of scientific instruments*, 80(9):094901.

Shen, M. X., Cui, Y. X., He, J., and Zhang, Y. M. (2011). Thermal conductivity model of filled polymer composites. *International Journal of Minerals, Metallurgy and Materials*, 18(5):623–631.

Shi, L., Dames, C., Lukes, J. R., Reddy, P., Duda, J., Cahill, D. G., Lee, J., Marconnet, A., Goodson, K. E., Bahk, J.-H., Shakouri, A., Prasher, R. S., Felts, J., King, W. P., Han, B., and Bischof, J. C. (2015). Evaluating Broader Impacts of Nanoscale Thermal Transport Research. *Nanoscale and Microscale Thermophysical Engineering*, 19(2):127–165.

Shin, H. S., Jung, Y. M., Lee, J., Chang, T., Ozaki, Y., and Kim, S. B. (2002). Structural comparison of Langmuir-Blodgett and spin-coated films of poly(tert-butyl methacrylate) by external reflection FTIR spectroscopy and two-dimensional correlation analysis. *Langmuir*, 18(14):5523–5528.

Singh, V., Bougher, T. L., Weathers, A., Cai, Y., Bi, K., Pettes, M. T., McMenamin, S. A., Lv, W., Resler, D. P., Gattuso, T. R., Altman, D. H., Sandhage, K. H., Shi, L., Henry, A., and Cola, B. A. (2014). High thermal conductivity of chain-oriented amorphous polythiophene. *Nature nanotechnology*, 9(5):384–90.

Soles, C. L. and Ding, Y. (2008). Nanoscale Polymer Processing. *Science*, 322(5902):689–690.

Song, L. and Evans, J. W. (2000). Electrochemical-Thermal Model of Lithium Polymer Batteries. *Journal of The Electrochemical Society*, 147(6):2086.

Sood, A., Cho, J., Hobart, K. D., Feygelson, T. I., Pate, B. B., Asheghi, M., Cahill, D. G., and Goodson, K. E. (2016). Anisotropic and inhomogeneous thermal conduction in suspended thin-film polycrystalline diamond. *Journal of Applied Physics*, 119(17):175103.

Srikant, V., Speck, J. S., and Clarke, D. R. (1997). Mosaic structure in epitaxial thin films having large lattice mismatch. *Journal of Applied Physics*, 82(9):4286–4295.

Su, G. P., Zheng, X. H., Qiu, L., Tang, D. W., and Zhu, J. (2013a). Measurement of thermal conductivity of anisotropic SiC crystal. *International Journal of Thermophysics*, 34(12):2334–2342.

Su, M., Chen, C., and Rajan, S. (2013b). Prospects for the application of GaN power devices in hybrid electric vehicle drive systems. *Semiconductor Science and Technology*, 28(7):074012.

Su, Z., Freedman, J. P., Leach, J. H., Preble, E. A., Davis, R. F., and Malen, J. A. (2013c). The impact of film thickness and substrate surface roughness on the thermal resistance of aluminum nitride nucleation layers. *Journal of Applied Physics*, 113(21):213502.

Su, Z., Huang, L., Liu, F., Freedman, J. P., Porter, L. M., Davis, R. F., and Malen, J. A. (2012). Layer-by-layer thermal conductivities of the Group III nitride films in blue/green light emitting diodes. *Applied Physics Letters*, 100(20).

Swartz, E. T. and Pohl, R. O. (1989). Thermal boundary resistance. *Reviews of Modern Physics*, 61(3):605–668.

Tomczak, N., Vallée, R. A. L., Van Dijk, E. M. H. P., Kuipers, L., Van Hulst, N. F., and Vancso, G. J. (2004). Segment Dynamics in Thin Polystyrene Films Probed by Single-Molecule Optics. *Journal of the American Chemical Society*, 126(15):4748–4749.

Touloukian, Y S ; Buyco, E. H., Touloukian, Y. S., and Buyco, E. H. (1970). *Thermophysical Properties of Matter - The TPRC Data Series. Volume 4. Specific Heat - Metallic Elements and Alloys*.

Tritt, T. M. (2004). *Thermal Conductivity*. Kluwer Academic, Plenum Publishers, New York.

Ulman, A. (1991). *An introduction to ultrathin organic films: from Langmuir-Blodgett to self-assembly*. Academic Press.

Van Krevelen, D. and Te Nijenhuis, K. (2009). *Properties of Polymers*. Elsevier.

Wang, Z., Zhang, Z., Zhang, J., and Sheng, K. (2014). Power electronic transformer for dc power distribution network. In *2014 International Power Electronics and Application Conference and Exposition*, pages 805–810. IEEE.

Ward, A., Broido, D. A., Stewart, D. A., and Deinzer, G. (2009). Ab initio theory of the lattice thermal conductivity in diamond. *Physical Review B - Condensed Matter and Materials Physics*, 80(12):1–8.

Wilson, R. B., Apgar, B. A., Martin, L. W., and Cahill, D. G. (2012). Thermoreflectance of metal transducers for optical pump-probe studies of thermal properties. *Optics Express*, 20(27):28829–38.

Wilson, R. B. and Cahill, D. G. (2014). Anisotropic failure of Fourier theory in time-domain thermoreflectance experiments. *Nature Communications*, 5:5075.

Wilson, R. B. and Cahill, D. G. (2015). Limits to Fourier theory in high thermal conductivity single crystals. *Applied Physics Letters*, 107(2015):203112.

Wilson, R. B., Feser, J. P., Hohensee, G. T., and Cahill, D. G. (2013). Two-channel model for nonequilibrium thermal transport in pump-probe experiments. *Physical Review B - Condensed Matter and Materials Physics*, 88(14):1–11.

Won, Y., Cho, J., Agonafer, D., Asheghi, M., and Goodson, K. E. (2013). Cooling limits for GaN HEMT technology. In *Technical Digest - IEEE Compound Semiconductor Integrated Circuit Symposium, CSIC*, pages 1–5.

Wong, C. P. and Bollampally, R. S. (1999). Thermal Expansion of Polymer Composites Filled with Ceramic Particles for Electronic Packaging. *Journal of Applied Polymer Science*, (1):3396–3403.

Wyrwas, E., Condra, L., and Hava, A. (2011). Accurate quantitative physics-of-failure approach to integrated circuit reliability. *IPC APEX EXPO Technical Conference 2011*, 3:1776–1815.

Xu, J., Yin, W. Y., and Mao, J. (2007). Transient thermal analysis of GaN heterojunction transistors (HFETs) for high-power applications. *IEEE Microwave and Wireless Components Letters*, 17(1):55–57.

Yan, Z., Liu, G., Khan, J. M., and Balandin, A. A. (2012). Graphene quilts for thermal management of high-power GaN transistors. *Nature Communications*, 3:827.

Yang, J. (2016). *Thermal Property Measurement With Frequency Domain Thermoreflectance*. PhD thesis, Boston University.

Yang, J., Maragliano, C., and Schmidt, A. J. (2013). Thermal property microscopy with frequency domain thermoreflectance. *Review of Scientific Instruments*, 84(10):104904.

Yang, J., Ziade, E., Maragliano, C., Crowder, R., Wang, X., Stefancich, M., Chiesa, M., Swan, A. K., and Schmidt, A. J. (2014). Thermal conductance imaging of graphene contacts. *Journal of Applied Physics*, 116(2):023515.

Yang, J., Ziade, E., and Schmidt, A. J. (2016a). Modeling optical absorption for thermoreflectance measurements. *Journal of Applied Physics*, 119(9):095107.

Yang, J., Ziade, E., and Schmidt, A. J. (2016b). Uncertainty analysis of thermoreflectance measurements. *Review of Scientific Instruments*, 87(1):014901.

Zhai, X. and Kleijn, J. (1997). Molecular structure of dipalmitoylphosphatidylcholine Langmuir-Blodgett monolayers studied by atomic force microscopy. *Thin Solid Films*, 304(1-2):327–332.

Zhang, Y., Zhang, H. L., Wu, J. H., and Wang, X. T. (2011). Enhanced thermal conductivity in copper matrix composites reinforced with titanium- coated diamond particles Enhanced thermal conductivity in copper matrix composites reinforced with titanium-coated diamond particles. *Scripta Materialia*, 65(12):1097–1100.

Zhou, X., Jones, R., Kimmer, C., Duda, J., and Hopkins, P. (2013). Relationship of thermal boundary conductance to structure from an analytical model plus molecular dynamics simulations. *Physical Review B*, 87(9):094303.

Zhou, X. W., Jones, R. E., Hopkins, P. E., and Beechem, T. E. (2014). Thermal boundary conductance between Al films and GaN nanowires investigated with molecular dynamics. *Physical Chemistry Chemical Physics*, 16(20):9403.

Ziade, E., Goni, M., Sato, T., Czubarow, P., and Schmidt, A. J. (2015a). Thermal conductance of nanoscale Langmuir-Blodgett films. *Applied Physics Letters*, 107(22):221603.

Ziade, E., Yang, J., Brummer, G., Nothern, D., Moustakas, T., and Schmidt, A. J. (2015b). Thermal transport through GaN-SiC interfaces from 300 to 600 K. *Applied Physics Letters*, 107(9):091605.

Ziade, E., Yang, J., Brummer, G., Nothern, D., Moustakas, T., and Schmidt, A. J. (2017). Thickness dependent thermal conductivity of gallium nitride. *Applied Physics Letters*, 110(3):031903.

Ziade, E., Yang, J., Brummer, G., Nothern, D., Moustaks, T., and Schmidt, A. J. (2016). Mapping Thickness Dependent Thermal Conductivity of GaN. *Journal of Heat Transfer*, 138(2):020906.

Ziade, E., Yang, J., Sato, T., Czubarow, P., and Schmidt, A. J. (2015c). Thermal Property Imaging of Aluminum Nitride Composites. *Journal of Heat Transfer*, 137(2):020902.

Zou, J., Kotchetkov, D., Balandin, A. A., Florescu, D. I., and Pollak, F. H. (2002). Thermal conductivity of GaN films: Effects of impurities and dislocations. *Journal of Applied Physics*, 92(5):2534–2539.

CURRICULUM VITAE